UiT
THE ARCTIC
UNIVERSITY
OF NORWAY

Faculty of Science and Technology
Department of Geosciences

A structural, geomorphological and InSAR study of the unstable rock slopes at Mellomfjellet, Nordreisa

Gaute Sikveland

GEO-3900 Master's thesis in Geology

May 2019

UNIVERSITY OF TROMSØ

Cover photo by Louise M. Vick

Abstract

The focus of this study has been to combine structural data with morphological observations and displacement data to characterise the unstable rock slopes at Mellomfjellet. The site contains two instabilities (Mellomfjellet 1 and 2) and is located along a west-facing slope in Reisadalen, a glacially eroded valley, in Nordreisa, Troms. The bedrock consists mainly of Caledonian amphibolite and hornblende schist, displaying Caledonian ductile and Post-Caledonian brittle structures. NNW-SSE and NNE-SSW-striking backscarps delimit the unstable area and align with the strike of the Post-Caledonian regional brittle structures. The backscarps seem to control the extent of the unstable rock slopes, as displacement from InSAR shows a downslope movement inside the areas delimited by the backscarps.

Structural analysis based on traditional field data revealed two structural domains (Mellomfjellet 1 and 2) each with three joint sets: Mellomfjellet 1: J1 (029/72±16), J2 (288/84±21) and J3 (075/67±12); and Mellomfjellet 2: J1 (022/81±14), J2 (108/88±15) and J3 (075/47±17). J1 and J2 were most dominant joint sets, striking parallel to subparallel with the backscarps. J3 was found only found adjacent to two E-W striking lineaments, cross-cutting the two instabilities. The undulating foliation (155/13±17 and 183/11±15, Mellomfjellet 1 and 2 respectively) is shallowly dipping downslope, and gently folded with a fold axis (237->13) also plunging downslope. Structural analysis based on a photogrammetric point cloud identified both J1, J2 and the foliation, and showed the same orientations as the field data when taking the variance into account.

Kinematic analysis and field observations suggest planar sliding along a failure surface stepping between sub vertical joints (J1 and J2) and the foliation. Mellomfjellet 1 shows morphological features similar with a DSGSD, complex fields and a biplanar compound slide. Mellomfjellet 2 show features similar with a slide topple, and a biplanar compound slide.

A failure scenario for each of the instabilities was determined, based on the delimiting backscarps and morphological features, where both scenarios lie in the medium hazard class. Mellomfjellet 1 has an estimated volume of 1.12×10^6 m^3 and Mellomfjellet 2 has an estimated volume of 3.05×10^6 m^3. The run-out analysis showed that Mellomfjellet 1 will not reach any infrastructure or buildings, while Mellomfjellet 2 is likely to reach a construction site where a new power line is being established. Both of the instabilities are classified as low risk sites.

Acknowledgements

I would like to thank my supervisor Louise Vick, at the University of Tromsø (UiT), for all the valuable guidance and feedback. Thank you for all the time and effort you have put into this project. I would also like to thank my co-supervisor, Martina Böhme, at the Geological Survey of Norway (NGU). Thank you for teaching me how to use the different software and for all your comments and feedback on this project.

I would also like to thank Bernt Kristian Vik for good team work, productive discussions and great sense of humour during the field work and at the office. Thanks to all my fellow students at UiT for two great years here in Tromsø.

I would also like to thank my family for supporting me throughout my studies. And Malene, thank you for supporting me through this thesis.

Tromsø, May 2019

Gaute Sikveland

Table of Contents

1 Introduction

1.1 Background of the study

Norway is a country known for its dramatic topography, with steep mountains and deep fjords formed over multiple glacial cycles. As a result, the possibility for slope hazards, including landslides, is high. Landslides can have major consequences, leading to infrastructure disruption and damage, and in the worst case, fatalities. Landslides can also have secondary consequences which pose a risk to society. Catastrophic failure of landslide dams can lead to flooding downstream. Large displacement waves can be triggered if the landslide runs out in an adjacent fjord (Hermanns and Longva, 2012). This exposes a threat to a large portion of Norwegian society, since many people inhabit narrow valleys, resulting in established villages in the hazard zone. In total, 33,000 historical landslides are recorded in Norway, leading to 4,475 fatalities (Hermanns et al., 2012a). Historically, 2-6 major landslides from rock slope failure have occurred per century along the coast of Norway (Hermanns et al., 2014). Three major rock avalanches have occurred in the last century (Tafjord 1934, Loen 1935 and 1936), causing a total of 174 fatalities, mainly from large displacement waves triggered by the landslides (Blikra et al., 2006).

As a response, the Norwegian Geological Survey (NGU) started systematic mapping of unstable rock slopes in 2005. More than 300 potential unstable rock slopes have been identified and characterized within three counties: Møre og Romsdal (91), Sogn og Fjordane (23) and Troms (117; Oppikofer et al., 2015). Due to the high number of potential rock slope failures, a standardized risk and hazard classification system was established in 2012 (Hermanns et al., 2014). The classification system makes it easier to prioritize which site needs to be mapped and monitored first, based on the consequences a potential rock slope failure may have for human lives (Hermanns et al., 2013).

1.2 Aim of the study

The aim for this master thesis is to investigate the unstable rock slopes (URSs), Mellomfjellet 1 and 2, to get a better understanding of mechanisms active at the site. To do so, the project has focused on the geomorphological and tectonic elements, which will be valuable knowledge for future hazard predictions and scenario modelling. The thesis will try to answer the following questions:

- What is the main failure mechanism of the URSs?
- What kind of influence do the inherited bedrock structures have on the failure mechanism?
- Can the rock slope failure be described as a deep-seated gravitational slope deformation (DSGSD)?
- What kind of failure scenarios can be expected, in terms of extent, volume and runout length?

To answer these questions, the following work has been conducted:

- Mapping of geomorphological structures indicating deformation of a slope, such as backscarps, subscarps, tension cracks, depressions, trenches, talus and ridges through a combination of desktop study and field observations.
- Mapping of structures in the bedrock (consistent with engineering geology methods and NGU database standards), such as foliation, joints, folds and fold axes.
- A surface model created from drone photogrammetry, using Agisoft Photoscan, to obtain structural data from inaccessible parts of the backscarp. Structural data was obtained from the model using Coltop3D.
- Spatial structural analysis based on the structural data, and kinematic analysis for the different spatial domains using Dips.
- Desktop study of available InSAR-data, to look at the slope deformation-rates.
- Run out modelling, using Flow-R, to look at the potential primary- and secondary consequences regarding a failure of the rock slope.

1.3 Available data

The results presented in this thesis are based on the data gathered during a two week field campaign in September, 2018. The data was collected by the author and Bernt Kristian Flekstad Vik. Data available are listed in Table 1. The coordinate system used is WGS 1984 UTM 33 N

Table 1: Available data

Data	Source	Resolution or scale
Orthophotos	Statens Kartverk	0.25x0.25 m
Topographic data	Statens Kartverk ArcticDEM	 3x3 m
InSAR data	NGU	5x20 m
Aerial photos (helicopter)	NGU	
Drone photos	Gathered in field	
Geological map	NGU	1:50 000

1.4 Study area

1.4.1 Location

Mellomfjellet (883 meters above sea level (m asl)) is a mountain located on the east side of Reisadalen Valley, Northeast of Troms County, on the west-facing slope (Figure 1). The unstable area is at approximately 200 to 500 m asl and is bound by prominent backscarps. Mellomfjellet is divided into two different locations; Mellomfjellet 1 and 2, based on the segmented nature of the unstable area (Figure 1). The combined backscarp of both of the URSs strikes N-S for approx. 1.6 km. The Mellomfjellet 1 backscarps comprises two dominant structures; the southernmost backscarp striking NE – SW and the northernmost backscarps striking NNW – SSE. The backscarp at Mellomfjellet 2 is one prominent scarp, striking in a NNE – SSW direction. Both of the sites have multiple dislocated blocks, separated from each other by subscarps and tension cracks, striking in the same direction as the backscarps. The blocks are heavily fractured and are disintegrating, resulting in large amounts of talus material in between and downslope of the blocks. Sporadic areas of dense vegetation are situated in the

talus. Multiple streams are located at the base of the talus, downslope of the densely vegetated areas. There is a farm, a power line and a river located at the base of the slope of Mellomfjellet 2.

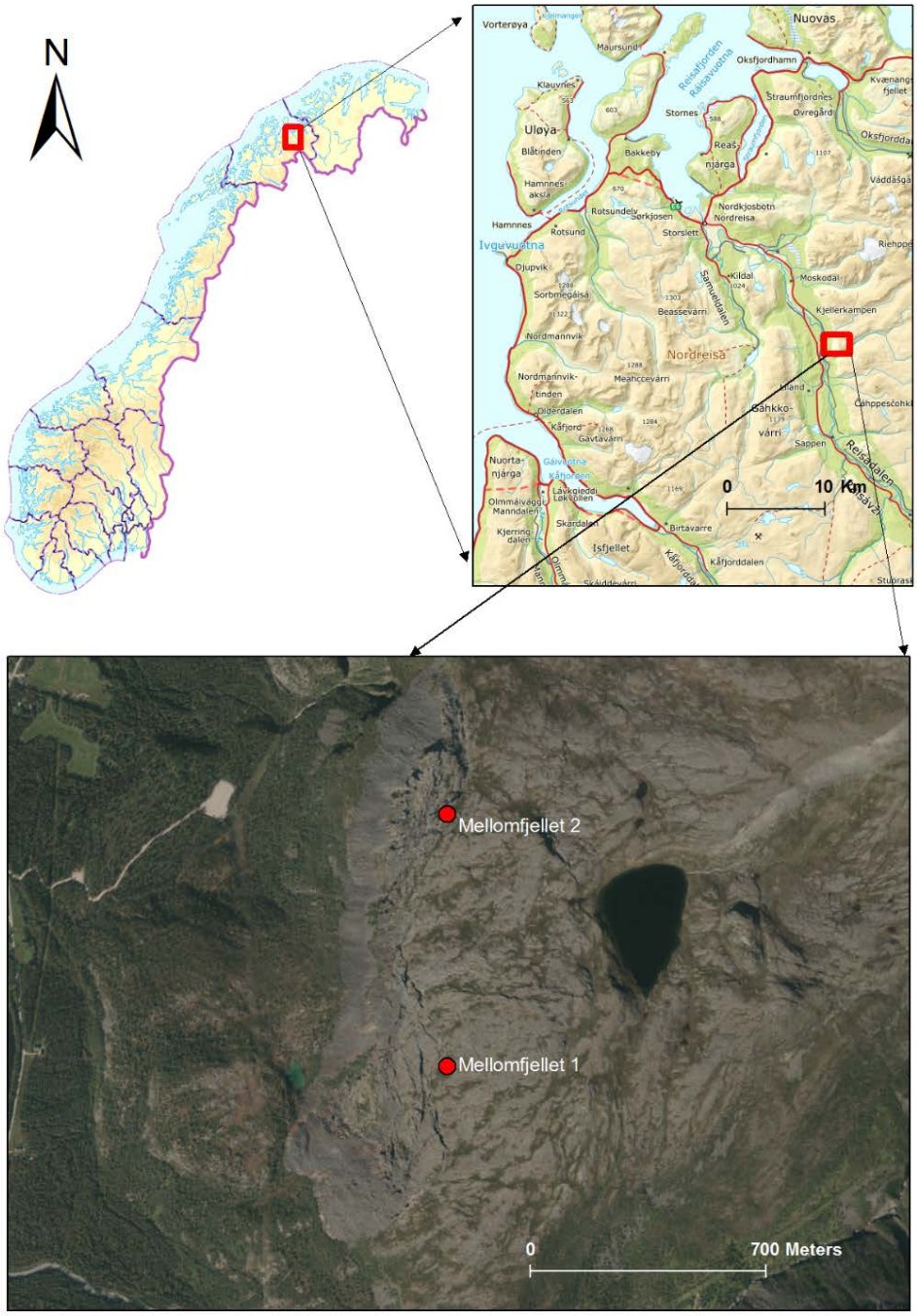

Figure 1: Overview map of the study area.

1.4.2 Climate and weather

Due to the variable topography of Troms, there are large variations in the climatic conditions across the county. The climate close to the coast has a much higher level of precipitation than the more sheltered areas inland. It may vary from a range of 300-600 mm annual precipitation in valleys inland, and up to an annual range of 1000-1500 mm precipitation in the coastal areas. The temperature also varies, largely depending on the location. During the winter months the mean temperature is -2 °C in the coastal areas, and between -6 and -9 °C in the inland valleys. The minimum temperatures measured are -10 to -15 °C along the coast, and -30 to -40 °C in the valleys. The mean temperature during the summer is approximately 12 °C close to the coast and around 14 °C in the inner parts. It may reach 28 and 30°C (coastal and inland respectively) during the summers, when hot air comes in from the south east).

Mellomfjellet is located in Reisadalen, in inner Troms, and experiences a much lower amount of precipitation than the coastal areas. The mean temperature is approximately 10 °C during the summer and around -8 °C during the winter, colder than the coastal areas. The permafrost limit in Northern Norway is at 990 m asl in the coastal areas, and at 550 m asl in the inland valleys (Blikra and Christiansen, 2014). Mellomfjellet, located at 200 – 500 m asl is located below the regional permafrost limit. However, Blikra and Christiansen (2014) found that sporadic permafrost can be present close to sea level in deep-seated rockslide terrains, which could also be the case at Mellomfjellet.

1.4.3 Regional geology

Basement rocks of the Fennoscandian Shield underlie all of Fennoscandia and outcrop in Norway in erosion windows, and in coastal areas of Troms as the West Troms Basement Complex (WTBC; Zwaan, 1988, Zwaan, 1995). The overlying geology across northern Norway is dominated by Caledonian thrust nappes (Ramberg et al., 2007). The WTBC and the Caledonian nappes are separated by the Permian normal fault system, the Vestfjord-Vanna Fault Complex (Doré et al., 1997). Brittle faults and fractures are a result of the collapse of the Caledonian Orogeny, which is related to the opening of the Atlantic Ocean (Ramberg et al., 2007).

1.4.3.1 Caledonian nappes

The Caledonian nappes are divided into four different Allochthons: Uppermost-, Upper-, Middle- and Lower Allochthon, (Figure 2; Ramberg et al., 2007). Mellomfjellet is located in Reisadalen, where two nappe complexes are present: the Reisa Nappe Complex and the Kalak Nappe Complex. The study area is located in the Kalak Nappe Complex (Zwaan, 1988). The

Kalak Nappe Complex is interpreted to be in the Middle Allochthon, and consists of the Gargia-, Nalganas-, Nabar- and Corrovarre Nappes. The rocks in these nappes consist of late Proterozoic to early Cambrian arkoses and underlying layers. The underlying layers consist of two different lithologies: Archean to Proterozoic granitic and amphibolite gneisses (metavolcanic rocks) and Proterozoic mica schist, greenstone and marble (metasedimentary rocks). The Nabar and Corrovarre Nappe (the two upper nappes in the nappe complex) are intruded by mafic plutons which lead to contact metamorphosis on the surrounding rocks (Zwaan, 1988).

The lithology at Mellomfjellet is mainly amphibolite and hornblende schist, which was interpreted by Zwaan (1988) to be metamorphosed gabbro. There is also a layer of calcareous marble, on the 1:50 000 bedrock map of the area (Zwaan et al., 1984). The calcareous marble is part of the Corrovarre Nappe, whereas the amphibolite and hornblende schist is not assigned a specific nappe.

As a result of the Caledonian orogeny, multiple ductile structures are present in the bedrock. Shear zones are common in the bedrock near the thrust faults, due to a high degree of deformation. Due to the Caledonian orogeny, one may also find other ductile structures in the bedrock, such as open asymmetric folds and foliation. The foliation is predominantly moderately to well developed in the schistose units, with a predominant gentle dip towards SW, and is a structure which is important concerning unstable rock slopes (Zwaan, 1988, Corfu et al., 2014, Andresen, 2018).

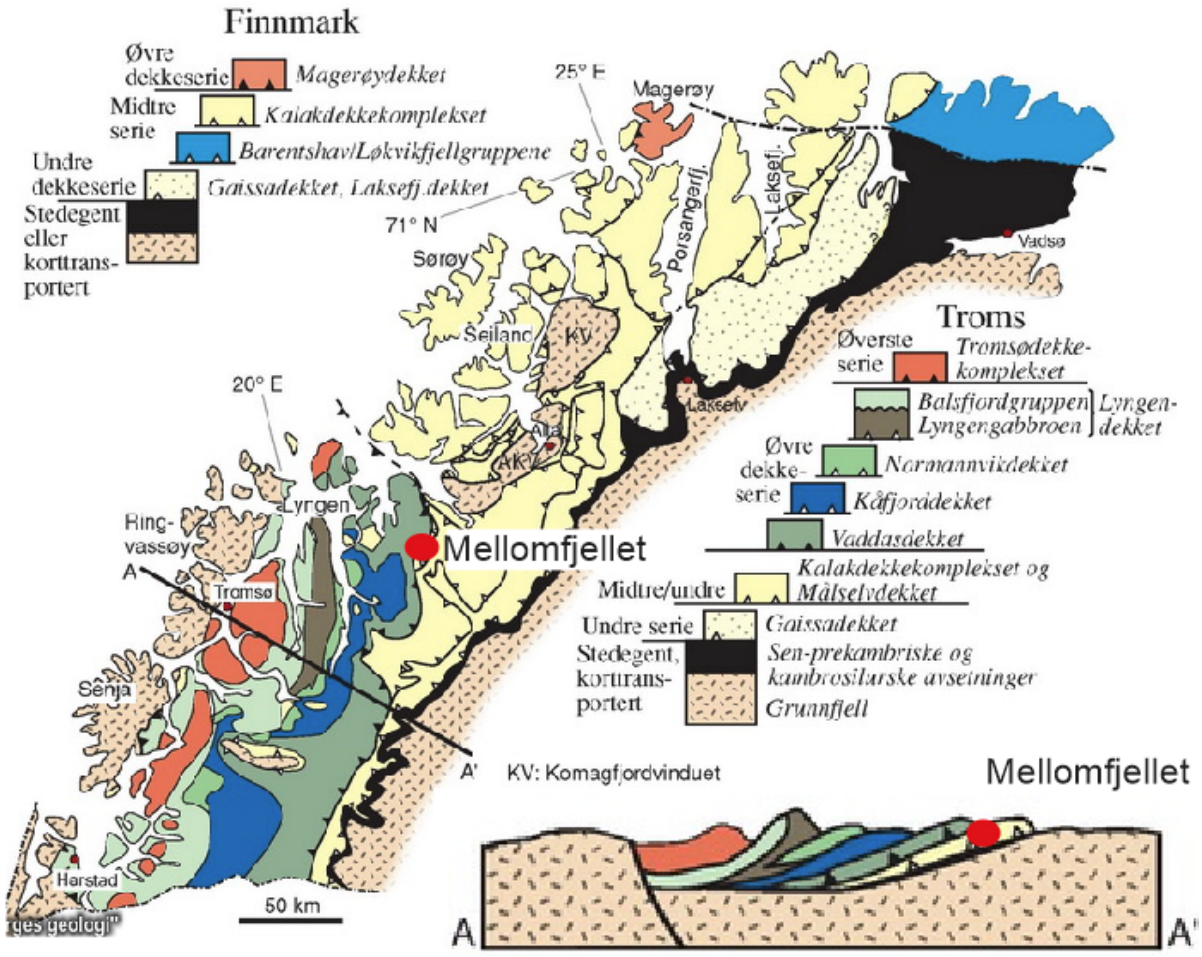

Figure 2: Regional geological setting of Northern Norway. Modified after Ramberg et al. (2007).

1.4.3.2 Post-Caledonian brittle structures

Troms County is dominated by both onshore and offshore faulting. Bergh et al. (2007) and Hansen and Bergh (2012) suggest that the faults were formed due to the collapse of the Caledonian orogeny, by multiple rifting phases during the opening of the Atlantic ocean in the Mesozoic to Paleogene. The faults are trending NE-SW, NNE-SSW and NW-SE, and can be traced from the Lofoten – Vesterålen fault complex to Finnmark (north of Tromsø), as illustrated by Indrevær et al. (2013) in Figure 3.

The Lofoten – Vesterålen fault complex consists of brittle structures trending NNE – SSW and NE – SE. The faults are steeply dipping, and are a result of an extension phase in Triassic to early Cretaceous during the opening of the North Atlantic Ocean (Faleide et al., 2008). Further north, faults related to the SW Barents Sea Margin can be traced. They show similar characteristics as the Lofoten – Vesterålen fault complex, with moderate to steep dip and trending towards the NNE – SSW and ENE – WNW (Indrevær et al., 2013). The faults are part

of two fault complexes, the Vestfjord – Vanna Fault Complex and the Troms – Finnmark Fault Complex. Indrevær et al. (2013) found that these faults are bound by a major basement horst (WTBC), that runs both onshore and offshore. They found that the brittle faulting was mainly controlled by reactivation along Precambrian and Caledonian structures in the bedrock, such as ductile shear zones, foliation and lithological boundaries. It is believed that the rifting occurred during the Carboniferous and Late Permian to Early Triassic time, and that a second rifting event followed in the Late Jurassic to Early Cretaceous resulted in a north westward displacement (Indrevær et al., 2013).

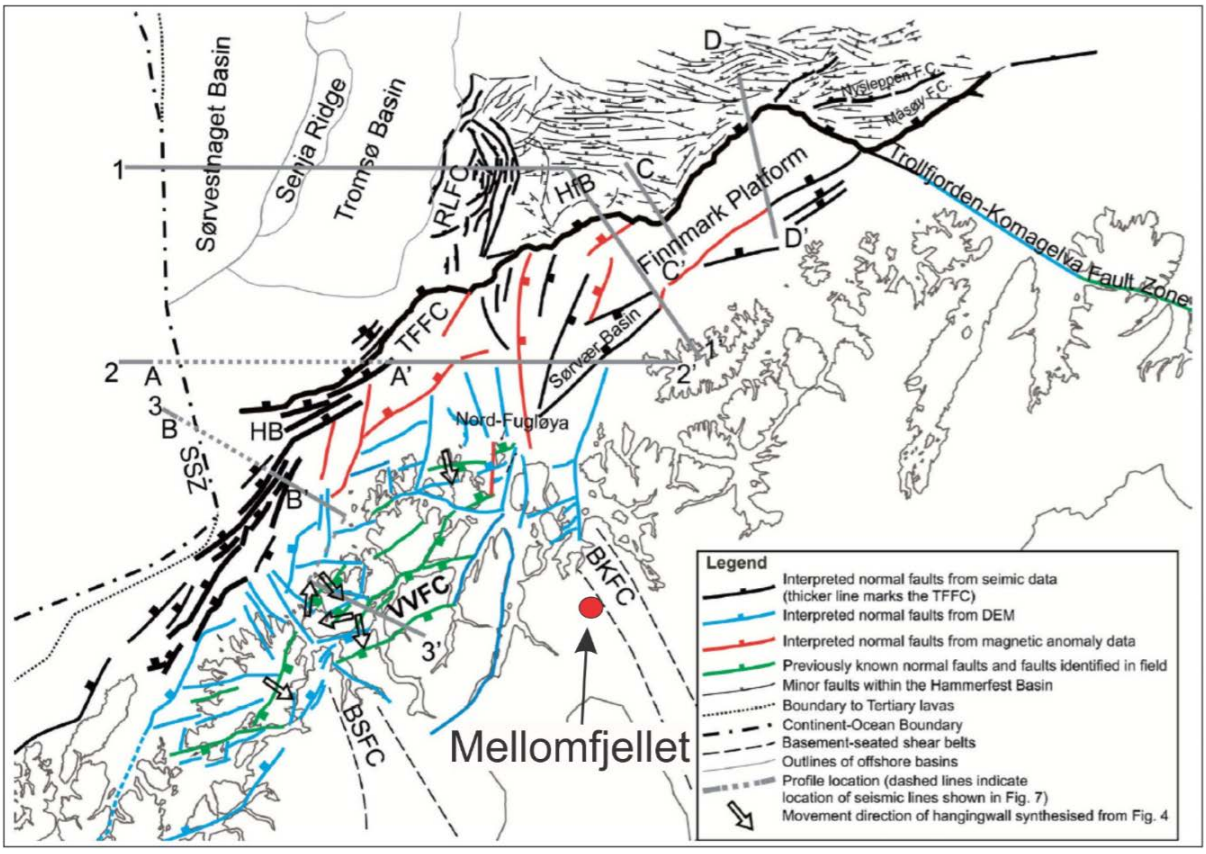

Figure 3: Mapped regional trace lineaments that represents Post-Caledonian normal faults in Northern Norway. Modified after Indrevær et al. (2013).

1.4.1 Quaternary geology

Norway has been through several glacial cycles. Glacial cycles during the Quaternary had a large effect on the development of landforms in Norway (Ramberg et al., 2007). These processes are responsible for shaping the topography of Troms. The glaciers eroded deep U-formed valleys and fjords, usually following structural weaknesses in the bedrock (Indrevær et al., 2013). Isostatic rebound, as a response to deglaciation, changed the elevation profile in the coastal areas which resulted in a steeper landscape (Ramberg et al., 2007). Erosion of the valleys caused over-steepening of the slopes. This lead to a change of the in situ stress field. Failure is known to occur if the applied stress is greater than the rock mass strength (Böhme, 2014). Retreat of the ice lead to debutressing of the rock slopes. Removal of the confining pressure caused by the glaciers, along with the over-steepening caused by erosion, resulted in multiple unstable rock slopes (Ballantyne, 2002, Böhme, 2014).

There are four marginal moraines in Reisadalen, showing the retreat pattern of the glacier since the last glacial maximum: the oldest of the moraines is believed to be of the same age as the Ra moraines of Younger Dryas, which are dated to be approx. 10.3 ka. The three younger events are dated to be 9.9-9.8, 9.7-9.5 and 9.4 ka (Bergstrøm, 1983). The glacial processes have had a massive impact on the topography in the area, with glacial erosion responsible of carving out and shaping the valley (Figure 4). Three URSs are located on the same side of Reisadalen as Mellomfjellet: Brattfjell, Doaresgaisa and Rajajoki (NGU, 2019). It is therefore likely that glacial conditioning of the slopes has led to the occurrence of multiple URSs in Reisadalen.

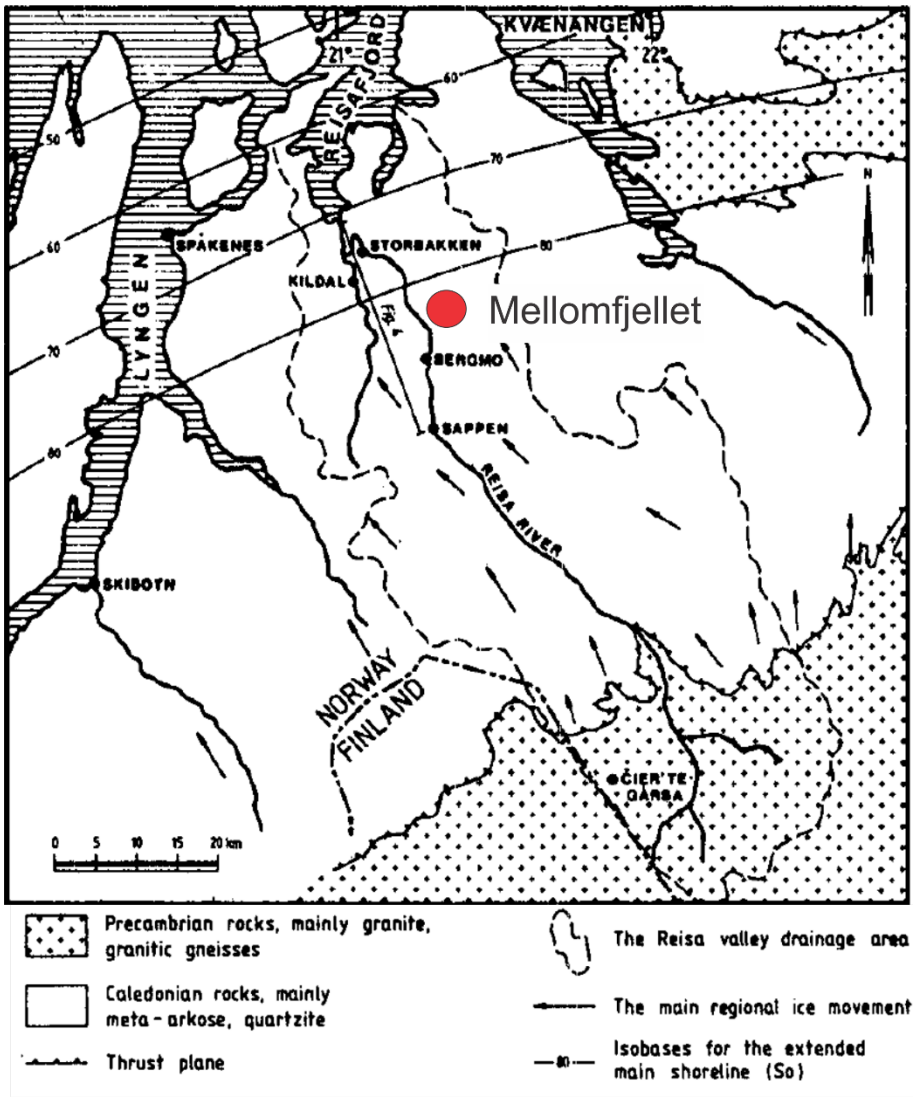

Figure 4: Overview map of the deglaciation of the Reisadalen Valley, where the main regional ice movement going northward throughout Reisadalen is marked. Modified after Bergstrøm (1983).

1.5 Previous Work

Troms County, as an alpine region, has a high density of URSs. There have been previous large rock slope failures, like Hølen, Grovfjorden and Balsfjorden (Blikra et al., 2006, Bunkholt et al., 2013). There are three high risk sites in Troms today: Jettan, Gamanjunni 3 and Indre Nordnes (NGU). At Jettan, located in Kåfjord, a potential failure may result in a tsunami with a 25-30 m run-up height (Glimsdal and Harbitz, 2007).

As a response to the systematic mapping of URSs by NGU, multiple master's thesis's on URSs are written by students at the University of Tromsø – The Arctic University of Norway (e.g. Husby (2011), Rasmussen (2011), Eriksen (2013), Skrede (2013), Hernes (2014), Bredal (2016)

and Andresen (2018)), where the main objectives have been to identify the controlling structures and their geometry in relation to the unstable slopes.

In 2009, NGU visited 12 new locations in Troms, to investigate their potential risk towards society. One of these locations was Mellomfjellet (Henderson et al., 2010). Their main findings were:

- Two main locations at Mellomfjellet: Mellomfjellet 1 (south) and Mellomfjellet 2 (north)
- Mellomfjellet 1:
    - Foliation dipping downslope with a dip angle ca. 15-25˚
    - Multiple discontinuous backscarps striking in two directions, NNW-SSE and NE-SW, creating wedge shaped blocks.
    - An assumed low angle failure plane parallel with the foliation
    - Two main blocks, based on different displacement
    - Rock fall deposits downslope, clearly limited by the NE-SW backscarp
    - Openings along the backscarps showing both backwards rotation and planar sliding, indicating a complex failure mode.
    - Roughly estimated volume of 8 million m^3
- Mellomfjellet 2:
    - Backscarps striking in a NNE-SSW direction, with a higher extent than Mellomfjellet 1.
    - An E-W striking structure divides the location into two parts: Northern parts showing an annual displacement of 8-9 mm, 2-3 mm/year in the southern parts
    - Roughly estimated volume of 9 million m^3

Based on the measured movement, its large volume and its potential risk of damaging properties and humans if a collapse occurs, NGU wanted a more detailed mapping and analysis done at Mellomfjellet. By collecting more data of the structures in the bedrock, morphological features and displacement rates, knowledge from this project may help with the bigger picture of the landslide hazard in Troms, and Norway in general by getting a better understanding of how and why URSs develop.

2 Methods

2.1 Geological and geomorphological mapping

Structural and geomorphological data was collected during a two week field campaign at the beginning of September 2018. The structural data was collected using a Silva Clinometer Compass, recording the strike and dip of the structures, using the right hand rule. Approximately 970 measurements of structures, mainly foliation and joints, were gathered at 31 different stations (Figure 5). The stations were located upslope of the unstable area, inside the unstable area (on larger blocks), and downslope of the unstable area. This ensured structural data was collected for the upper and lower parts of the unstable rock slope as well, which is vital information when making a geological model. Measurements of fold axes were executed when possible. Morphological features associated with rock slope failures, such as tension cracks, backscarps, subscarps, morphological depression and talus material were also mapped. Large scale structures were mapped prior to the field work using orthophotos from different years, with different lighting conditions. These structures were visited in the field and investigated on a more detailed level. Their orientation was measured, alongside with the horizontal and vertical offset. An analysis of the orientation of the lineaments was conducted, where the mapped lineaments were divided into 10 m long segments, and plotted in a rosette diagram. A DJI Inspire drone was used to do a flyover of the site, to get a better overview of the morphological features. Vegetated areas were mapped, as it indicates the presence of water. Streams and wet areas were also mapped, since the presence of water is an important factor for the stability of rock slopes (Wyllie and Mah, 2004). The position of the measurements from the field campaign was taken using a Garmin GPSMap 64st, with an expected precision of 2 m (T. Eiken, personal communication, October 24, 2018).

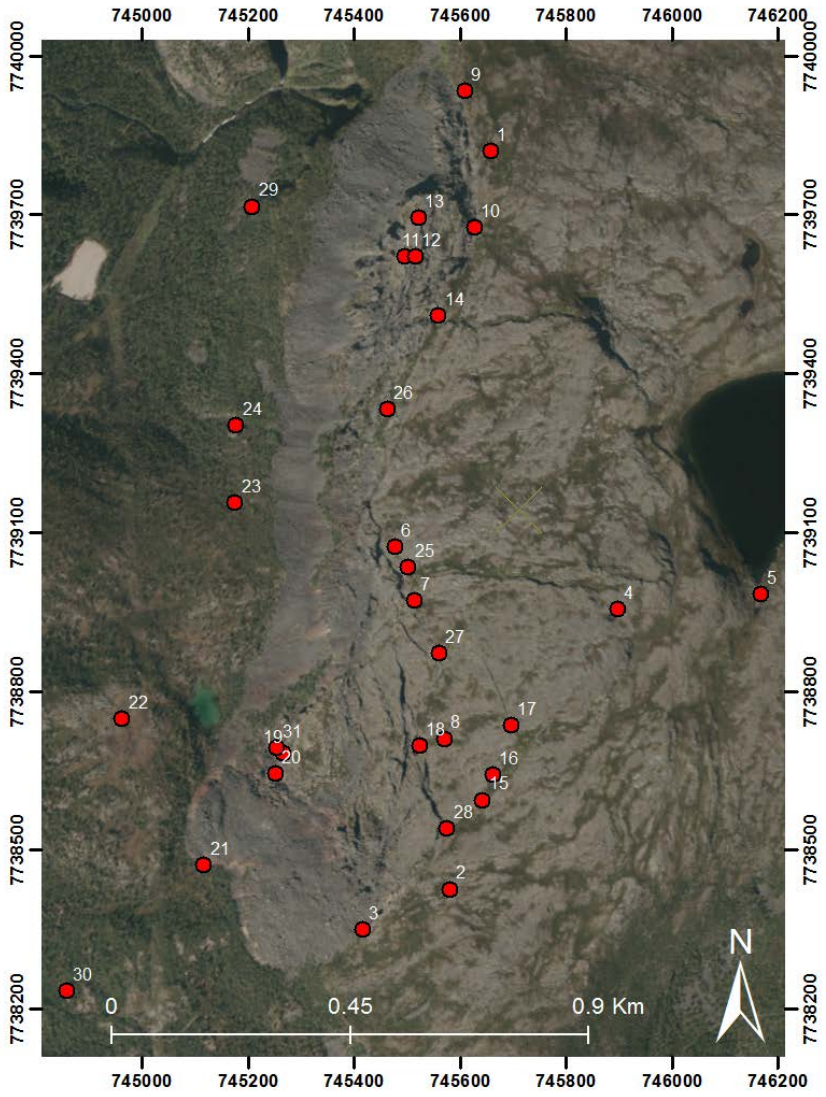

Figure 5: Overview map of all the stations in field, where information were gathered.

2.2 **Photogrammetry**

Photogrammetry is a technique where objects can be presented in 3D, by combining multiple overlapping photos of the objects. This is done by taking photos from different angles and positions, to cover all the visible sides of the object (Figure 6). This method has been utilized in geoscience for many different tasks. Traditionally, it has been used to obtain topographic data from aerial photographs (Bemis et al., 2014). In traditional photogrammetry, several pre-determined ground control points (GCPs) need to be known, in order to extract the correct shape and orientation of the objects (Micheletti et al., 2015). In recent years, a new method has evolved: Structure from Motion (SfM). This is a method that does not need the predefined GCPs

to create a correct 3D-model. SfM determines the orientation automatically by using the cameras position and its internal camera geometry. Due to the lack of GCPs, SfM requires a large overlap for each of the photographs. There are several processing techniques you can use for SfM. Computer software uses algorithms to identify overlapping photographs by recognizing similar points in multiple photos. The photos can be processed automatically and quite rapid, where the only limitation is the available processing power of the computer. To generate the model in real world coordinates, GCPs are necessary in order to scale the model correctly (Micheletti et al., 2015). This can usually be done after the processing of the SfM 3D-model, by identifying visible GCPs in several photos and adding their measured coordinates in the model. One of the most popular devices to use for SfM photogrammetry, is an Unmanned Aerial Vehicle (UAV). Multi-copters are especially popular to use, due to their mobility and relatively low cost. By using a multi-copter UAV, geoscientists may study outcrops and locations which are inaccessible for people, and can cover large areas within a short period of time (Micheletti et al., 2015).

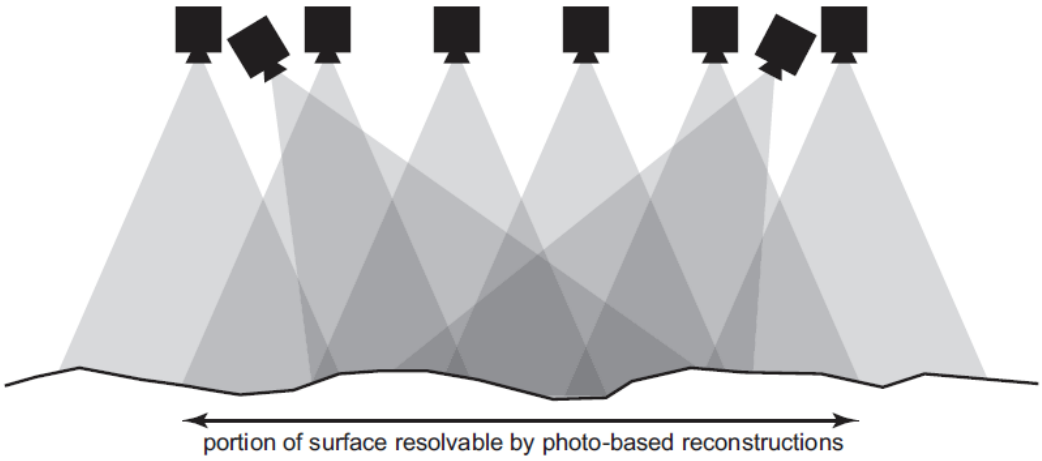

Figure 6: The basic principles of photogrammetry. Multiple positions and angles of the camera results in overlap of the topography. Modified after Bemis et al. (2014).

In this thesis, a UAV was used to gather structural data from an inaccessible part of the backscarp of Mellomfjellet 2. The UAV used was a DJI Inspire 1, with a Zenmuse X3 camera with a 12 megapixel resolution. The backscarp examined was almost vertical. In order to cover all the different sides of the backscarp, the UAV was flown in three different flight paths, at the approx. same horizontal distance to the wall, but at different heights. Each of the paths where flown three times, one with 90 degree, one with 60 and one with 30 degree camera angle (from

vertical). In total, there were taken 279 photos along the three flight paths. Five GCPs were spray marked above and below the study area, where their coordinates were measured using a Garmin GPSMap 64st.

To process the photos, Agisoft Photoscan was used. Agisoft is a software which uses algorithms to create a 3D-model of the area based on the previously mentioned SfM-method. A short summary of the workflow of the processing executed in Agisoft is listed below (Mallison, 2018):

- Import all of the pictures into Agisoft and align them. In this part, the software aligns the photos that overlap each other. For this task, the key point limit was set to 60, 000 (the limit of points that may be re-recognized in other photos), and tie point limit (limit of points which ties one photo to the other) to unlimited. The quality was set to "High" and "Adaptive camera fitting" was on. This resulted in a sparse point cloud.
- The sparse point cloud was then cleaned up, by deleting all the points with a low likelihood of being in the right place. The "gradual selection" feature selects the points based on the re-projection error (removes points with too low correlation) and was set to 0.5, re-construction uncertainty was set to 10 and projection accuracy set to 8. This step reduced the number of points from 1 256 575 to 250 000, which decreased the processing time in the next step.
- Based on the 250 000 high quality points, the dense point cloud was produced. The quality was set to "Ultra high" and the deep filtering to "Aggressive".
- The last step was to import the GCPs in to the dense point cloud. These were identified on all photos where visible, and then given the correct coordinates for WGS84 UTM 33N. This way the model was scaled correctly in relation to the coordinate system and its geographic position.

2.3 Structural analysis

The structural data was analysed in Dips 7.0 (Rocscience, 2018a). Dips 7.0 is a software for plotting structural data in a stereographic projection. The data can also be divided into separate structural sets, both manually or based on statistics of the clusters. Based on the assigned joint sets, the mean strike and dip of the different sets is obtained (Rocscience, 2018a).

The structural data are presented in an equal area projection, in lower hemisphere, and as a contour plot of pole vectors based on a Fisher's distribution. To present the contour plot, the density was set between 0 – 10 %, with dark colours representing high values and bright colours representing low values. When examining contour data, Rocscience (2018b) suggest that any cluster greater than 6 % density is very significant, clusters between 4 – 6 % densities are slightly significant and clusters below 4 % should be considered with care unless the dataset includes several hundreds of measurements. For this project, approx. 970 structural measurements have been collected, and clusters with densities lower than 4% have also been considered for the large scale structural analysis. When creating sets, the tool called "Sets from Cluster Analysis" in Dips was used. The tool uses a cone, where the angle limit of the cone was set to 25˚ (Rocscience, 2018b).

As mentioned in chapter 2.1, the structural data are collected at 31 different stations. Structural data from each station are presented in separate stereonets on an overview map of the area in Appendix A and B.

2.3.1 Analysis in Coltop3D

Detailed 3D-point clouds created from photogrammetry and terrestrial laser scanners (TSL) have become a useful tool for geoscientists in recent years. Their high resolution makes it possible to identify geological and geomorphological structures by identifying surfaces based on the colours visualized by the points reconstructed in the 3D-model. Coltop3D is a software that identifies planar structures in 3D by displaying the orientation and the dip of the pole using the Hue Saturation Intensity (HSI) wheel (Figure 7). The hue represents the orientation of the surface (0-360˚) and the saturation intensity represents the dip angle (0-90˚). This way, the software makes it possible to recognize joint sets based on the different colours (Figure 8; Jaboyedoff et al., 2007)

Structural analysis of 3D-models makes it possible for geoscientists to gather data from remote places. Parts of the backscarp at Mellomfjellet 2 (Figure 1) is inaccessible, which limits the amount of data available from traditional mapping. This makes Coltop3D an excellent tool to get more detailed structural data. Based on the results, it is possible to identify joint sets that are not present at outcrops reachable by foot.

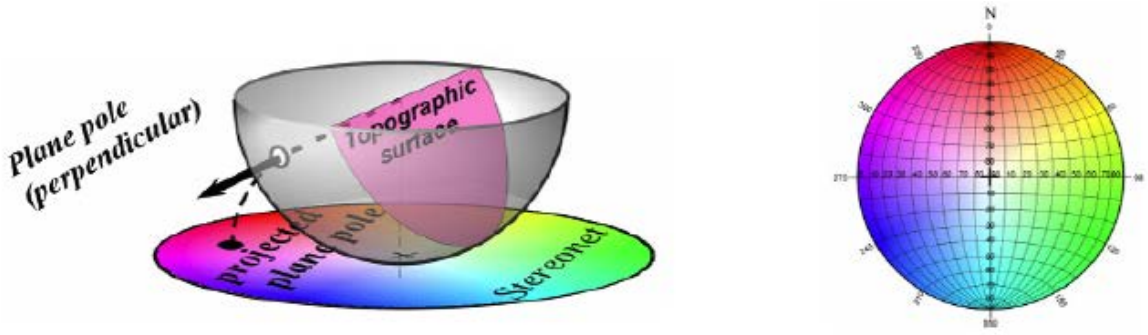

Figure 7: The object to the right shows the colour codes for the poles for the different orientations. The object to the left shows how the colour of the pole represents a plane in a 3D stereonet. Modified after Jaboyedoff et al. (2009).

The following workflow is based on the user manual for Coltop3D (Jaboyedoff et al., 2007). The analysis in Coltop3D is based on the point cloud created from UAV photogrammetry (chapter 2.2). Based on the dominating colours (representing orientations) in the point cloud, polygons where chosen. A polygon was drawn over each of the recognized sets (in the point cloud), where all the point orientations inside these polygons were extracted and exported into an excel file. The excel file was imported into Dips7.0, where sets were assigned using cluster analysis, as explained in chapter 2.3.

The quality of the data extracted from Coltop3D is directly affected by the quality of the 3D-model used for the analysis. If there are areas where the point density is low, structures might not be detected, or smoothed out, influencing the structural data gathered from Coltop3D.

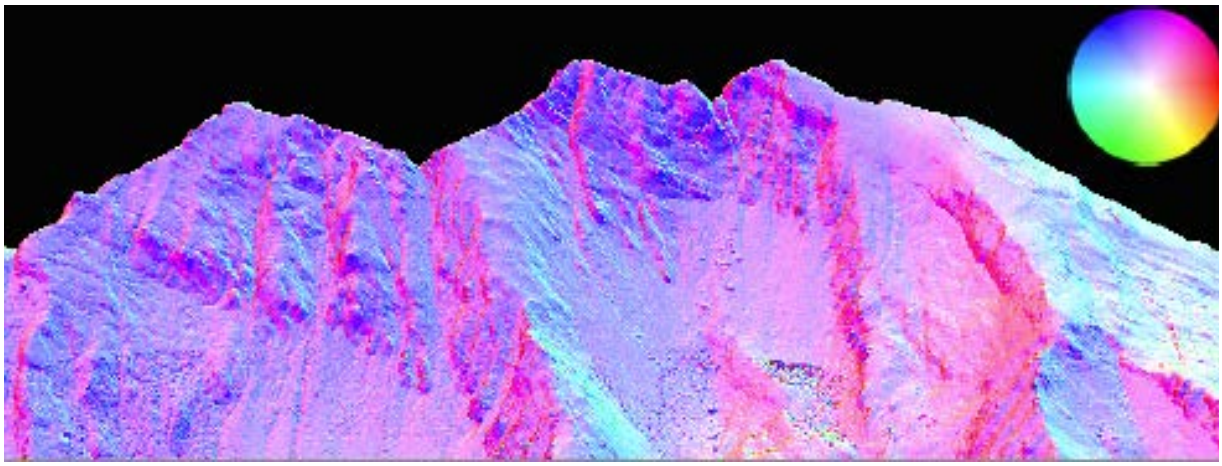

Figure 8: A visualization of a rock slope in Coltop3D, showing steeply dipping structures which have been assigned bright purple colours from the HSU-wheel. Modified after Jaboyedoff et al. (2009).

2.4 Kinematic analysis

Based on the structural data, it is possible to perform a simple kinematic analysis in Dips7.0. By inputting the strike and dip of the slope, alongside the friction angle, the number of poles in the critical zone of failure for the different failure mechanisms are shown. The failure types assessed in dips are planar sliding, wedge sliding, direct and flexural toppling. By performing a kinematic analysis you get an indication of which failure mechanisms are most likely to happen (Rocscience, 2018a). The critical zone for failure is determined by the angle and direction of the slope, the friction angle and the orientation of the discontinuities (Wyllie and Mah, 2004). The friction angle is set to 20˚, a conservative angle recommended by Hermanns et al. (2012b) for large URSs in Norway.

For planar failure, the mean plane of the joint set has to have a lower dip angle than the slope (daylighting in the slope), and a steeper dip than the friction angle (Figure 9A). A wedge failure occurs along the intersecting line of two joint sets. The line of intersection of two planes has to daylight in the slope and be steeper than the friction angle (Figure 9B). Another feasible failure mode for large rock slopes is flexural toppling. For flexural toppling to occur, the dominant joint set has to have a steep dip angle into the slope, with approximately the same orientation as the slope (Figure 9C). It also has to be steep enough for interlayer slip to take place. This way, a series of slope parallel slabs can form (Hermanns et al., 2012b). Direct toppling is not included in the kinematic feasibility test, since it only occurs in minor rock volumes (Hermanns et al., 2012b)

Lateral limit determines a lateral zone for the slope, in which failure is possible to occur. If the joint set is dipping outside of the lateral limit, it is assumed that intact rockmass at one end stabilize the block or rockmass, and failure is not possible (Wyllie and Mah, 2004). In general rock slope engineering, a lateral limit of 20˚ is used for the different failure modes (Wyllie and Mah, 2004). Nevertheless, for large rock slope failures, studies have showed that 20˚ is not a suitable limit, due to more complex structures involved. Therefore, Hermanns et al. (2012b) suggests to set the lateral limit to 30˚. They propose that failure is possible in-between the 30 degree limit, and partly possible outside the lateral limit.

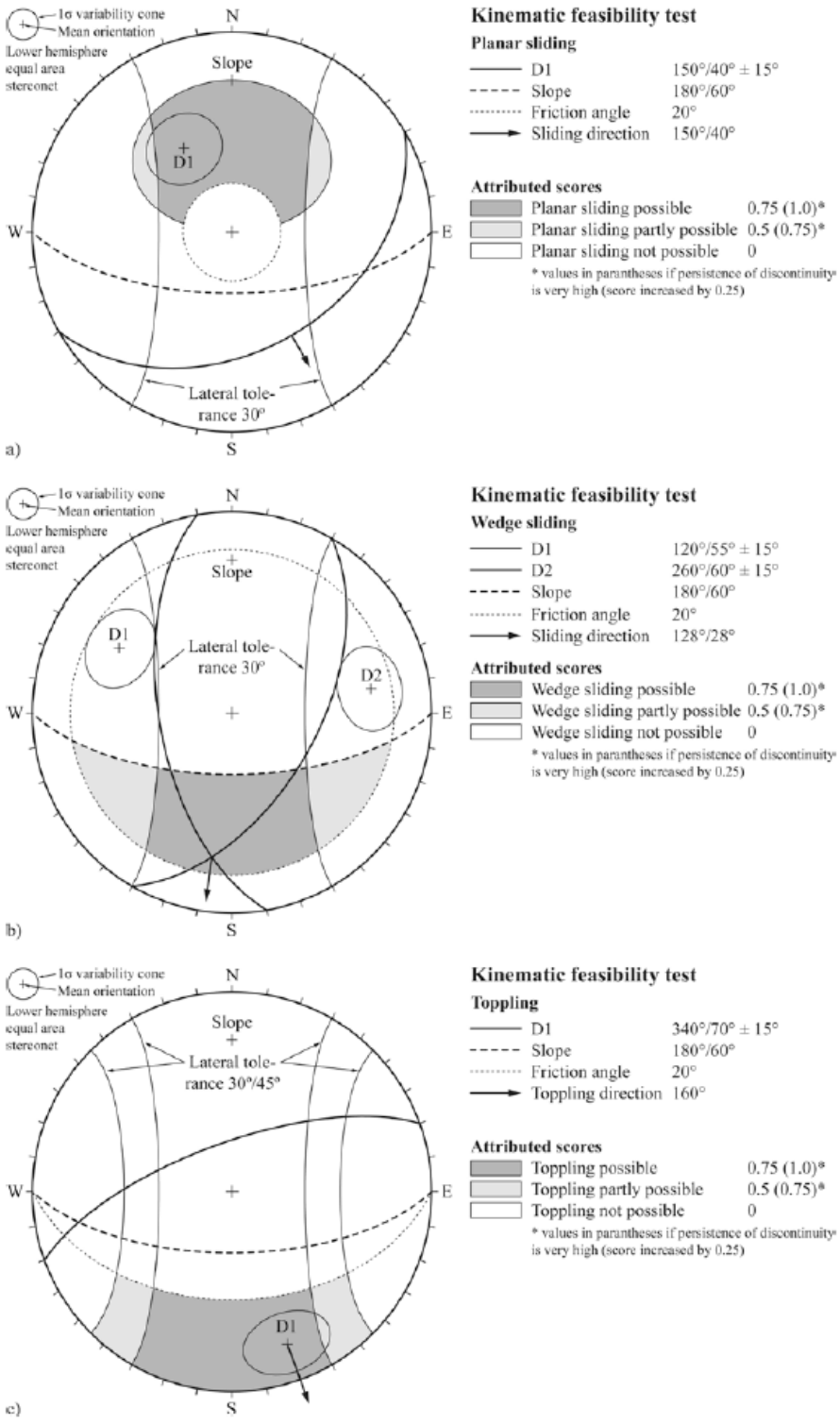

Figure 9: Kinematic feasibility test for the different failure modes possible for an URS. If the orientation of the set is located within ±30˚ of the slope aspect failure is considered to be possible. If the set is oriented outside ±30˚ of the slope aspect (in-between 30-45˚ for toppling) it is considered partly possible. A) Planar sliding. B) Wedge sliding. C) Toppling. Modified after Hermanns et al. (2012b)

2.5 Interferometric synthetic aperture radar (InSAR)

InSAR is a technique that can detect surface displacement by using radar data. Synthetic aperture radar (SAR) is a spaceborn instrument imaging the earth from above. It travels in orbits around the earth in an N-S or S-N direction (the azimuth direction), sending out and receiving a radar beam in a sideways direction (Line of Sight (LOS); Figure 10). The satellite records the position of the pixels by recording the range and azimuth direction, calculated from the satellite's own position. The range direction is found by timing the return of the reflected echo of the beam. The azimuth direction is calculated using a method called Doppler spread, a technique comparing the reflected echo from objects in front of the satellite with objects behind the satellite (Rosen et al., 2000). The position of the pixels are then converted into map coordinates using a method called geocoding. When the satellite orbits from south to north, it is ascending. Likewise, the satellite is descending when orbiting from north to south (Eriksen, 2013, Massonnet and Feigl, 1998, Lauknes, 2011).

Interferometry is a technique where signals are recorded over a specific area over time by multiple satellite flyovers, and compared with earlier recorded signals. The satellite sends out and records an electromagnetic pulse, with a certain wavelength and amplitude. If the reflected signal has a shift in phase, it may indicate a surface displacement. A shift in phase is referred to as a phase contribution. There may be multiple reasons for a phase contribution: a small change in position of the satellite for the different flyovers, disturbance as a result of turbulence or layering of the atmosphere or noise as a response of drift in frequency of the radar. To calculate surface displacement you must therefore subtract all the factors mentioned above from the phase contribution, before you get the change in phase caused by surface displacement. The surface displacement obtained from the interferometry is in one direction, LOS of the satellite. Therefore the actual surface displacement may be larger, if the movement vector is not parallel with the LOS (Figure 11 and Figure 12; Eriksen, 2013).

For this project, two InSAR-datasets were available from different satellites: RADARSAT-2 (R-SAT) and Sentinel-1. R-SAT is collected from 2009 to 2015, has a 5x10 m resolution, 24 days revisiting interval and has been processed using an S-BAS algorithm (Böhme et al., 2016a, Lauknes et al., 2010). The Sentinel-1-data is collected from 2015 to 2018, has a 5x20m resolution (ESA, 2019), 6 days revisiting interval and has been processed using a PSI-algorithm (Kampes, 2006). The LOS, for both R-SAT and Sentinel-1, is towards the ENE when the satellite is ascending. When it is descending, the LOS is towards the WNW for both satellites (Figure 11).

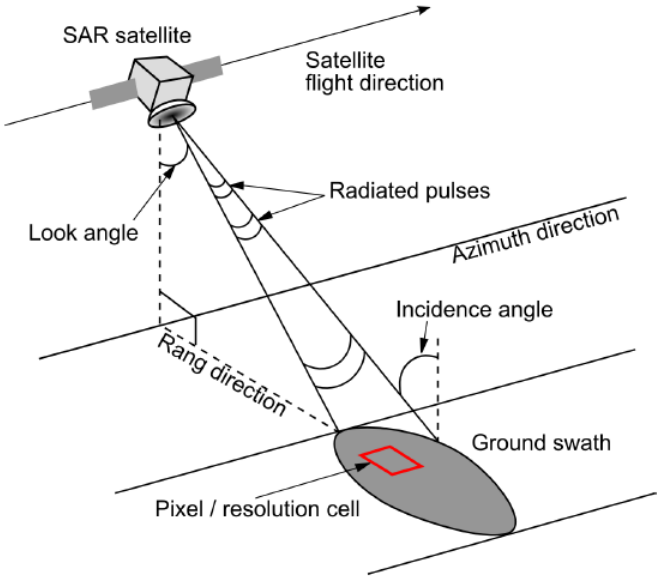

Figure 10: Schematic overview of different angles and directions for a SAR satellite. After Eriksen (2013).

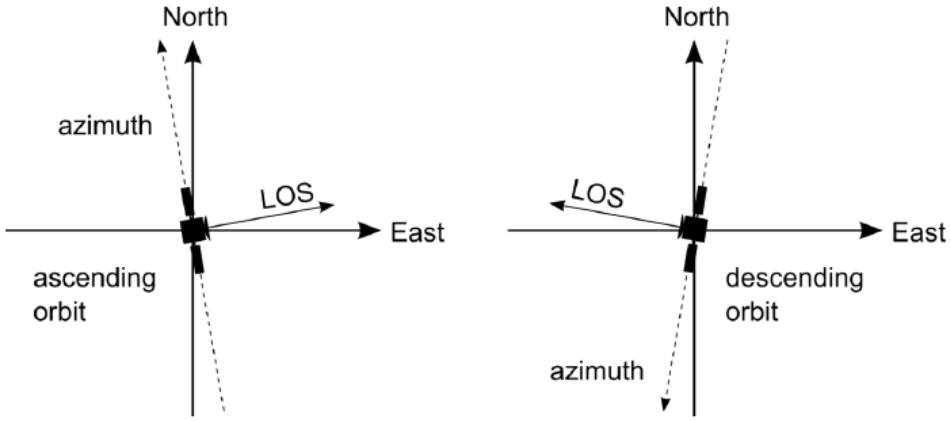

Figure 11: Sketch showing the azimuth and LOS for ascending and descending satellites. After Lauknes (2011).

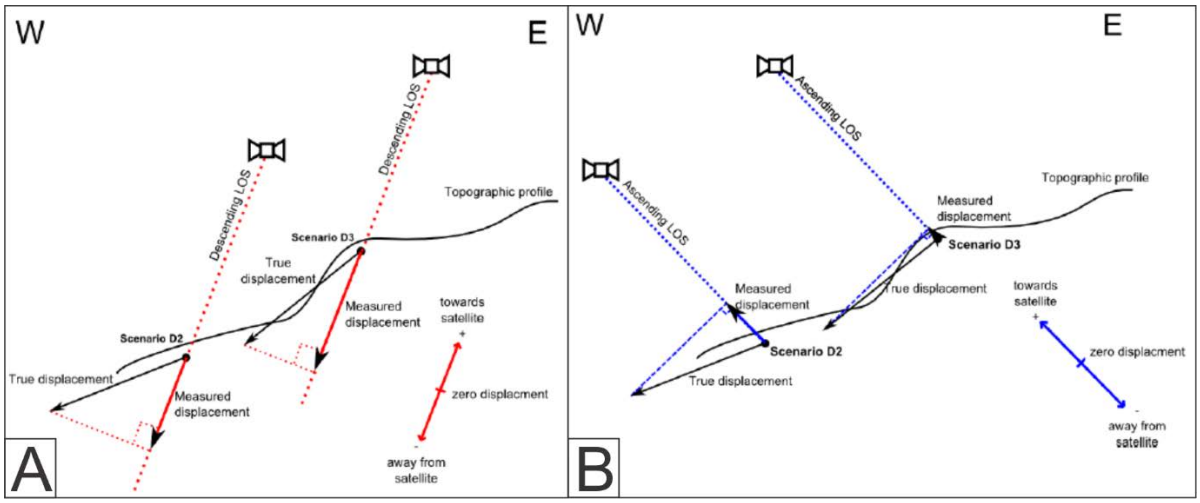

Figure 12: Schematic sketch showing LOS for descending and ascending satellites in relation to a west-facing slope. Modified after Eriksen (2013). A) LOS for a descending satellite. B) LOS for an ascending satellite.

2.6 Volume estimation

2.6.1 Sloping local base level (SLBL)

To correctly assess the risk and the consequence, it is necessary to estimate the volume of various failure scenarios of the URSs. With an estimation of the volume, it is possible to estimate the runout length of a potential collapse. The volume of the unstable area is defined by backscarps/fractures delimiting the URS from the stable part, and by the underlying failure surface. Since the position of the failure surface is often unknown, due to the lack of data from depth, an estimation is needed. To estimate the depth of the failure surface, and calculate the volume, it is possible to use SLBL. This is a technique developed at the University of Lausanne, in Switzerland, which estimates the failure surface by fitting an ellipse between the backscarp and the toe line of the URS (Jaboyedoff et al., 2004, Oppikofer et al., 2016a).

To calculate the SLBL, a DEM and a polygon of the unstable area are necessary. Three different geometries are calculated with SLBL in order to represent uncertainties connected to the basal failure surface: a minimum, an intermediate and a maximum SLBL (Figure 13). The absolute minimum SLBL has no curvature tolerance, resulting in a straight surface between the backscarp and the toe line. The maximum SLBL is calculated by using the maximum curvature tolerance (Oppikofer et al., 2016a).

The following workflow is based on an internal report provided by NGU. To calculate the volume based on the SLBL technique, NGU's customized GIS toolbox "Konsekvensutredning

Fjellskred Tools.tbx" was used, along with two excel macros. A short summary of the workflow of the processing executed in ArcGIS 10.5 and Excel is listed below:

- Create a polygon of the unstable area, based on delimiting structures
- Use the toolbox to get the altitude differences of the polygon. Measure the length of the polygon in its sliding direction
- Put the minimum and maximum altitude, polygon length, cell size of DEM, basal angle and backscarp angle into the excel spreadsheet to calculate the min., intermediate and maximum curvature tolerance of the ellipse.
- Convert the polygon of the unstable area to a raster-file and the DEM to an ASCII raster file.
- Create SLBL ASCII files for the min, intermediate and maximum curvature. These files will consist of the DEM without the unstable area, based on the curvature of the ellipse.
- Calculate the area of the 2D profiles for the min., intermediate and max SLBL. Put the area into the excel spreadsheet to calculate the volume, together with the area from the raster of the unstable area.

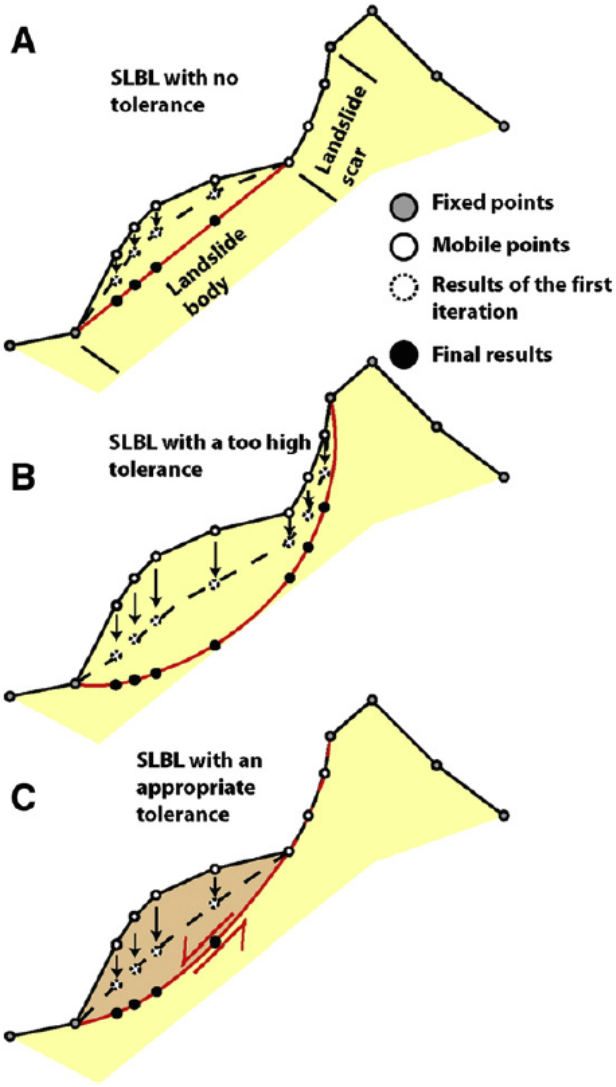

Figure 13: Schematic 2D profiles of SLBL estimations of volume. A) SLBL curvature with no tolerance at all, resulting in a planar failure surface. B) SLBL with a maximum tolerance, which could be too deep. C) A SLBL with an appropriate tolerance. Modified after Travelletti et al. (2010).

2.7 Run-out analysis

2.7.1 Scheideggers equation

Scheidegger (1973) found out that the height difference divided by the runout extent of a rock avalanche has an empirical relationship with the volume of the deposits. The height difference (H) divided by the runout length (L) equals the tangent of the angle of reach, which is illustrated in Figure 15. The angle of reach is calculated by the following equation, defined by Scheidegger (1973):

$$\tan\alpha = \frac{H}{L} = 10^{0,62419} * V^{-0.15666} \qquad (1)$$

Scheidegger curve indicates a logarithmic relationship between the H/L-ratio and the volume, as seen in Figure 14. The historic events that the regression line (Scheideggers curve) is based on, are marked as crosses. Data from Norwegian rock avalanches are plotted as dots, and are located well above the regression line. A higher H/L-ratio for a certain volume indicates a lower run-out length, hence is the Scheidegger curve a conservative approach for Norwegian rock slopes (Hermanns et al., 2012b).

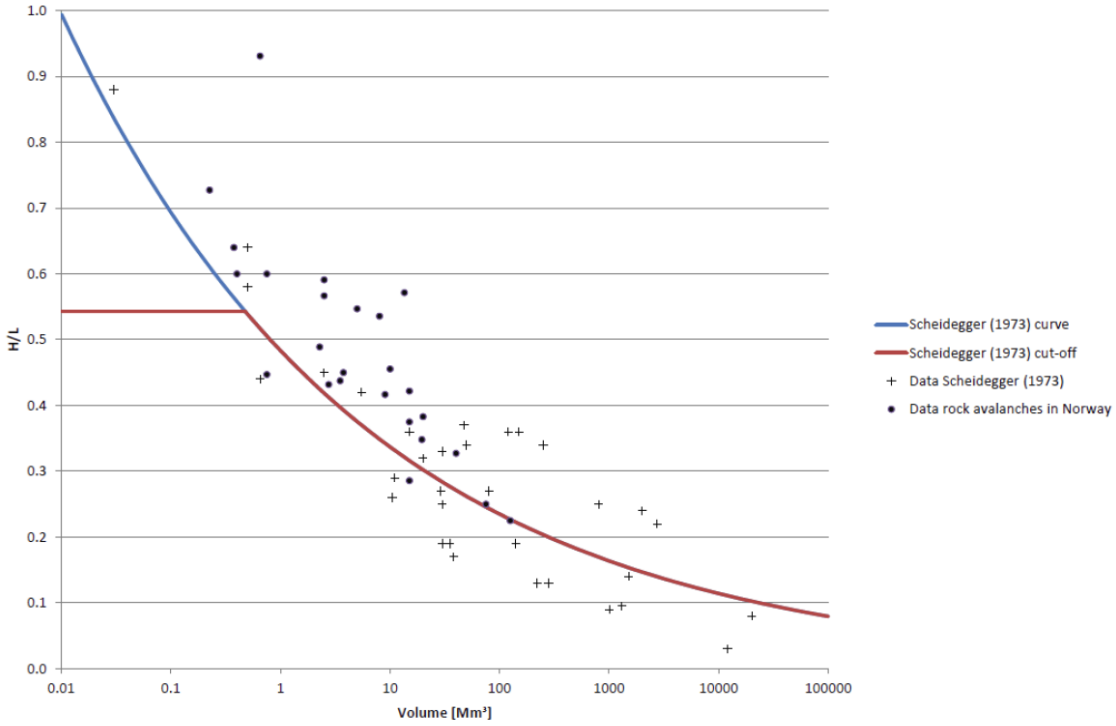

Figure 14: Scheideggers curve showing the logarithmic relationship between H/L-ratio and total volume of the rock avalanches. After Hermanns et al. (2012b).

To calculate the angle of reach for instabilities at Mellomfjellet, Scheideggers equation is used. The angle of reach is an important parameter used in the run-out analysis performed in Flow-R, which is further explained in chapter 2.7.2.

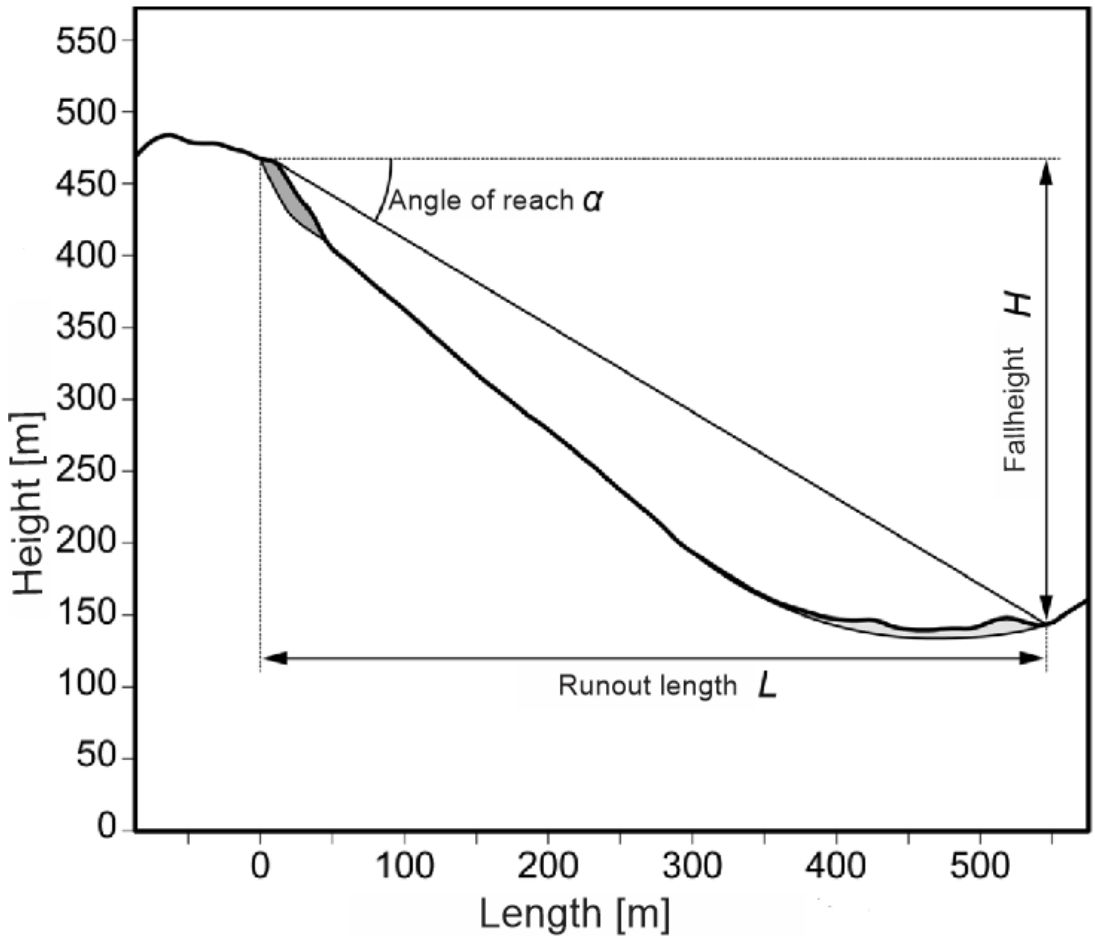

Figure 15: A schematic profile of an unstable rock slope showing how the angle of reach is calculated. Modified after Oppikofer et al. (2016a).

2.7.2 Flow-R

Run-out analysis is an important step when estimating the consequence of a rock slope failure. For this project, the software Flow-R has been used to perform such an analysis. Flow-R, developed at the University of Lausanne, is a software used for runout-modelling for debris flows and rock avalanches (Horton et al., 2013).

Flow-R uses a multiple flow direction algorithm to define the lateral extent of the rock avalanche, modified after Holmgren (1994). The algorithm lets the direction of the avalanche move on to one or multiple neighbouring cells, based on difference in height (Figure 16). It takes into account the previous flow direction of the avalanche, based on the *n* last cells. This way, the runout path of the avalanche is less affected by smaller hills and topographical obstacles. The software uses an opening angle θ, limiting the path of the avalanche from one

cell to the next. It has the highest probability to proceed straight forward, but may also change direction based on the height difference to the neighbouring cells. This way, Flow-R calculates the probability of the avalanche to spread from one cell to the next. If the probability is lower than the predefined threshold limit, the avalanche stops (Oppikofer et al., 2016a, Horton et al., 2013).

To calculate the potential and kinetic energy of the avalanche, the software uses a simplified friction model. The model assumes that the kinetic energy of the avalanche as it moves downslope is reduced due to friction of the ground surface. When the avalanche has passed a certain slope friction angle (φ), the model assumes that its energy is zero, and the avalanche stops. The friction angle (φ) is the same as the angle of reach (α) as described in equation 1, and is therefore used as the friction parameter for the slope.

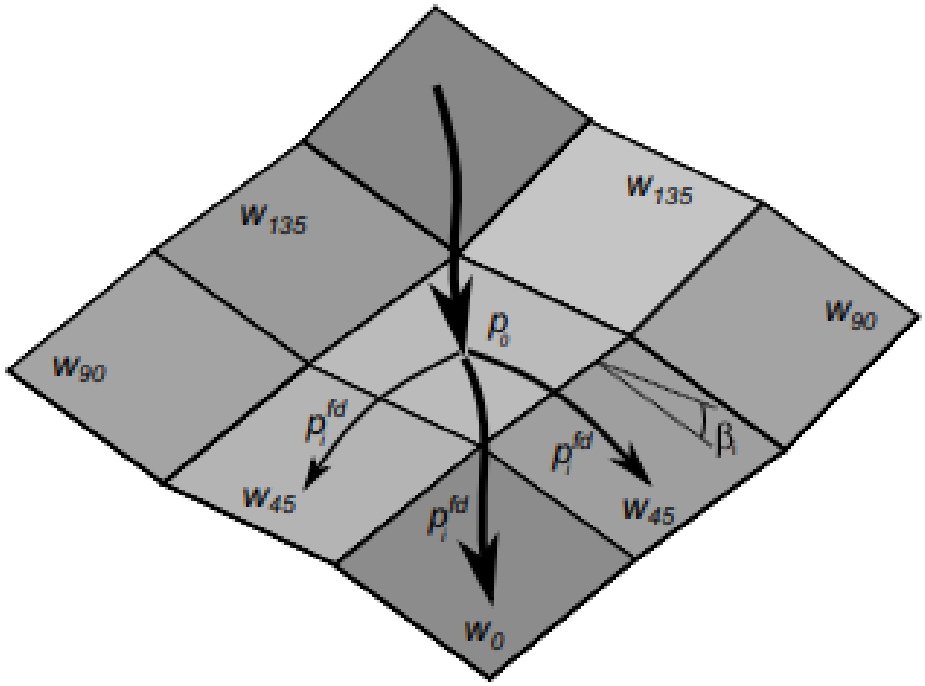

Figure 16: An illustration which shows how Flow-R calculates the spreading of the avalanche, based on the orientation of the neighbouring cells. Modified after Horton et al. (2013).

The following workflow is based on an internal report provided by NGU:

- Measure the maximum altitude difference, from the top of the unstable area to the lowest point in the valley below.
- Resample the DEM to 5x5 m spatial resolution, to make the calculations easier for Flow-R.

- Convert the source area (polygon of unstable area from volume estimation) and resampled DEM to ASCII-files.
- Import the data into Flow-R, and run the calculations with the following setting:
    - Directions algorithm: Holmgren (1994) modified
    - Opening angle: 120°
    - Number of cells remembered (n)= 25
- Load the output file from Flow-R into ArcMap to visualize the runout results.

2.8 Hazard classification

In order to quantify the hazard at Mellomfjellet, the hazard classification system developed by Hermanns et al. (2013) has been used. The system has a set of criteria describing the present state of an unstable rock slope. They describe the structural development of the slope, displacement rates and other signs of activity. The criteria of the analysis are:

- Backscarp presence
- Potential sliding structures present
- Lateral release surfaces present
- Kinematic feasibility test
- Morphological expression of the basal rupture surface present
- Displacement rates
- Acceleration
- Increase of rock fall activity observed
- Past events

Each of the criteria have two or more options describing the conditions for the given criterion. The conditions are given a score ranging from 0-1, except for displacement rates, where the score is ranging from 0-5. The sum of the score from all the criteria is classified as the hazard score, ranging from 0-12, where it is assumed that an URS is more likely to fail with a higher score. The hazard score is divided into five different hazard classes: Very low (0 - 2.4), Low (2.4 – 4.8), Medium (4.8 – 7.2), High (7.2 – 9.6) and Very High (9.6 – 12). Based on the assigned class, it is possible to determine if further investigation and/or monitoring is necessary (Hermanns et al., 2013).

3 Results

This chapter presents the geological (joints, foliations, folds etc.) and geomorphological (scarps, dislocated blocks, cracks etc.) features mapped in field work. Structural domains will be described. Furthermore, structural data have been gathered using drone photogrammetry, and are compared with field measurements. Displacement rates measured from two satellite InSAR-data sets are shown, and related to the geomorphological features. Feasible failure modes are presented in the kinematic analysis, based on the structural domains. Lastly, failure scenarios are presented in terms of volume and run-out extent model results.

3.1 Structural analysis

To analyse the structural data gathered from Mellomfjellet, stereonets from 31 different stations were analysed in order to detect structural variations across the study area (Figure 5 and Appendix A and B). By comparing the difference in orientation for the mapped foliation and joint sets, in relation to the orientation of the backscarps, lineaments and slopes, the analysis resulted in two different structural domains: Mellomfjellet 1 and Mellomfjellet 2 (Figure 17). Of the 31 structural stations, 17 stations were included in the two domains. Assigning the different sets for the mapped discontinuities was based on the calculated densities of the contour plot, as mentioned previously in chapter 2.3. Due to the large spatial variations, and a large number of measurements per domain (>100), most of the assigned sets have a density lower than 6%, which classifies as slightly significant at best (Rocscience, 2018b). Stereoplots of the two structural domains, containing the mean planes of the mapped structures are presented in Figure 18 and Figure 19. All of the assigned sets are mapped and identified in field, and are described in detail in chapter 3.2.2.

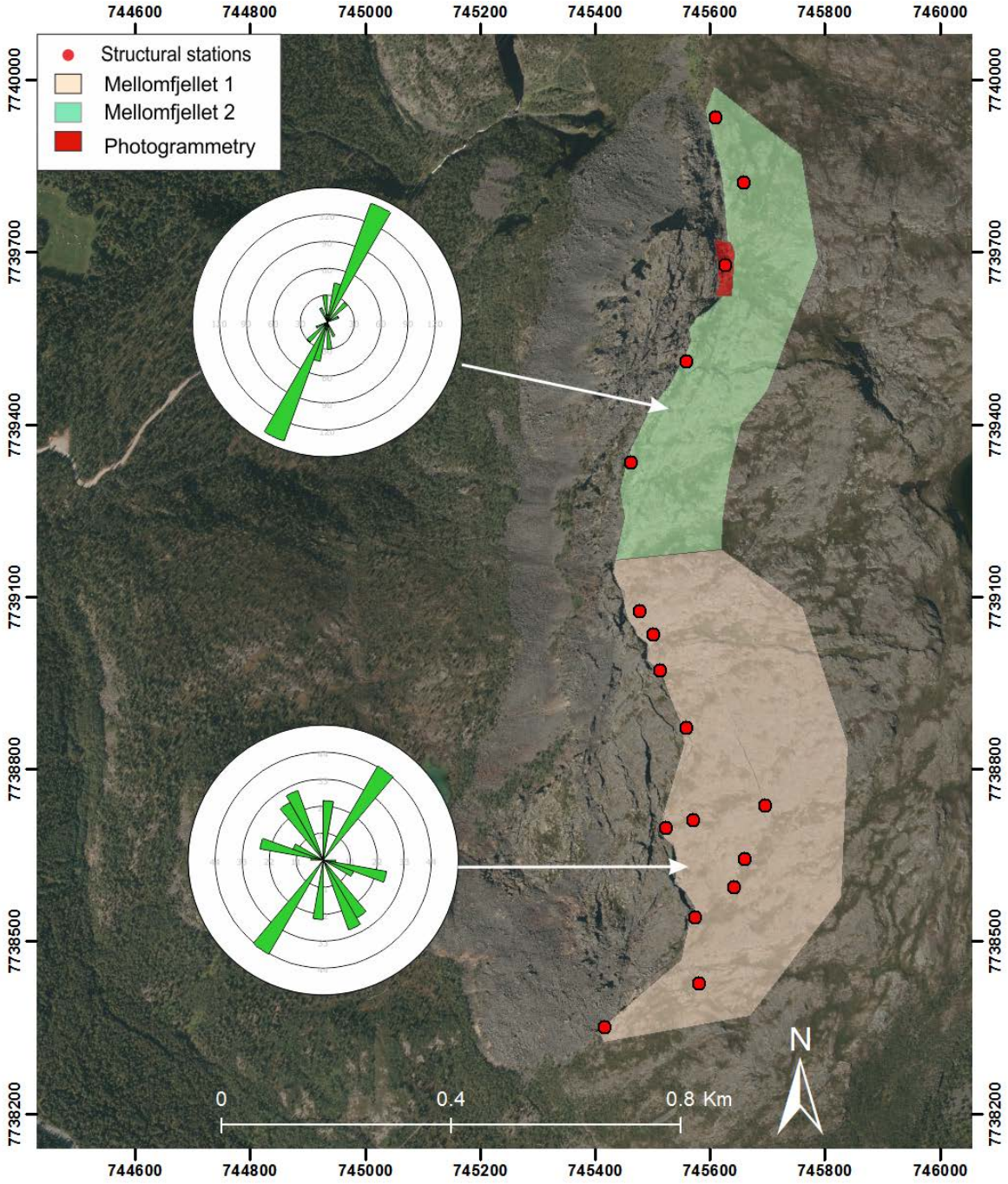

Figure 17: Overview map of the determined structural domains, including the structural stations, rosette plots of mapped lineaments and the area where photogrammetry was done.

3.1.1 Mellomfjellet 1

At Mellomfjellet 1, 313 structural measurements were taken from 12 different stations. The stations are from assumed in situ bedrock close to the unstable area. Four different sets were assigned for this domain, using cluster analysis. The foliation (denoted SF), and joint set 2 (denoted J2) are the only sets that are slightly statistically significant, with contour densities between 4-6%. Joint set 1 (J1) and joint set 3 (J3) are not statistically significant, but are well documented and described in field. The fold axis was calculated using the tool *Fold analysis* in Dips, with a trend and plunge of 235 -> 14.

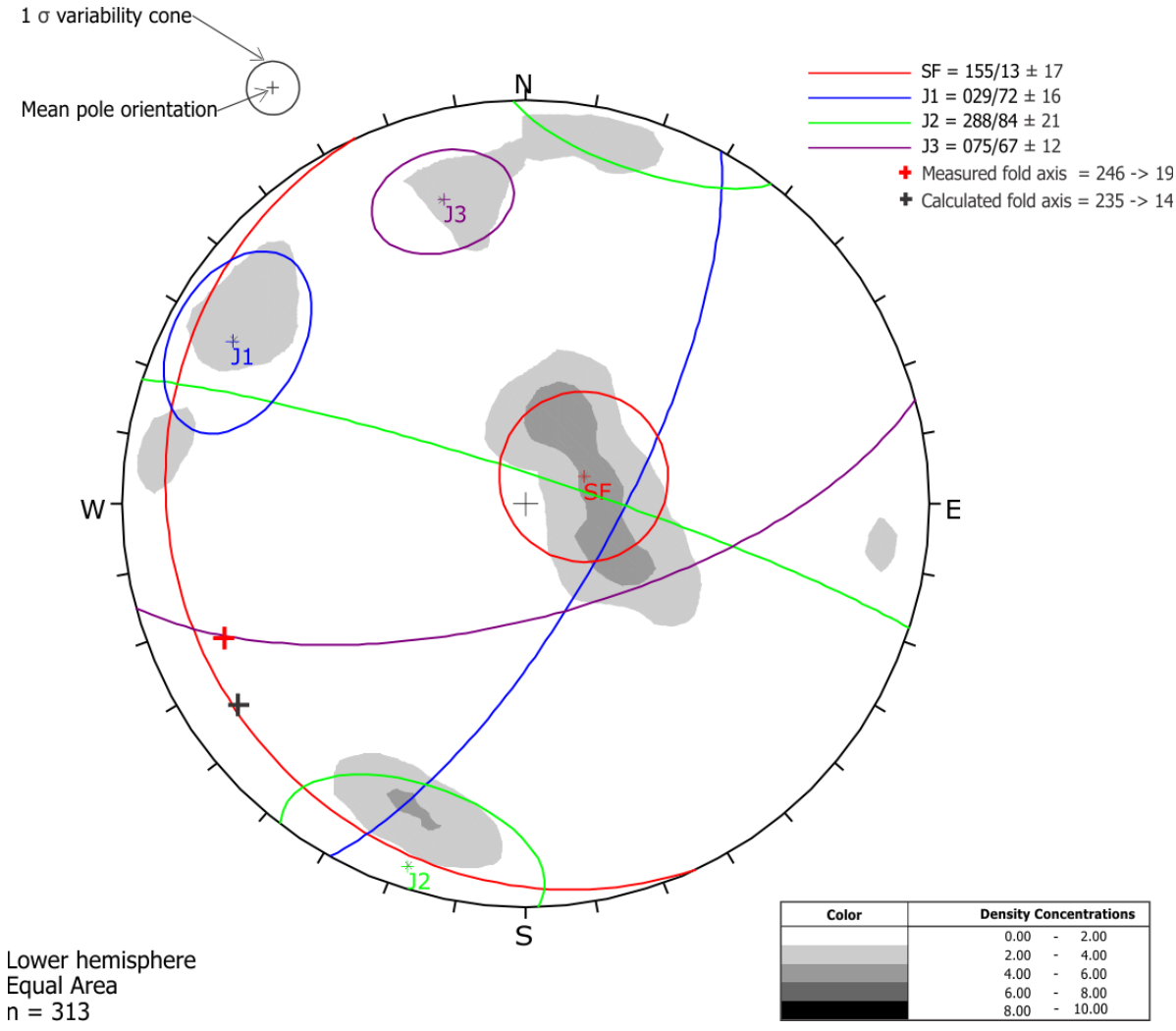

Figure 18: Stereographic plot of the poles for the measurements done at Mellomfjellet 1

3.1.2 Mellomfjellet 2

At Mellomfjellet 2, 205 structural measurements from 5 structural stations have been collected. All of the stations are located close to the unstable area, and are from assumed in situ bedrock. Four sets were identified and assigned from the cluster analysis of the contour plots. Both SF and J1 have the highest densities (8-10%), classifying as very statistically significant. J2 are slightly statistically significant, with density between 4-6%. Based on the cluster analysis alone, J3 is not statistically significant, with a density ranging between 2-4%. However, it was observed at several stations in the field (Figure 30), which is why it has been assigned here as a set. The fold axis was calculated with a trend and plunge of 248 -> 10.

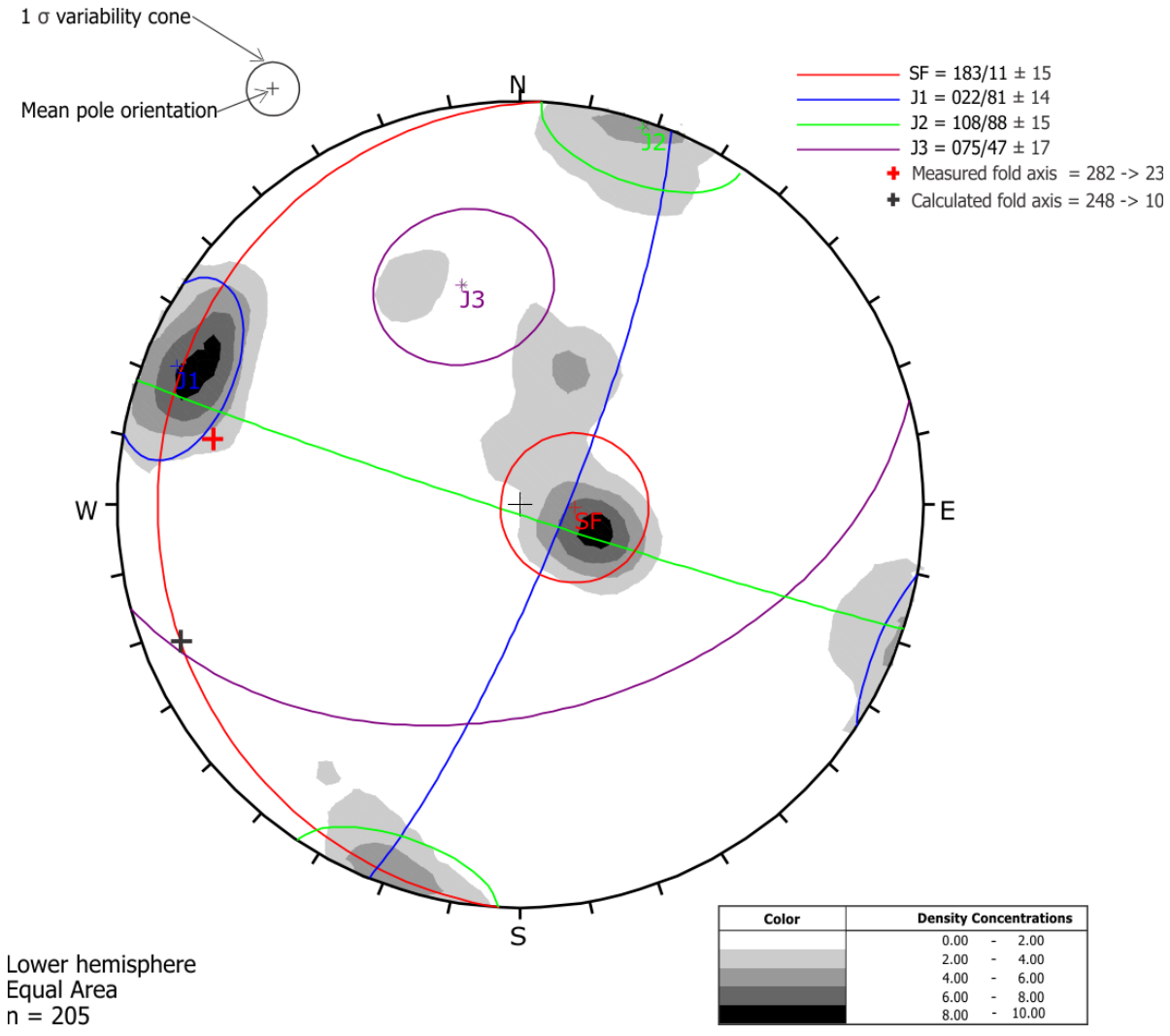

Figure 19: Stereographic plot of the poles for the measurements done at Mellomfjellet 2.

3.1.3 Data from photogrammetry

3.1.3.1 3D Model

An inaccessible part of the backscarp at Mellomfjellet 2 was investigated in more detail using drone photogrammetry (red polygon, Figure 17). The 3D model is presented in Figure 20. The model has a point density of 0.277 points/cm^2, or 2770 points/m^2. As a result of its high point density, the structures of the backscarp are highly visible and easy to detect, in spite of varying lighting conditions.

The area has recently experienced localised failure, which has been captured in photo series from 2009 and 2018. This failure is also visible in the 3D model, identified by its bright colours to the far left in the detail in Figure 20, marked with a red circle. On its right side, a similar failure is discovered, but of older age due to its darker colour.

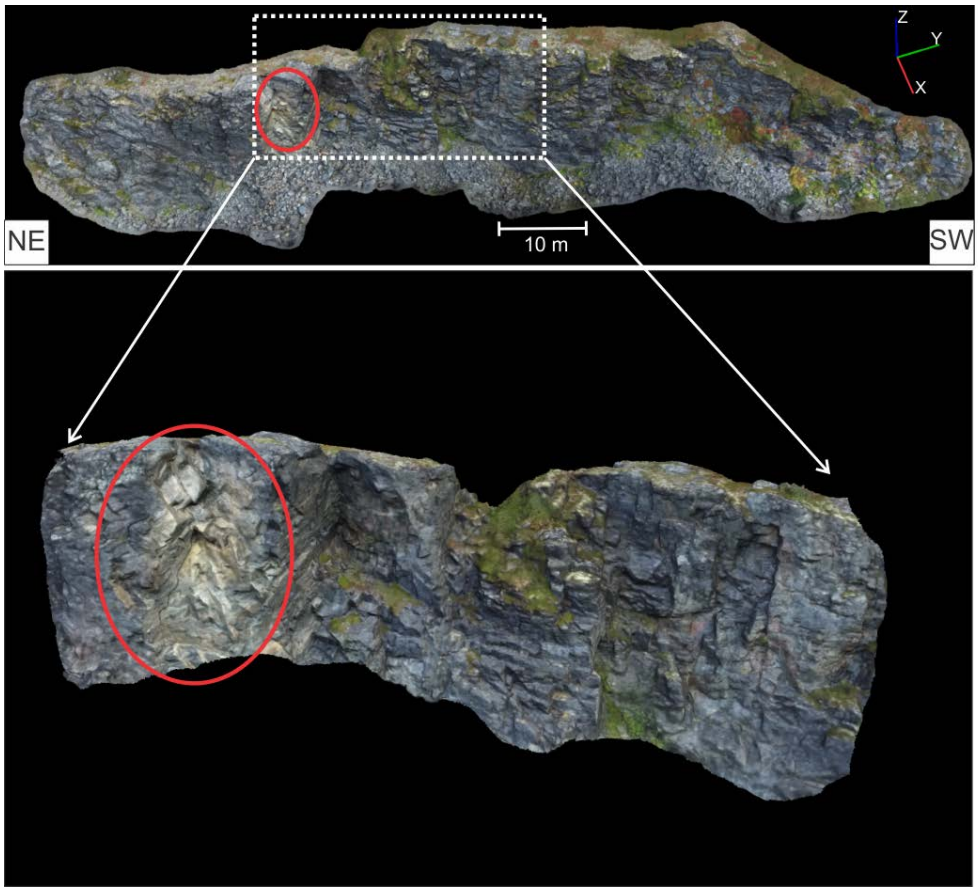

Figure 20: 3D model of the backscarp at Mellomfjellet 2. A recent failure along J1, J2 and the foliation is visible in the detail below, marked with a red circle.

3.1.3.2 Coltop3D

To analyse the orientation of the structures, the point cloud was imported into Coltop3D (Figure 21). Based on the colour of the faces, three sets were recognised: a bright-pink colour representing the foliation, yellow and green representing J1 and the turquoise colour as J2 (Figure 21 detail). J3 was not recognized in Coltop3D. The mean orientation of the sets are presented in Table 2, together with the structures from field for the same domain (Mellomfjellet 2). The foliation from Coltop3D is showing an 11˚ steeper dip, 17˚ more towards the south than the data measured from field. J1 from Coltop3D has a 9˚ more gentle dip, dipping 16˚ more towards east than J1 from field. J2 has a very similar strike for the two data capture methods, with only 1 degree difference. The dip is also quite similar, where both are a few degrees from vertical (Table 2). Taking the variance into account, the sets are similar for both methods (Figure 22).

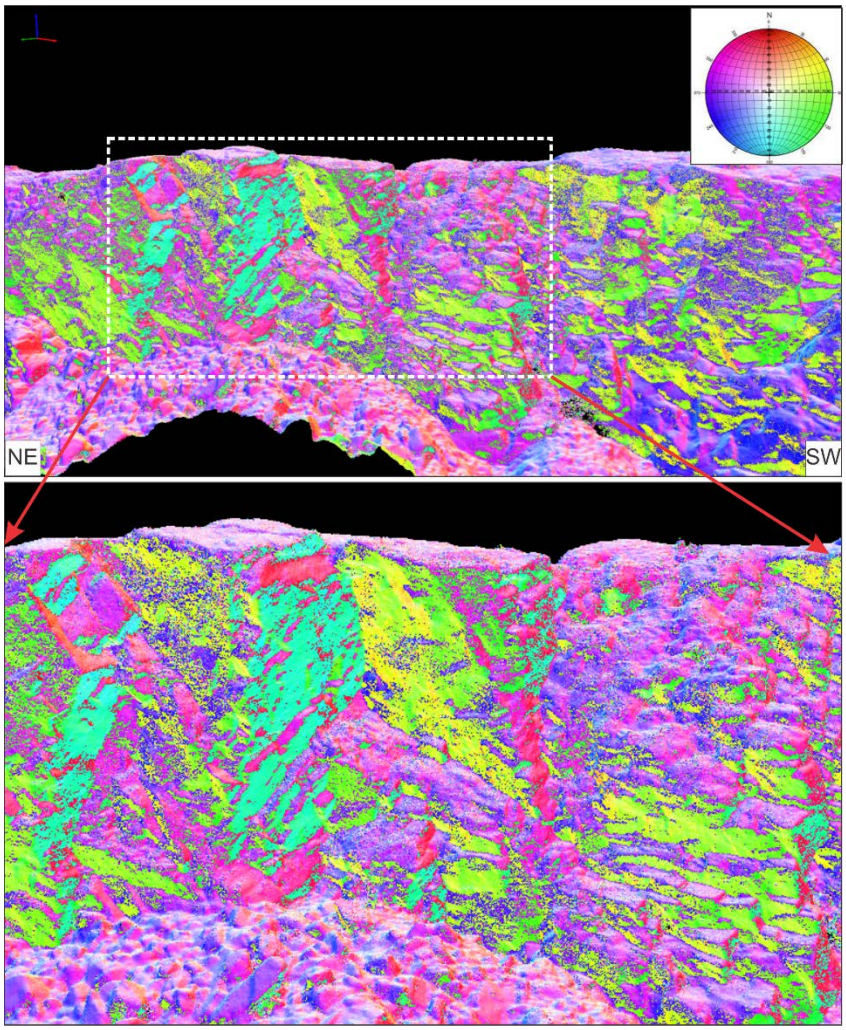

Figure 21: The 3D model of the backscarp where the orientation of the faces are classified with a unique colour based on the orientation.

Table 2: Comparison of the mean orientation of the discontinuity sets gathered in field and from Coltop3D. Numers in parentheses represent the actual difference, when taking into account the right hand rule.

	Coltop3D		Field measurements		Difference	
Joint set	Strike	Dip	Strike	Dip	Strike	Dip
SF	166 ± 13	22 ± 13	183 ± 15	11 ± 15	-017	+11
J1	006 ± 17	72 ± 17	022 ± 14	81 ± 14	-016	+9
J2	289 ± 16	85 ± 16	108 ± 15	88 ± 15	+181(+1)	-3(-8)

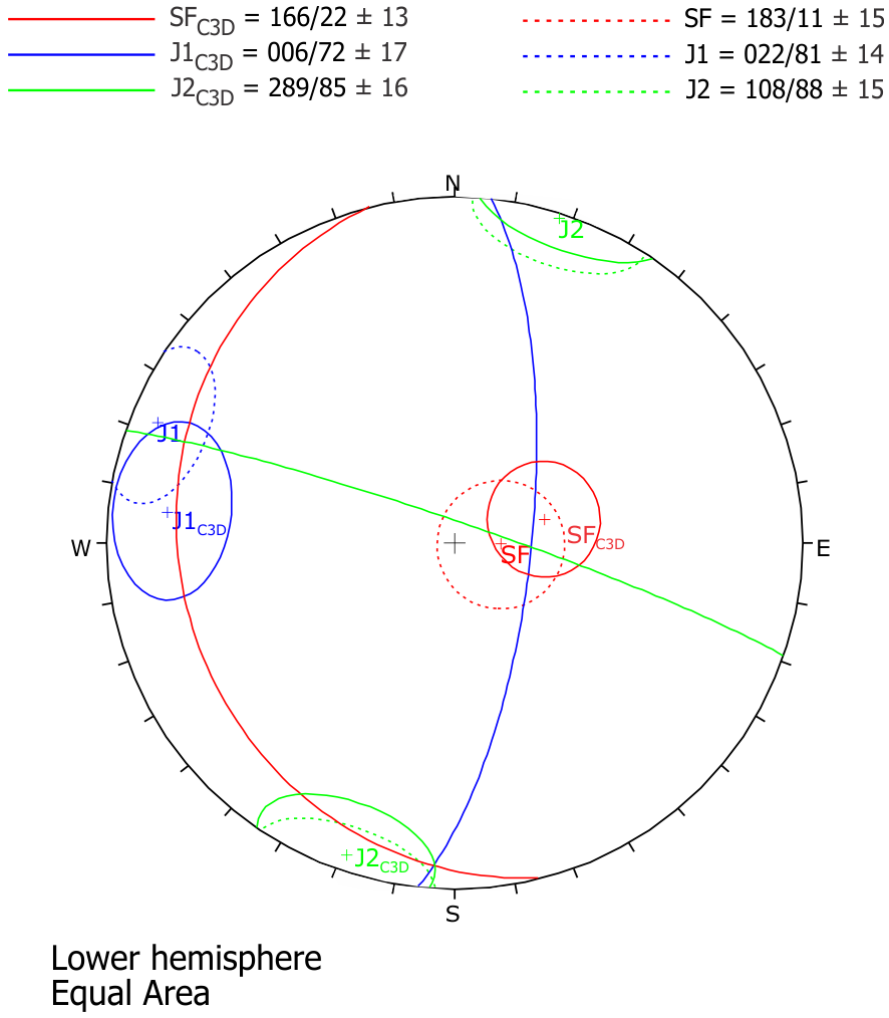

Figure 22: Comparison of structural sets gathered from the 3D model (denoted C3D) and the sets measured in field at Mellomfjellet 2 (dotted lines). Inspired by Jaboyedoff et al. (2009).

3.1.4 Kinematic analysis

This chapter presents the results from the kinematic analyses for the two structural domains. The input parameters for the analysis are presented in Table 3. The slope inclination and orientation was determined using spatial analysis of the ArticDEM in ArcMap. The areas that classify as *possible* for failure are given a darker hue in the stereonet, while areas classifying as *partly possible* are given a lighter hue. The results from the kinematic analysis are presented in Figure 23 and Figure 24. Only the sets where failure is possible are presented in the figures.

Table 3: Input values for the kinematic feasibility analysis.

Domain	Slope orientation		Friction angle	Lateral limit
	Strike	Dip		
Mellomfjellet 1	170	64	20	30
Mellomfjellet 2	200	74	20	30

3.1.4.1 Mellomfjellet 1

At Mellomfjellet 1, parts of the foliation plot within the area possible for planar failure (Figure 23A), resulting in a sliding direction towards WSW, however it is not possible along the mean plane of the set. Wedge failure is not possible along the intersection of any of the mean set planes (Figure 23B). However, due to variations within the sets, 18.75 % of all intersections plotted within the critical zone for wedge failure to occur (Table 4). Flexural toppling is partly possible along J1 and J2 (Figure 23C). The percentage of structures critical to failure are presented in Table 4, showing a similar percent of critical measurements for all the failure modes (ranging from 17.25 to 19.81 %).

Table 4: Results from the kinematic analysis, showing the percentage of structures which are oriented in a way that may lead to failure. Note that this table includes both possible and partly possible failures.

Mellomfjellet 1 (170/64)			
Intersections	**Total**	**Critical**	**Percent critical**
Planar sliding (all)	313	54	17.25 %
Planar sliding (SF)	79	35	44.3 %
Wedge sliding	48819	9156	18.75 %
Flexural toppling	313	62	19.81 %
Flexural toppling (J1)	45	28	62.22 %

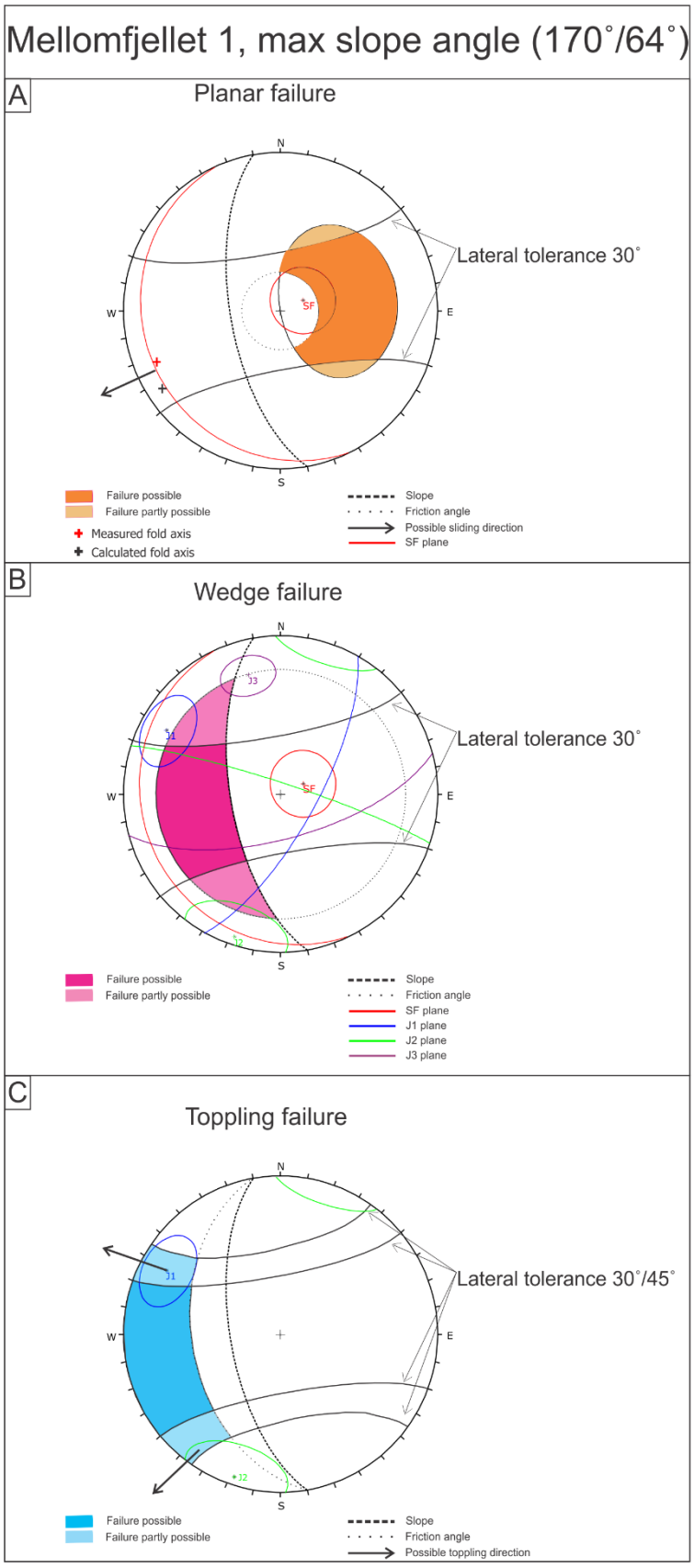

Figure 23: Kinematic feasibility test for Mellomfjellet 1. A) Planar failure is possible along the foliation. B) Wedge failure is not possible along the intersection of the mean planes. C) Toppling failure is partly possible along J1 and some variations of J2.

3.1.4.2 Mellomfjellet 2

At Mellomfjellet 2, planar failure is possible along parts of the foliation, resulting in a possible sliding direction towards west, however not possible along the mean plane (Figure 24A). Wedge failure is not possible along the intersection of the mean planes (Figure 24B). The kinematic analysis (Table 5) shows that 12.96 % of the intersections are feasible for wedge failure to occur. Toppling failure is possible for J1, with a toppling direction to WNW (Figure 24C). It is partly possible for J3, where parts of the variability cone plotted inside the critical area. The results of percentage of critical measurements (Table 5), the analysis shows that 78.33 % of J1 are oriented in a way that is feasible for flexural toppling.

Table 5: Results from the kinematic analysis, showing the percentage of structures which are oriented in a way that may lead to failure. Note that this table includes both possible and partly possible failures.

Mellomfjellet 2 (200/74)			
Intersections	**Total**	**Critical**	**Percent critical**
Planar sliding (all planes)	205	19	9.27 %
Planar sliding (SF)	47	15	31.91 %
Wedge sliding	20900	2709	12.96 %
Flexural toppling	205	56	27.32 %
Flexural toppling (J1)	60	47	78.33 %

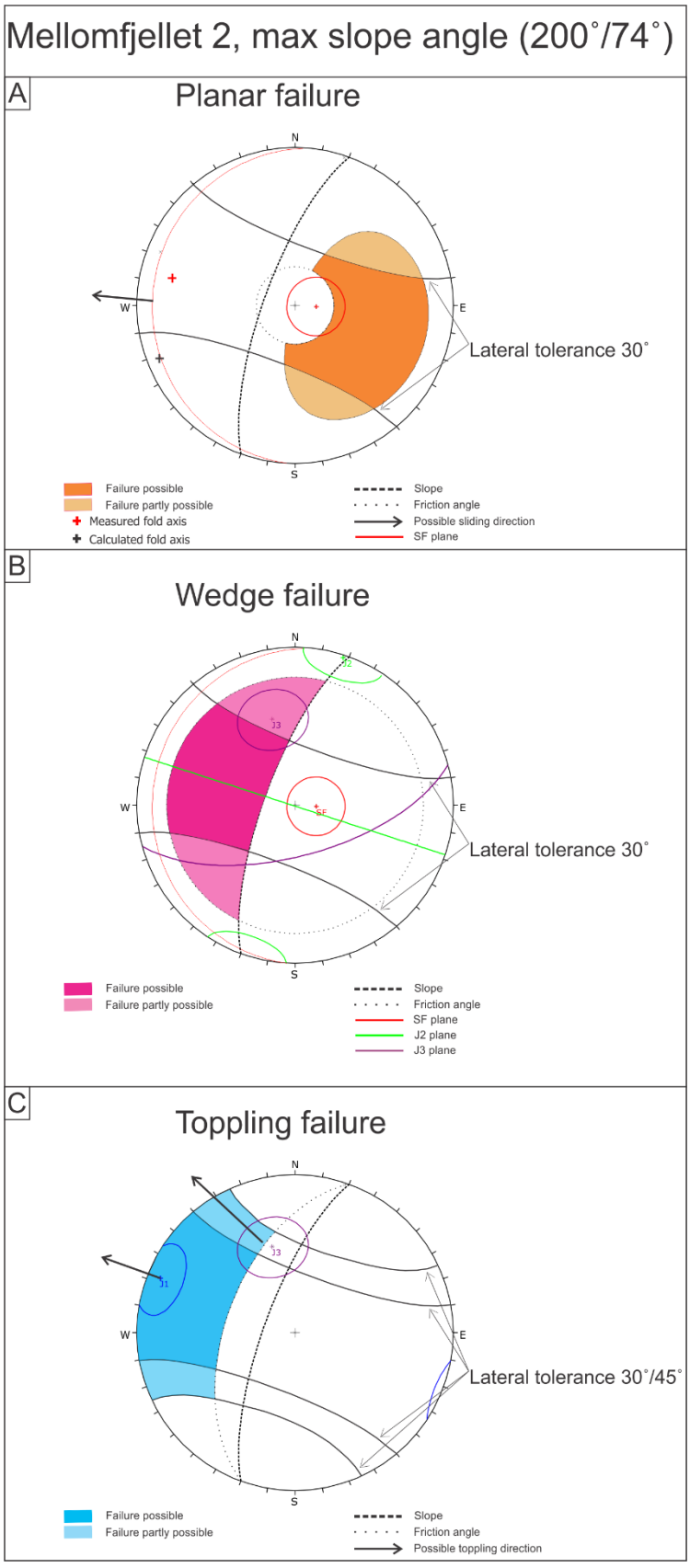

Figure 24: Kinematic feasibility test for Mellomfjellet 2. A) Planar failure possible along a small part of the foliation, but not along the mean plane. B) Wedge failure not possible along the intersection of any of the mean planes. C) Flexural toppling possible along J1 and partly along J3.

3.2 Results from field investigations

3.2.1 Lithology

The 1:50 000 geological map (Zwaan et al., 1984) shows two lithologies present at Mellomfjellet: amphibolite and hornblende schist, with a lens of calcite marble. Hand samples taken in the field confirmed the presence of amphibolite and hornblende schist, however the lens of calcite marble was determined to be felsic intrusion.

3.2.1.1 Lithological description: Amphibolite and hornblende schist

A greenish-grey rock containing mafic mineral assemblages (hornblende and biotite) and occasional garnets (Figure 25). The degree of foliation varies, in some places the foliation is well developed with a platy schistose texture. However the rockmass was in some areas more massive, resembling an amphibolite. Based on the mineral composition and texture the rockmass was classified as ranging between an amphibolite and hornblende schist.

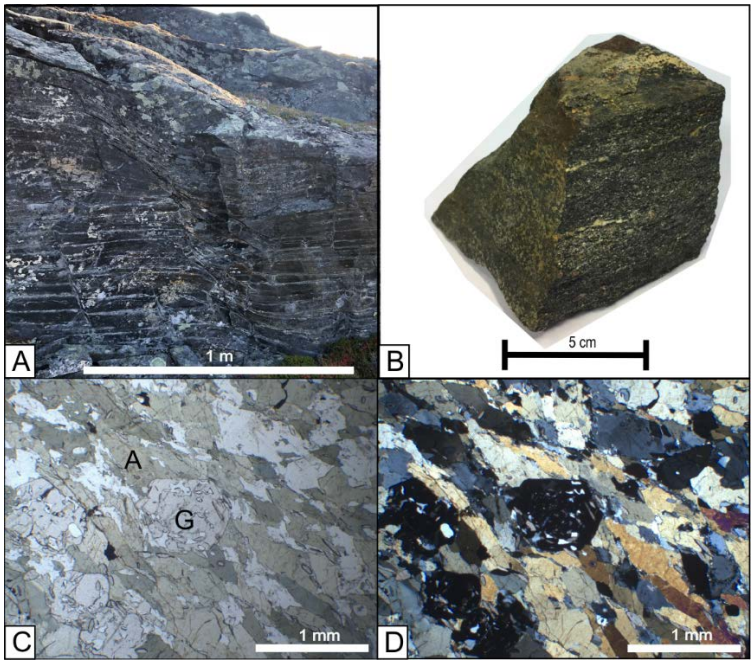

Figure 25: Amphibolite, the main lithology at Mellomfjellet. A) Photo showing an outcrop of the amphibolite. B) Hand sample used to identify minerals, and to create thin sections from. C) Thin section in plane polarized light (PPL) showing amphibole (marked A) and garnet (marked G) as main minerals. D) Thin section in crossed polarized light (XPL).

3.2.1.2 Lithological description: Felsic intrusion

A whitish-yellow lens containing felsic mineral assemblages (quartz, feldspar and biotite, with some pyrites present; Figure 26). Based on the mineral composition and texture of the rockmass the rock mass was classified as a felsic intrusion. The contact zone between the felsic intrusion

and the above laying amphibolite is presented more in detail in chapter 3.2.2.6 explaining how it may act as a zone of weakness.

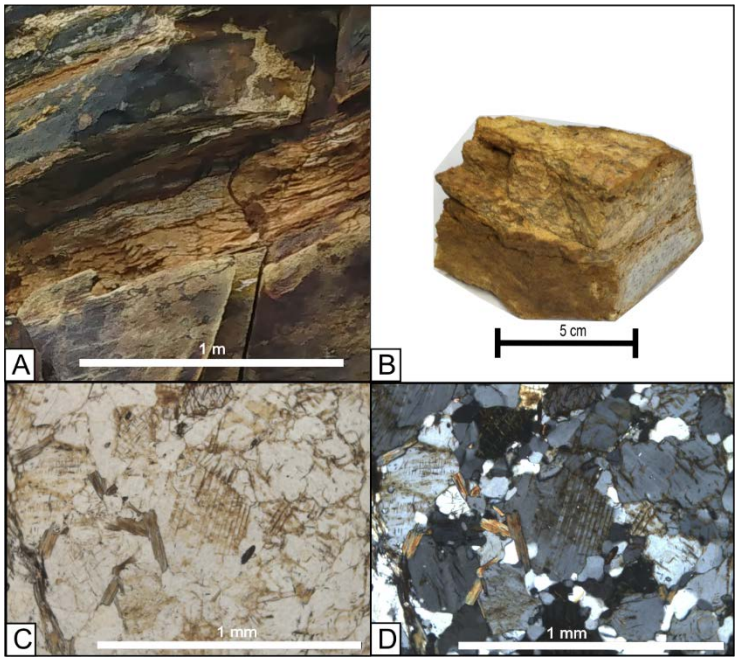

Figure 26: The second lithology found at Mellomfjellet, a felsic intrusion. A) Photo of the outcrop. B) Hand sample used to classify minerals and to make thin sections. C) Thin section in PPL showing biotite, feldspar and quartz. D) Thin section in XPL confirming the same minerals identified in PPL in figure C.

3.2.2 Geological structures

3.2.2.1 Foliation

The foliation is moderately to well-developed across the site (Figure 27). It is gently folded with an average wavelength varying between 5-15 m. As a result, the orientation of the foliation varies at different stations. To get an average orientation of the foliation, a large number of measurements were gathered across the site. The average orientation for the different domains are presented in Table 6. Overall the foliation had a gentle dip downslope.

Table 6: Orientation of the foliation observed at the different domains.

Domain	**Strike/dip**
Mellomfjellet 1	155/13 ± 17
Mellomfjellet 2	183/11 ± 15

Fold axes were measured at four different locations, three at Mellomfjellet 1 and one at Mellomfjellet 2 (Table 7). Like the dip of the foliation, the fold axes were plunging gently downslope (Figure 27A**)**.

Table 7: Orientation of the fold axes observed at the different structural domains.

Domain	**Trend –> plunge (measured in field)**	**Trend –> plunge (Calculated in Dips)**
Mellomfjellet 1	255 -> 15	235 -> 14
	236 -> 21	
	245 -> 20	
Mellomfjellet 2	282 -> 23	248 -> 10
Both domains combined		237 -> 13

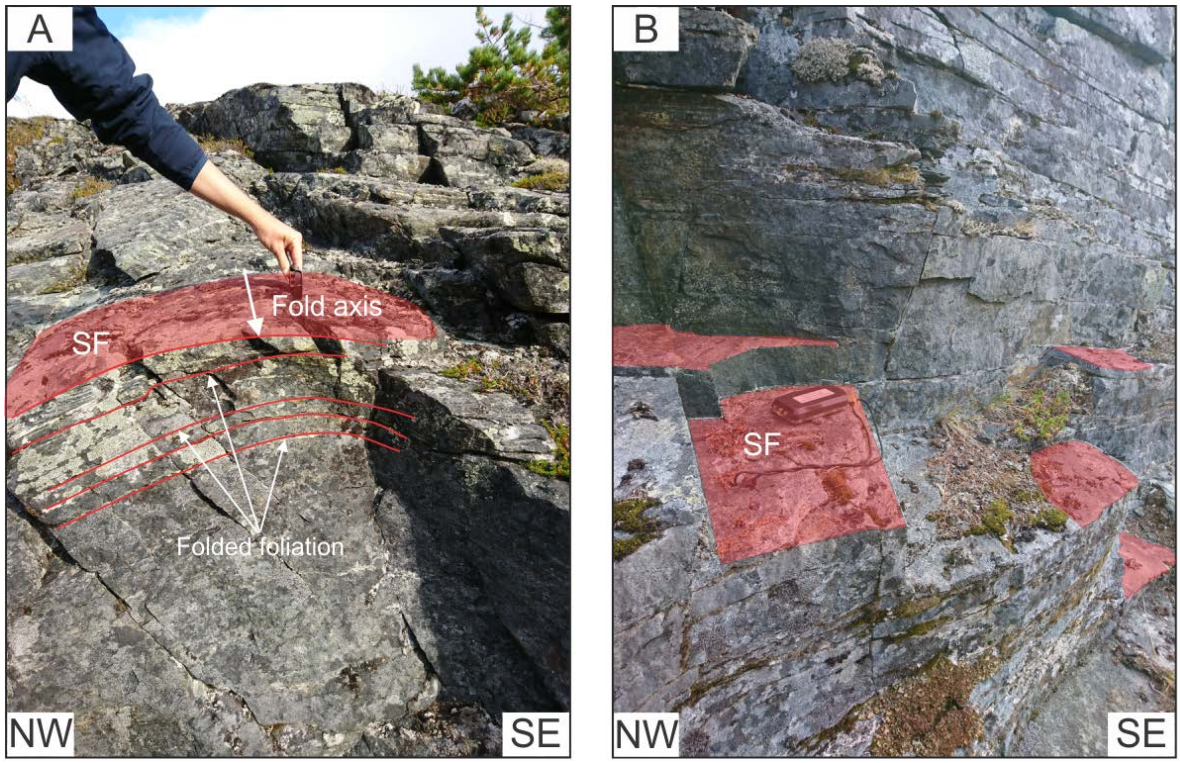

Figure 27: Different foliation planes exposed in field. A) The folded foliation and the measured fold axis. B) Multiple foliation step surfaces exposed.

3.2.2.2 Joint sets

From the structural analysis combined with field descriptions, three joint sets were identified at both structural domains. J1 is a sub-vertical dipping joint set with an average strike towards NNE-SSW. J2 strikes towards WNW-ESE with a sub-vertical dip. J3 strikes towards ENE-WSW with a moderately to steeply dip. The mean strike and dip of the different joint sets for both domains are presented in Table 8.

Table 8: Orientation of the joint sets measured in field at the two domains.

Domain	**J1**	**J2**	**J3**
Mellomfjellet 1	029/72 ± 16	288/84 ± 21	075/67 ± 12
Mellomfjellet 2	022/81 ± 14	108/88 ± 15	075/47 ± 17

The spacing, persistence, shape and roughness was quite variable for each structural set throughout the area. For each station the mapped discontinuities were given an estimated value for each of the parameters, in order to better differentiate them. The estimates for the different sets measured in the two domains are presented in Table 9, where the values are based on Appendix I.

Table 9: Spacing, persistence, shape and roughness of the mapped discontinuities. The attributes given is this table is based on rough estimates in field.

Set	**Spacing [m]**		**Persistence [m]**		**Shape**		**Roughness**	
	MF 1	**MF 2**	**MF1**	**MF2**	**MF 1**	**MF 2**	**MF 1**	**MF 2**
Foliation	0.1 – 1	0.1 – 1	-	-	Undulating	Undulating	Smooth	Smooth
J1	0.5 – 5	0.1 – 2	>50	>20	Undulating	Stepped	Rough	Smooth
J2	0.2 – 2	0.4-5	>50	10-20	Undulating	Planar	Smooth	Rough
J3	0.1 – 2	0.2-2	>5	>10	Planar	Planar	Rough	Smooth

3.2.2.3 Joint set 1

Joint set 1 is found along the backscarp for both structural domains (Figure 28 and Figure 29). The joint set is steeply dipping into the slope, with a mean strike towards NE-SW. There is a small variation in orientation for the set when comparing the two domains, but considering their variance, they are the same (Table 8). The mean dip at Mellomfjellet 2 is slightly steeper and oriented more towards the east than at Mellomfjellet 1. It is the most prominent joint set at Mellomfjellet 2, especially noticeable as it forms most of the backscarp (Figure 29).

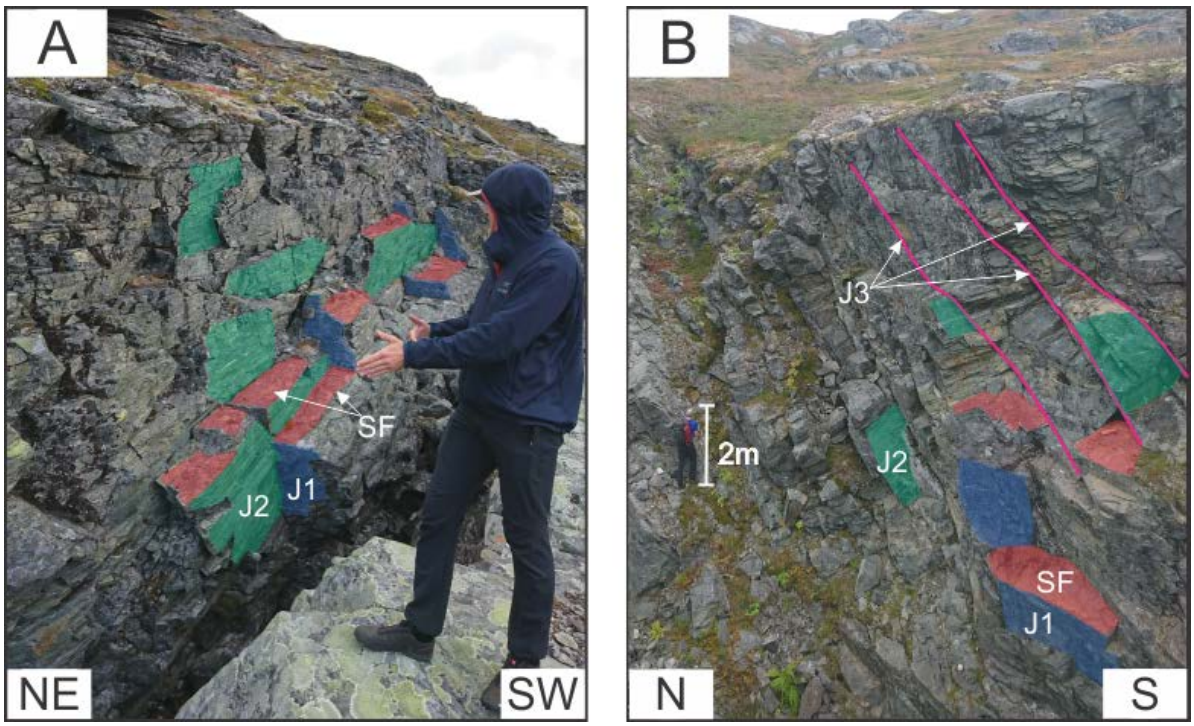

Figure 28: Foliation and different joint sets at Mellomfjellet 1. A) Exposure along the backscarp showing two joint sets (J1 and J2) and the foliation. B) Exposure in the intersection of the backscarp and E-W striking lineament showing a third joint set (J3).

3.2.2.4 Joint set 2

Joint set 2, orthogonal to joint set 1, also forms part of the backscarps at both Mellomfjellet 1 and 2. The set strikes WNW-ESE in both domains, is steeply dipping towards NNE at Mellomfjellet 1, and is vertical at Mellomfjellet 2 (Figure 29). The spatial variation of the joint set between the two domains are much less noticeable than for Joint set 1 (Table 8). It is the most prominent in the backscarp of Mellomfjellet 1 (Figure 28A).

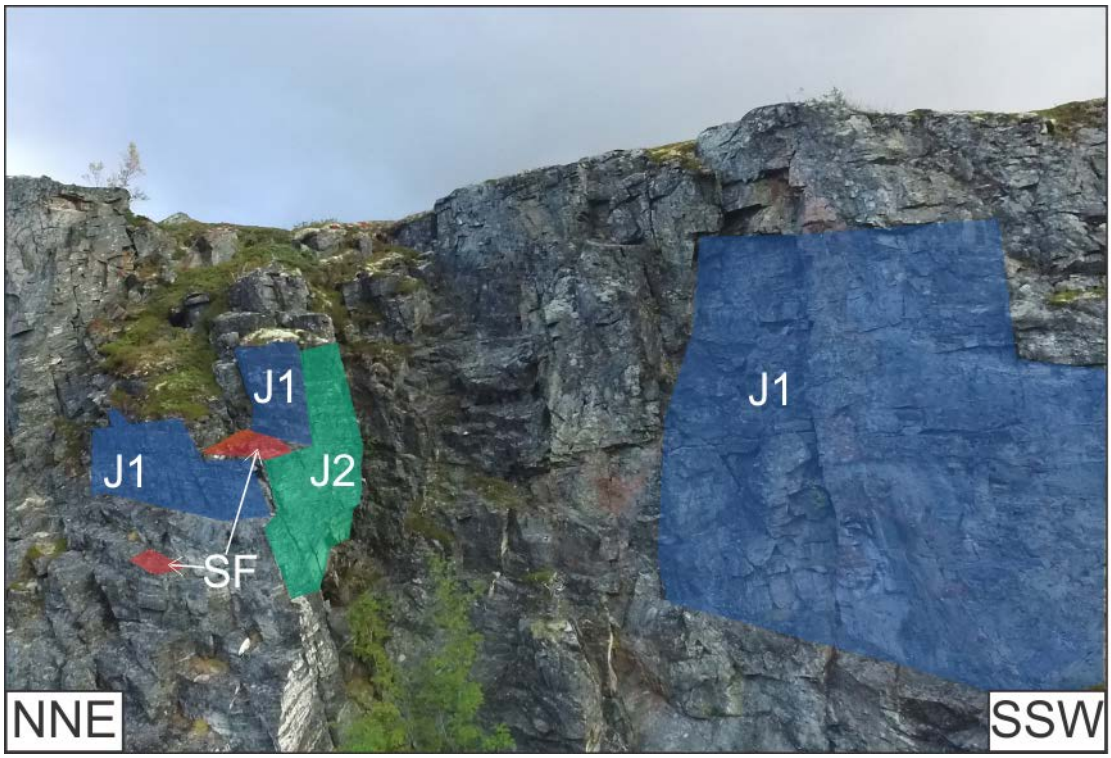

Figure 29: J1 as the most prominent joint set along the backscarp at Mellomfjellet 2.

3.2.2.5 Joint set 3

Joint set 3 was also mapped at both of the structural domains, with some variability in the dip angle. At Mellomfjellet 1 it was observed where a large EW-striking lineament intersected with the backscarp. For this structural domain, the set is moderate to steeply dipping (67˚) towards SSE (Figure 28B). The set is also present at Mellomfjellet 2, along a second EW-striking lineament, with a strike similar to the set at Mellomfjellet 1. The dip is shallower, with an average dip of 47˚ (Figure 30).

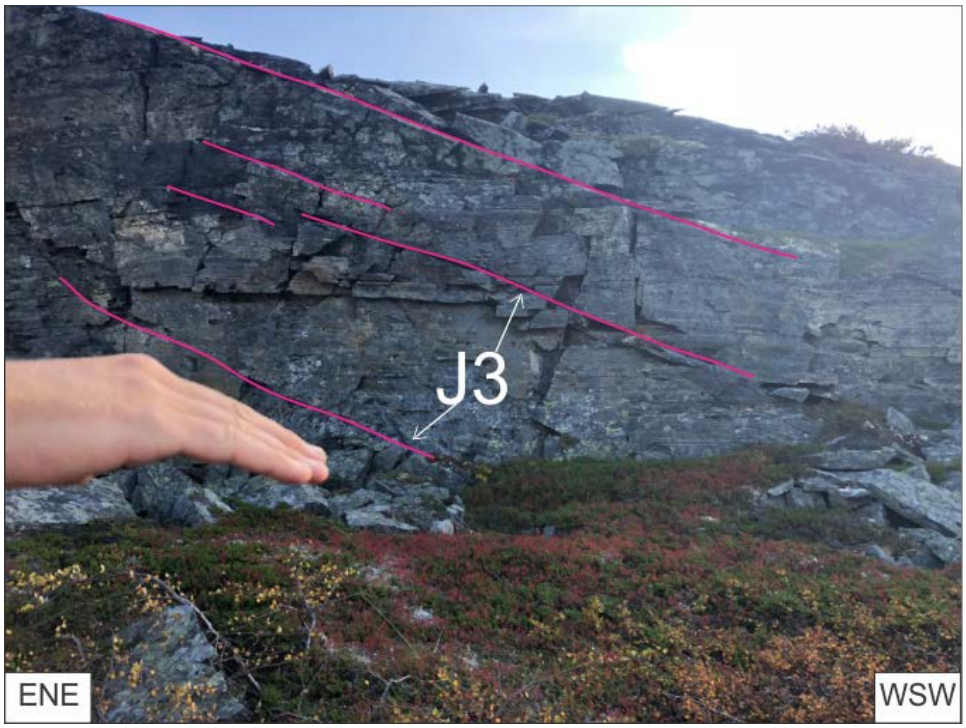

Figure 30: Joint set 3 exposed at an outcrop at Mellomfjellet 2.

3.2.2.6 Felsic intrusion

Inside the unstable area of Mellomfjellet 1, a felsic intrusion (as mentioned in 3.2.1) is present at the lower front of a large dislocated block (Figure 31). It is parallel with the foliation of the adjacent rockmass, has an average thickness of 40 cm and dips 20-30˚ downslope. The intrusion has a yellow-brown colour, consists of multiple planar structures parallel with the foliation with a surrounding grain matrix, consisting of fine sand to gravel sized grains. Only small chips and grains of the matrix were possible to break off with a hammer, due to the high strength of the material. However a weaker lens of loose material was located in-between the surrounding matrix. Yellow coating was observed on the joint surfaces below. The persistence of the zone laterally across the slide area is unknown, but it could be traced around all the visible parts of the lowermost block. When observing the entire site from a distance downslope, similar yellow zones were observed across the entire site, both Mellomfjellet 1 and 2. Due to steep terrain and the danger of falling blocks, these areas were not visited more closely.

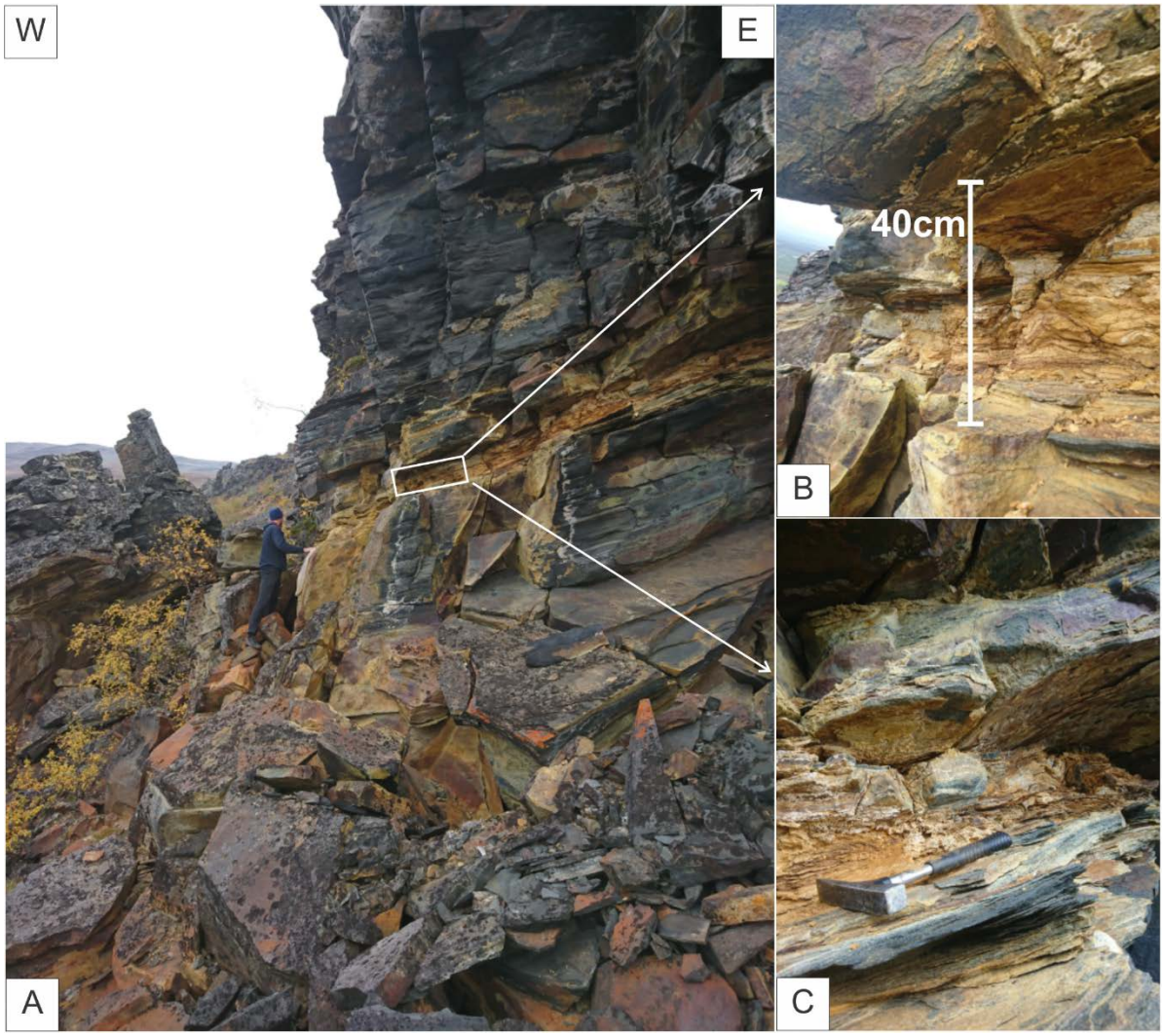

Figure 31: Foliation parallel felsic intrusion. A) Photo of the zone taken from the side of the block. B) Close-up photo of the zone taken from the side. C) Close-up photo of the shear zone taken from below

Samples from the zone were gathered from the lens of loose material. The structure of these fragments were investigated closer with a SEM microscope, where they were magnified up to 30µ. From the images a clay structure is apparent (Figure 32). Electron results showed a clear aluminosilicate signal, indicative of clay mineralogy, however no X-ray diffraction testing could be done to confirm this.

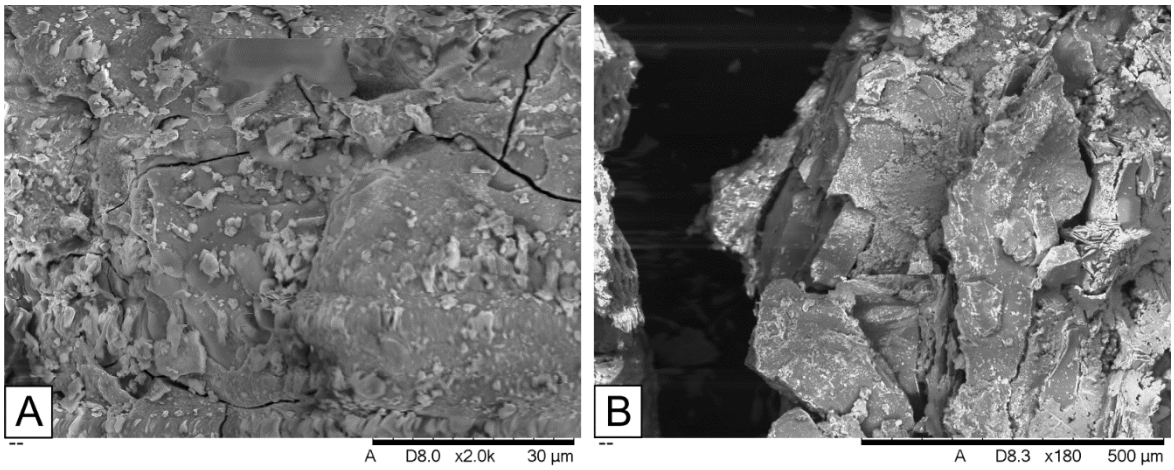

Figure 32: Close up of a grain gathered from the zone. A) Close-up of cracks, resembling a typical shrink-swell behaviour of aluminosilicate clay families. B) Multiple structures resembling clay are observed, which the grain is built of.

Structures resembling the shear zone material observed inside the unstable area of Mellomfjellet 1 were also observed outside of the unstable area, at three different locations. In Figure 33A, a 10 cm thick zone dipping ca. 30˚ downslope parallel with the foliation is visible. It had a dark brown colour, was not possible to chip with the hammer and consisted of a very fine grained matrix (fine sand to gravel) in between the foliation parallel planar structures. Figure 33B and C are from the same area, just upslope of the backscarp at Mellomfjellet 1. Figure B displays a 30 cm thick zone parallel with the foliation, consisting of coarse, partly loose gravel with a dark colour. The zone is partly covered by vegetation resembling some sort of moss, indicating the presence of water. Figure C shows a 10-15 cm thick zone of dense foliation resembling a schist-like texture, in contrast to the adjacent rock mass.

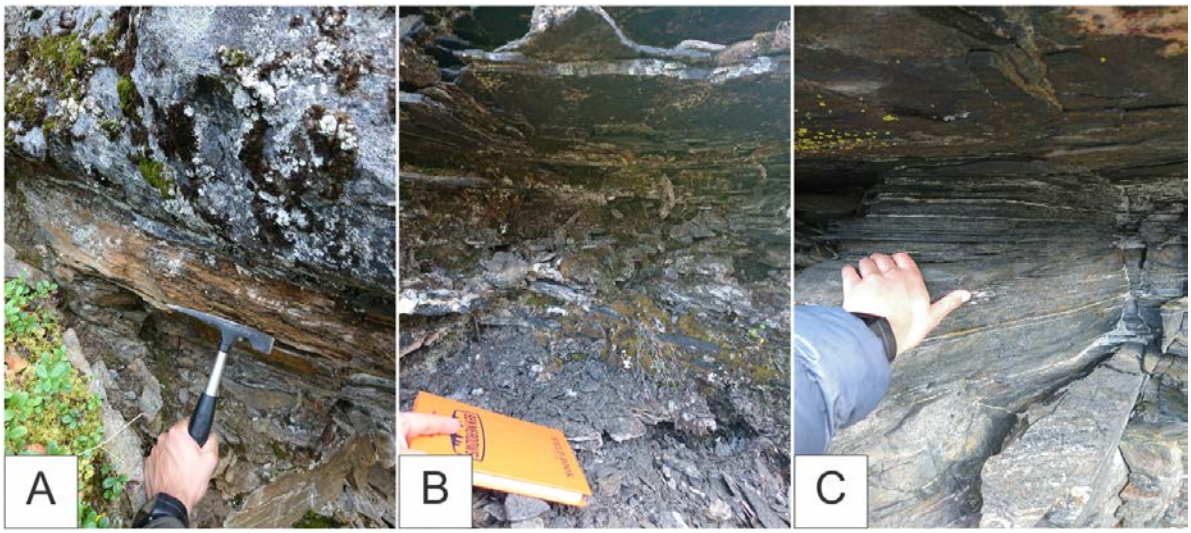

Figure 33: Geological features with similar characteristics as the felsic intrusion, displayed in Figure 31. A) 10 cm thick zone of hard material, resembling the texture of the felsic intrusion. B) A 30 cm thick zone with a more coarse and loose matrix, compared to the felsic intrusion. C) A 10-15 cm thick zone with a schist like texture, in contrast to the adjacent rockmass.

3.2.3 Geomorphological features

Geomorphological features related to URSs were mapped for the entire area, as described in chapter 2.1. Morphological lineaments, such as backscarps, subscarps and tension cracks were observed and mapped, together with morphological surfaces, such as dislocated blocks, talus cover and fresh rockfall. The observed features resulted in a geomorphological map over the site, which is illustrated in Figure 34. Photos and more detailed descriptions from the field are presented later on in this chapter.

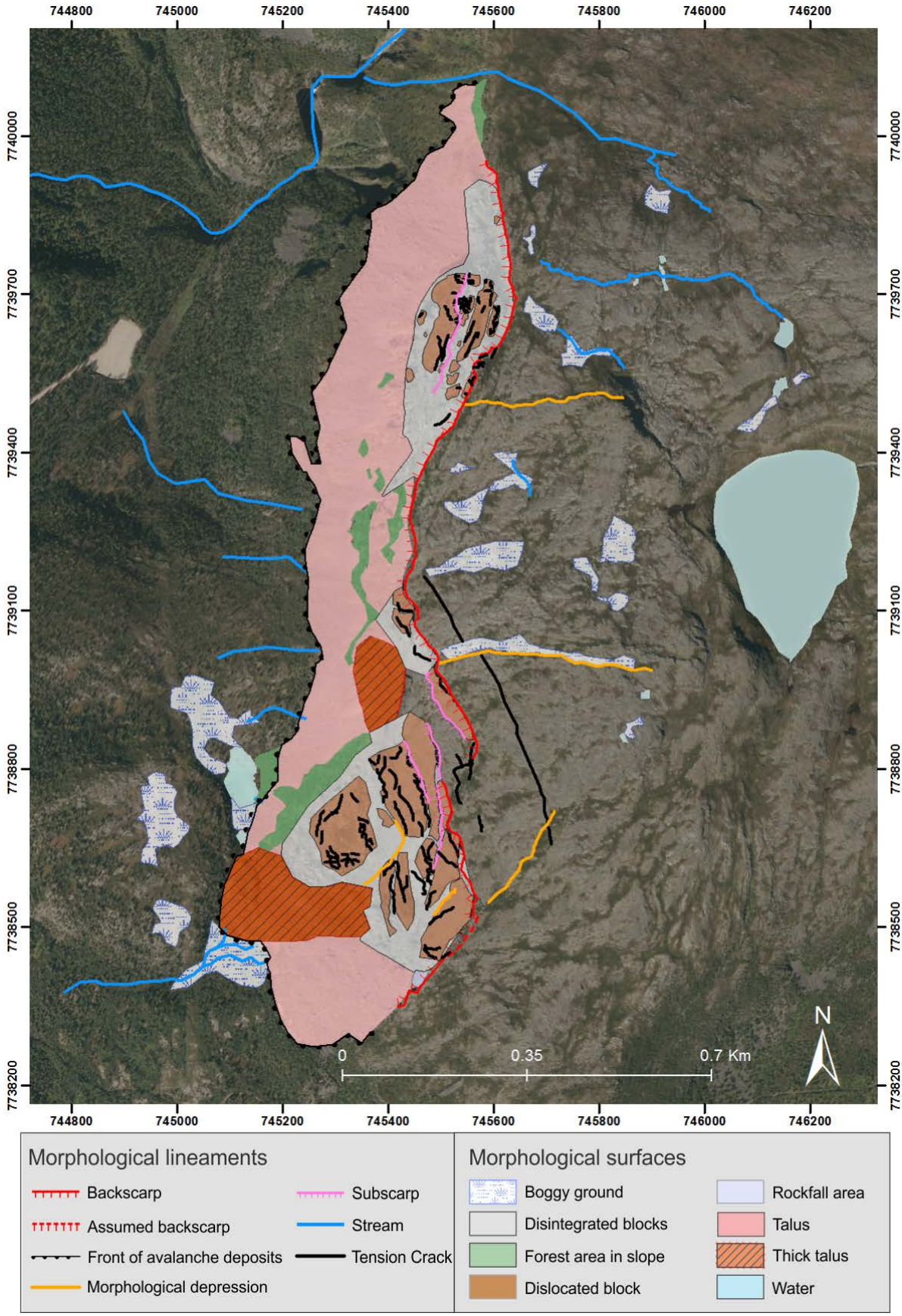

Figure 34: Overview map of mapped geomorphological features associated with an active URS.

3.2.3.1 Scarps

Both of the URSs have distinct backscarps creating a clear boundary for the unstable area. At Mellomfjellet 1, the backscarps are mainly oriented NNW-SSE, and a smaller part at the southern end is oriented towards the NE-SW. Even though the backscarps are well developed, with several meters opening and vertical offset, the backscarps are not fully connected as a single structure (Figure 35). The backscarps showed a varying degree of opening, but the main trend was that the horizontal displacement was larger than the vertical displacement (Figure 36). Subscarps divide the unstable area into multiple large blocks, resulting in varying deformation rates for the different blocks.

The backscarp at Mellomfjellet 2 is predominantly oriented in a NNE-SSW direction, with a slight direction change towards N-S in the northern end of the unstable area. The backscarp has a 25 m horizontal opening and a vertical displacement of 10 m, and is fully connected as a single backscarp (Figure 35). Subscarps are located in front of the backscarp, dividing the unstable area into several large blocks.

Figure 35: Photos of the backscarps, scarps, morphological depressions and tension crack taken from helicopter.

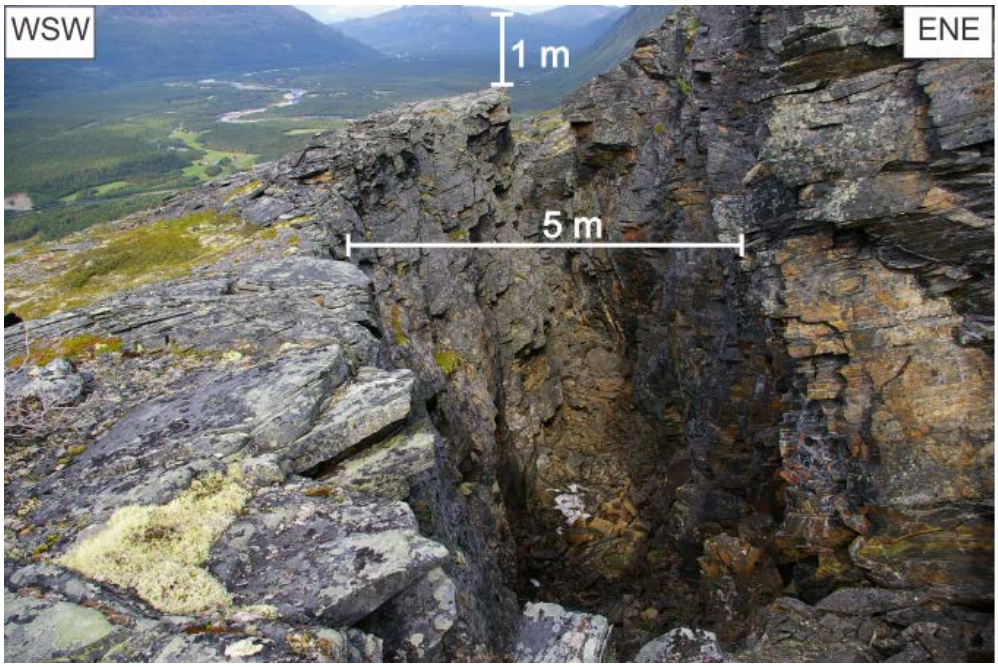

Figure 36: The vertical and horizontal displacement of a large block, in relation to one of the backscarp at Mellomfjellet 1. Modified after Henderson et al. (2010).

3.2.3.2 Tension crack

Above the backscarp at Mellomfjellet 1 (approx. 200 m eastward), a large tension crack is located (Figure 35 and Figure 37A-D). It is oriented in the same direction as the northern most backscarp (NNW-SSE), subparallel with J2, and can be traced along the mentioned backscarp (>500 m). The tension crack is more than 30 meters deep, has a horizontal opening up to 2 m and has large cavities filled with snow and ice.

3.2.3.3 Morphological depressions

Three large morphological depressions are present at the two domains (Figure 35), two at Mellomfjellet 1 and one just south of the main blocks at Mellomfjellet 2. Two of the morphological depressions strike in an E-W direction (Figure 37E), can be traced up 500 m, daylighting when intersecting the backscarps at their western end.

The third morphological depression is oriented NE-SW, striking parallel with the southern backscarp at Mellomfjellet 1. It can be traced from the intersection from the southern backscarp up to the tension crack upslope (Figure 34 and Figure 35). Tension cracks were found along the edges of the depression (Figure 38), where the smaller scale tension cracks change direction at the intersection point, and line up parallel with the large scale tension crack.

Figure 37: Photos of the tension crack (A-D) upslope of the backscarp at Mellomfjellet 1, and the northern most morphological depression (E) located at Mellomfjellet 2 (Figure 35). A) The joint pattern (J1 and J2) along the tension crack B) the depth of the tension crack where a person is observed at 25 m. C) The extent of the tension crack towards NW. D) The extent of the tension crack towards SE. E) The strike of the morphological depression at Mellomfjellet 2.

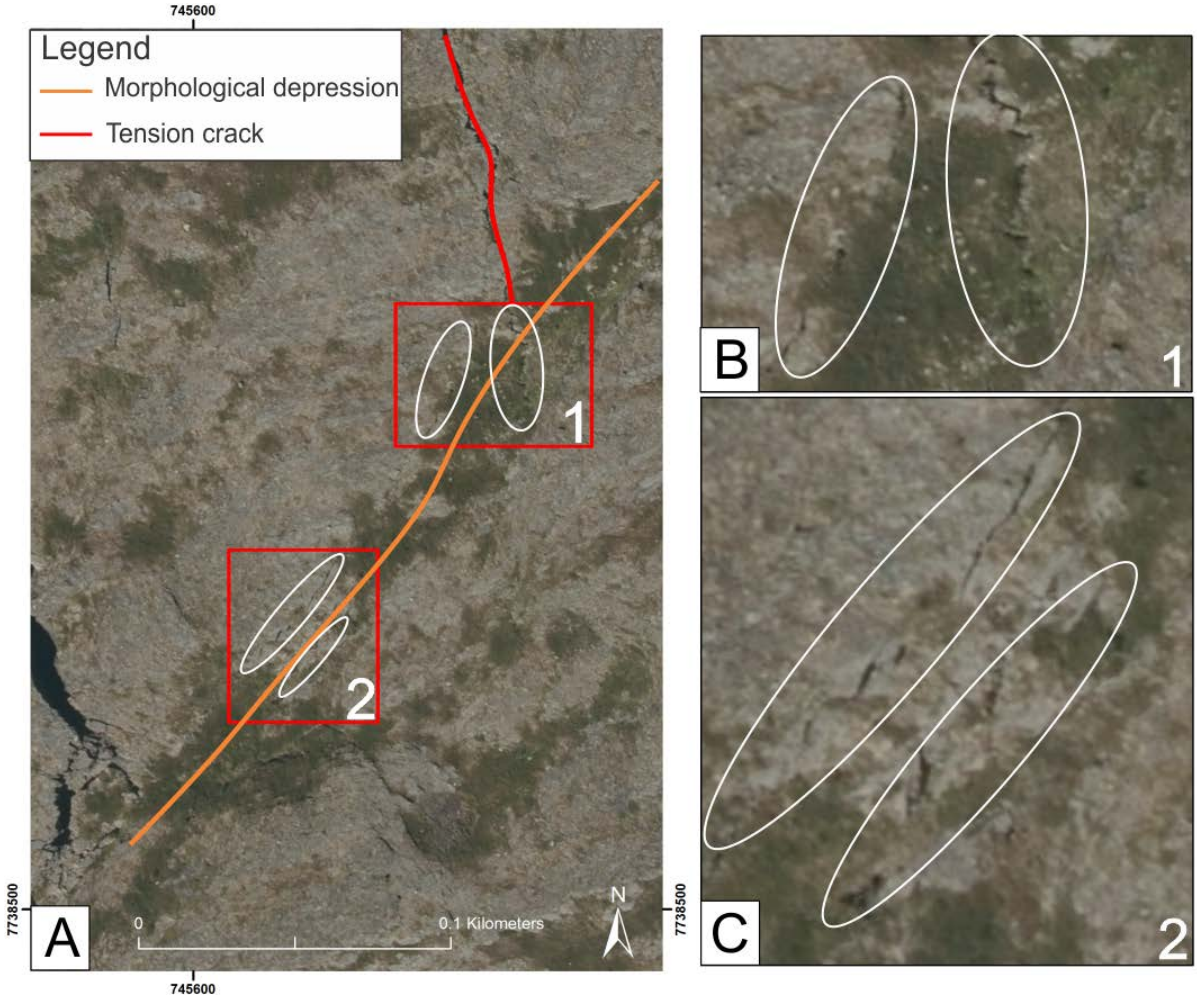

Figure 38: Tension crack and morphological depression at the southern part of Mellomfjellet 1, where the white ellipses show tension cracks. A) Overview map showing the large tension crack and morphological depression. B) Detail of the intersection between the large tension crack and morphological depression. Tension cracks along both sides of the morphological depression are visible, linking the large tension crack and depression together. C) Detail of tension cracks found on both sides of the morphological depression further downslope than the location in figure B.

3.2.3.4 Disintegrating blocks and talus

The displaced blocks are heavily fractured, resulting in a large amount of debris lying between and around the blocks (Figure 39). Downslope of the disintegrating blocks, talus cover of varying thickness is found, consisting of smaller boulders and blocks. In the south-western part of Mellomfjellet 1 (Figure 34), a large area of thick talus is located (Figure 40). Photos from the helicopter and aerial photos show bulging lobes towards the lower part of the talus, with multiple radial ridges at the front of the lobe (Figure 40A). There are signs of recent activity along the edges of the talus, with fresh material being exposed at the front of the lobe (Figure 40B). The vegetation immediately in front of the talus shows sign of disturbance, with trees being tilted over and fresh earth exposed (Figure 40C).

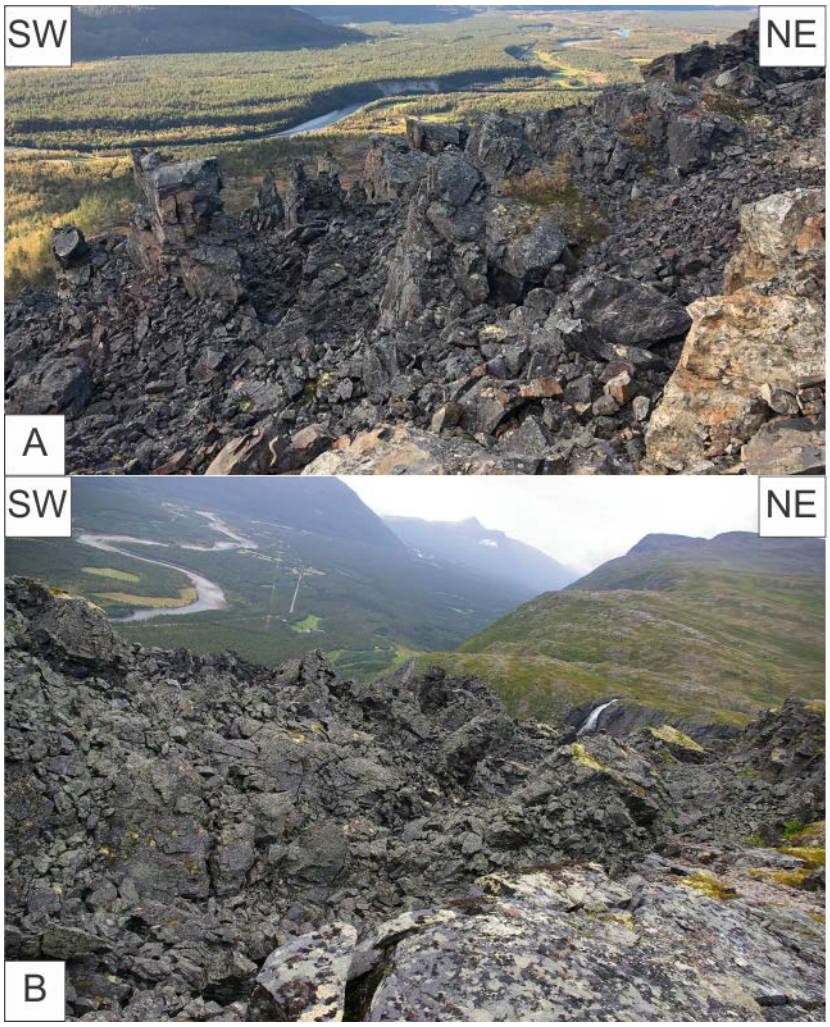

Figure 39: Disintegrating and blocky material A) Large blocks in the southern parts of Mellomfjellet 1. B) Blocks located just north of the main blocks at Mellomfjellet 2.

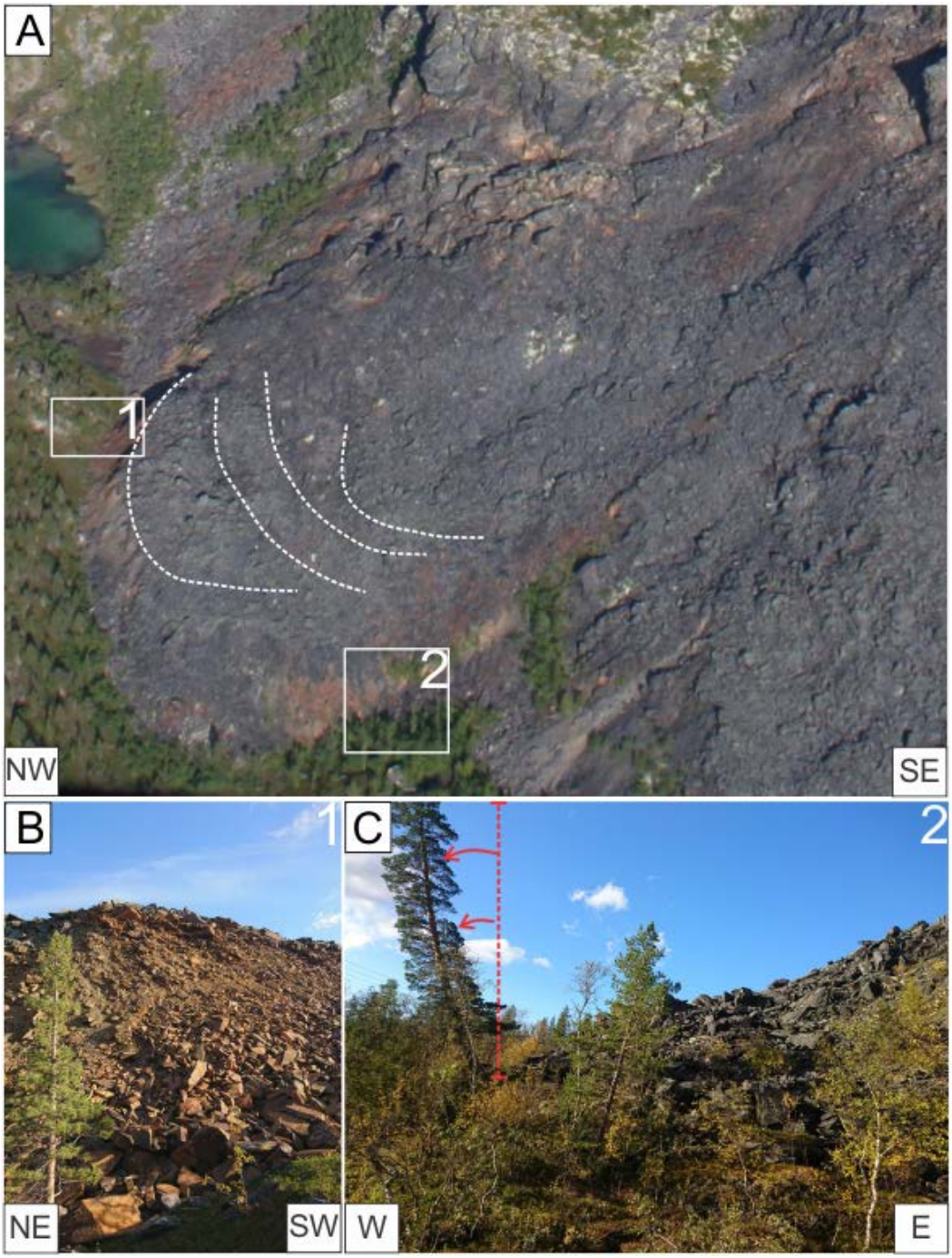

Figure 40: Photo of thick talus cover downslope of Mellomfjellet 1, where two details are marked. A) Overview photo from helicopter, where the dotted white lines show radial ridge structures at the surfaces of the lobe. B) Detail showing fresh scree material exposed along the edge of the talus. C) Detail showing tilting of a tree along the edge of the talus.

3.2.3.5 Observed failure modes

Examples of recent rockfall activity may give vital information when assessing a rock slope failure. Fresh rockfall activity indicates active deformation in the area, and can also reveal what kind of failure modes are most common along the discontinuities in the area. Observed failure modes are also important when validating the results from the kinematic analysis, when assessing failure modes on a larger scale. In Figure 41, recent planar sliding is demonstrated on a small scale, observed inside the unstable area of Mellomfjellet 1. At this location, failure had occurred along the foliation, exposing a failure surface of approx. 20-25 m^2.

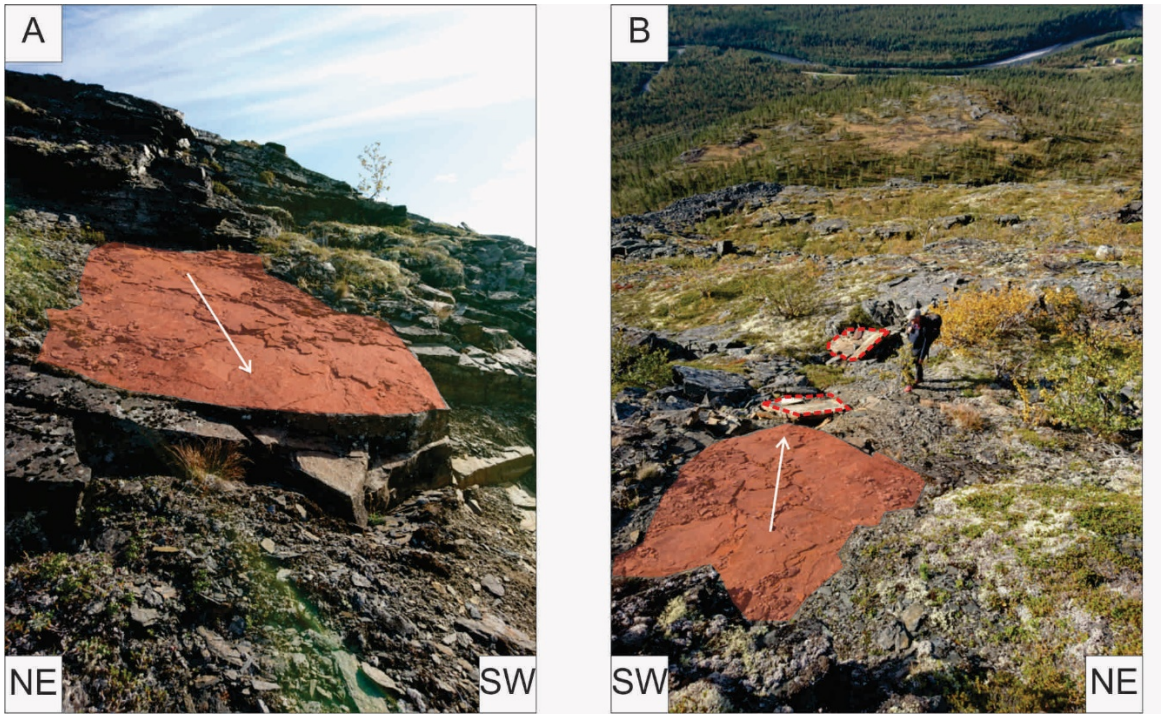

Figure 41: Planar sliding along the foliation plane. A) Picture taken from underneath the failure. B) Picture taken from above the failure, where the white arrows indicate sliding direction and the dotted red polygons show parts of the resultant rockfall deposits below.

Recent activity was also observed along the backscarp. Toppling failure was observed at the backscarp for both structural domains, as illustrated in Figure 42. At Mellomfjellet 1 multiple blocks were observed as either fully toppled out or partly toppling out of the backscarp (Figure 42A), while at Mellomfjellet 2 a large block was observed partly toppling out from the backscarp (Figure 42B). Failure occurred along J1 and SF for both locations, with J1 dipping steeply into the slope, and the foliation working as a basal failure surface with a gentle dip downslope.

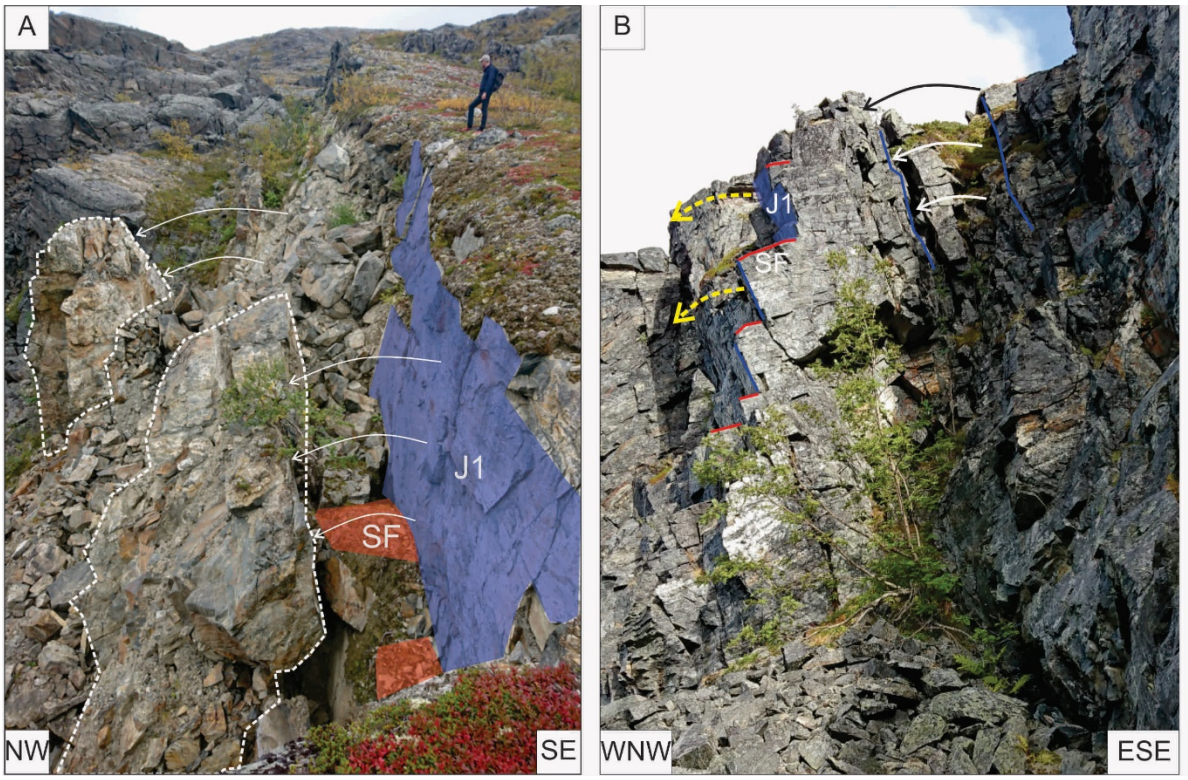

Figure 42: Toppling failure observed at a small scale along the backscarps. A) Recent toppling failure along the backscarp at Mellomfjellet 1, failing along J1 and the foliation. The dashed polygons shows the toppled out blocks, the arrows indicate toppling movement. B) Toppling occurring along the backscarp of Mellomfjellet 2, failing along J1 and the foliation. The dashed arrows indicate movement of previous toppled out blocks, the solid arrows show the observed movement of the block partly toppled out.

Fresh rockfall activity was also observed along the northern part of the backscarp of Mellomfjellet 2. The area was discovered due to the colour difference of the failure surfaces, which were brighter than the surrounding backscarp. The failure mode has the same characteristics as a biplanar sliding along the foliation, with wedge intersecting along J1 and J2 function as release surfaces. The failure must have occurred in the last 9 years, as it had not happened during NGU's field campaign in 2009 (Figure 43). This is the same area that was investigated using drone photogrammetry, in chapter 3.1.3.

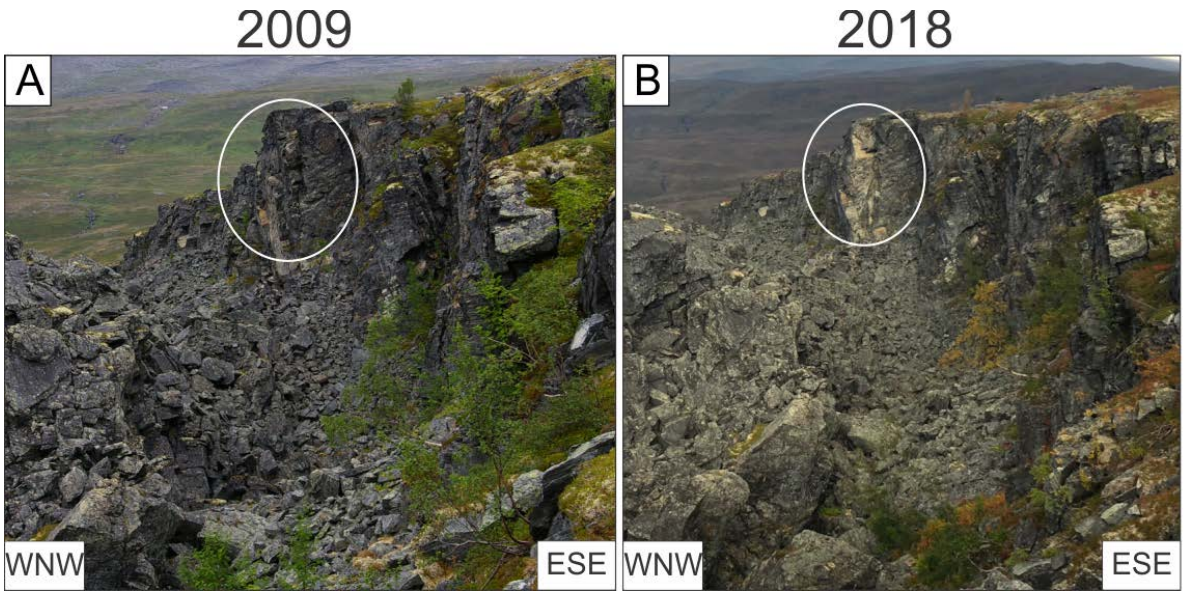

Figure 43: Bi planar failure that occurred the in the period 2009-2018. The backscarp and recent failure was examined more in detail using drone photogrammetry (3.1.3). A) Photo from 2009 where no recent activity were observed. The photo is modified after Henderson et al. (2010). B) Photo from 2018 showing the fresh failure occurring the last 9 years.

3.2.3.6 Seepage and boggy ground

There were no observations of streams flowing directly into the unstable area. However, multiple areas of boggy ground/wet marks, smaller streams, ponds and a lake were mapped upslope of the URSs. Snow and ice were also found deep inside the large tension crack upslope of Mellomfjellet 1. Multiple vegetated areas were mapped inside the unstable area. Densely forested areas were observed at the toe of the unstable area, within the talus, indicating the presence of water. Small and medium sized streams were mapped flowing out of the talus at multiple locations, often downslope of the forested areas located inside the unstable area (Figure 34). Mineral coating was observed on rocks inside the streams downslope of the unstable area.

3.3 InSAR

InSAR data from two different satellites (RADARSAT-2 and Sentinel-1) were made available by NGU for the area. They are presented as maps showing LOS displacement in mm per year (Figure 44 and Figure 45). The displacement rates are examined in relation to morphological elements (scarps and dislocated blocks) to get a better understanding of how the unstable area moves, and where the highest displacement rates take place. For both satellites sets, the data from the descending satellites are chosen, due to its favourable LOS in relation to the slope (Figure 12). It is worth mentioning that all velocities are recorded within the LOS of the satellite, which is only one component of the movement vector. Therefore, the movement rates could be greater than presented in this chapter.

3.3.1 RADARSAT-2

Displacement rates from descending RADARSAT-2 (R-SAT) measurements are presented in Figure 44, where red coloured areas show negative (downward along LOS) displacement and blue coloured areas show positive (upward along LOS) displacement. Six profiles extracting displacement rates are drawn across the unstable rock slope to visualize the displacement variations in relation to the morphological elements. Profiles AA', BB' and CC' show displacement at Mellomfjellet 1, and profiles DD', EE' and FF' show displacement at Mellomfjellet 2. It is worth noting that the assumed stable areas all show positive displacement rates of 1-1.5 mm/year, most likely due to processing errors. It is therefore assumed that 1 mm/year shows 0 mm/year displacement, and that the displacement rates lower than 1 mm/year are moving downward along LOS.

Mellomfjellet 1 shows the highest displacement rates, with a max LOS displacement of -5.8 mm/year, along profile AA'. Profile AA' is drawn perpendicular to the backscarp and parallel with the slope, showing a change in vertical displacement going from 0.5 mm/year above the backscarp, to -5.8 mm/year inside the unstable masses. Profile BB' is drawn across assumed stable area, and shows no sign of displacement. Profile CC' are drawn in the same orientation as profile AA', presenting increased downward displacement from the backscarp and into the blocks and talus downslope.

Mellomfjellet 2 shows lower displacement rates, with maximum downward movement of -0.5 mm/year. The relative velocity difference between the stable and unstable areas are 1-1.5 mm/year downwards for both of the profiles going into the unstable area (profile DD' and FF'), displaying a change in displacement at the backscarp.

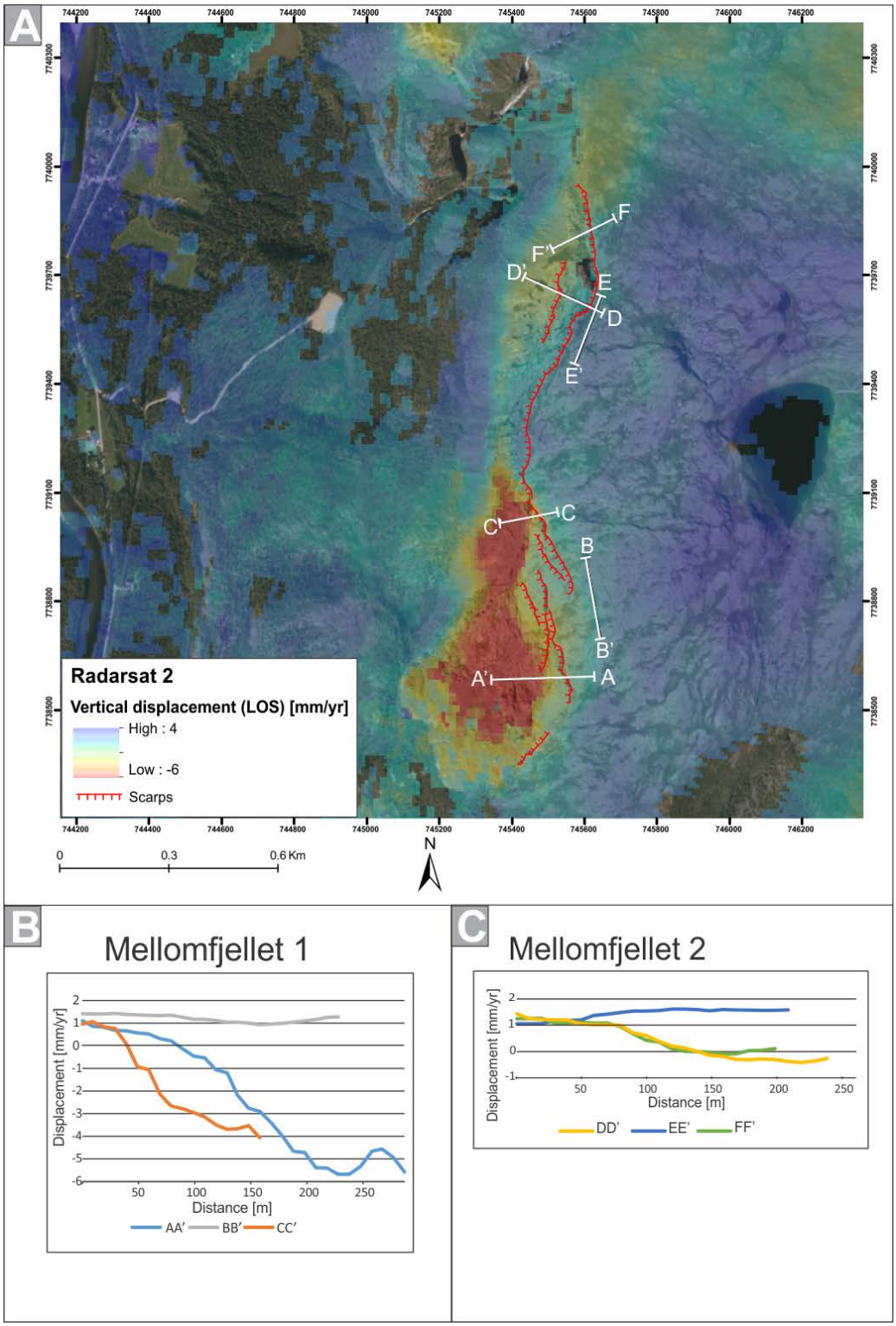

Figure 44: Map and profiles showing measured displacement based on R-SAT descending data at Mellomfjellet. A) Overview map of displacement and the location of the profiles. B) Displacement along profiles at Mellomfjellet 1, where a change in displacement across the backscarp is visible in both profile AA' and CC'. Along profile AA', a relative decrease in displacement is recorded at approx. 240-270 m where a smaller block is located. C) Displacement along profiles at Mellomfjellet 2. Profile DD' and FF' show a change in displacement across the backscarp, with a change of 1.5-2.0 mm downward. Profile EE' shows that stable areas are given a positive value of 1-1.5mm/year, the same as profile BB' at Mellomfjellet 1.

3.3.2 Sentinel-1

Displacement rates from descending Sentinel-1 are presented in Figure 45 as point data. When assessing change in velocity for point data, polygons are drawn for areas that show similar displacement rates (low variation), as these give a more area-wide result. Red coloured points show negative (downward) vertical displacement, while blue coloured points show vertical positive (upward) displacement.

The maximum velocities displayed at Mellomfjellet 1 are found in areas of active talus and medium to small dislocated blocks, rather than rockslide areas. These areas show displacement rates up to -40 to -50 mm/year (downslope). Polygons located on larger blocks at Mellomfjellet 1 show displacement rates ranging from 0.8 to -8.2 mm/year. Outside of the unstable area (upslope of the backscarp), the polygons show velocities ranging from 0.5 to 1.3 mm/year upwards.

Velocities at Mellomfjellet 2 are much lower than at Mellomfjellet 1, displaying rates up to a maximum -3.5 mm/year downslope on the main block. Right at the edge of the backscarp, there is not detected any change in displacement (0.3 mm/year, Figure 45C). The movement is located further out on the main block, in relation to a subscarp, with velocities of -3.5 and -2.9 mm/year are recorded (Figure 45C).

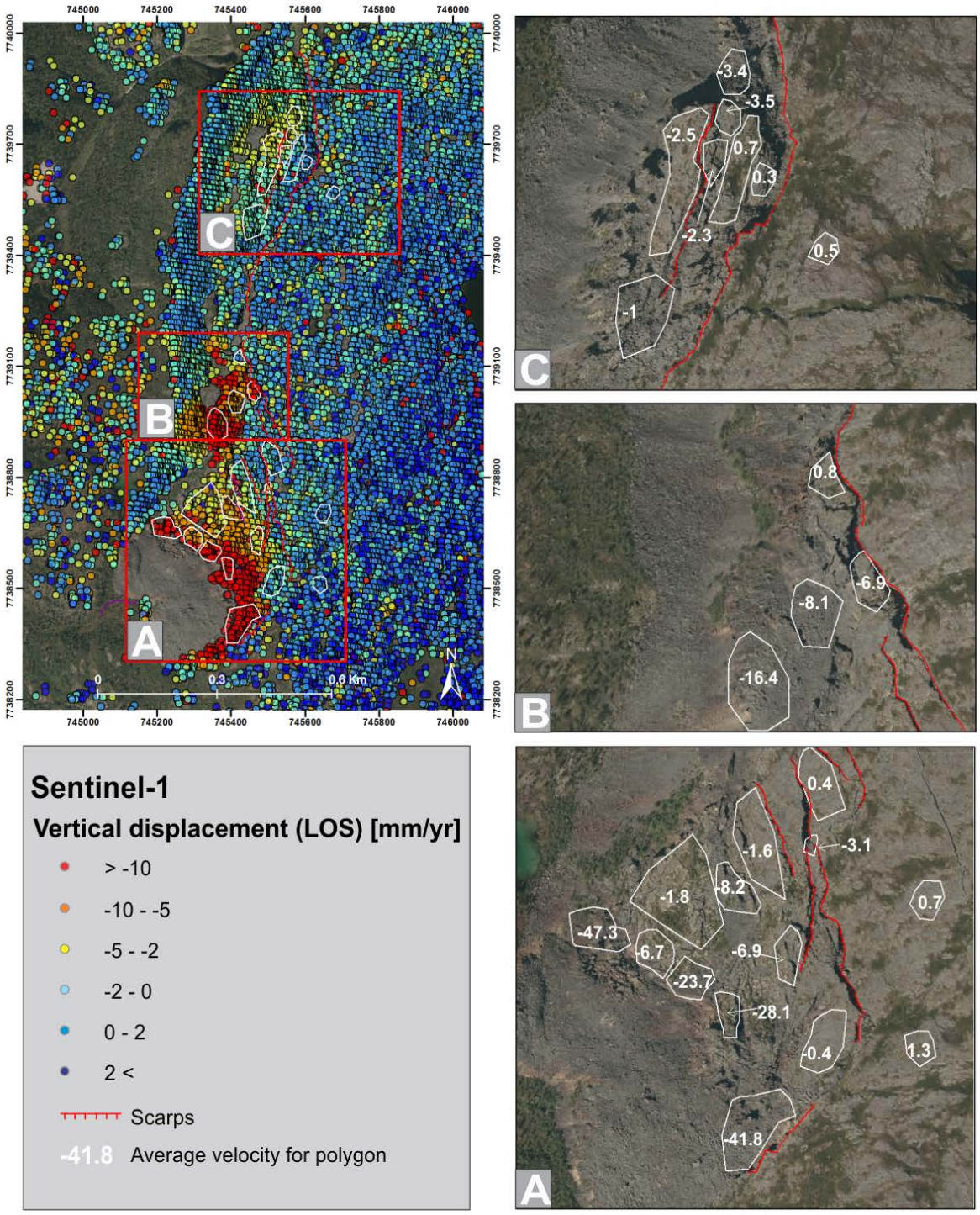

Figure 45: Overview of displacement measured from the Sentinel-1 satellite. The three insets to the right are details of the main polygon analysis areas. A) Shows the polygons of the southern "main" area of Mellomfjellet 1, where the largest displacements are from the disintegrated talus. B) Shows the polygons of the northern area of Mellomfjellet 1, where a smaller block shows -6.9 mm/year displacement, but the largest displacements are from the talus area. C) Shows the polygons for Mellomfjellet 2, where the maximum displacement are -3.5 mm/year, recorded on one of the main blocks.

3.4 Failure scenarios and run out analysis

Based on the structural domains and the orientation of the backscarps, Mellomfjellet 1 and 2 are separated into two failure scenarios. For both of the scenarios, the worst case scenario has been selected, in terms of the volume. The outline of the two scenarios are presented in Figure 46, together with the SLBL profile lines used to inspect the volume.

The volumes for the two failure scenarios were calculated based on the SLBL technique explained in chapter 2.6.1., and the results are presented in Table 10. Mellomfjellet 1 has an intermediate volume of $1.12x10^6$ m^3 resulting in an angle of reach of 25.4˚ from the Scheidegger equation (explained in chapter 2.7.1). Mellomfjellet 2 has an intermediate volume of $3.05x10^6$ m^3, resulting in an angle of reach of 22.1˚ from the Scheidegger equation. The angle of reach was used as input parameter when performing the run out analysis in Flow-R.

Table 10: Volume estimated, angle of reach and run-out length for the two domains.

Domain	Area [m^2]	Estimated volume [m^3]			Angle of reach [˚] (int. volume)	Run-out length [m] (int. volume)
		Min. SLBL	**Int. SLBL**	Max. SLBL		
Mellomfjellet 1	113260	$0.72x10^6$	**$1.12x10^6$**	$1.59x10^6$	25.4	695
Mellomfjellet 2	159002	$1.54x10^6$	**$3.05x10^6$**	$4.07x10^6$	22.1	985

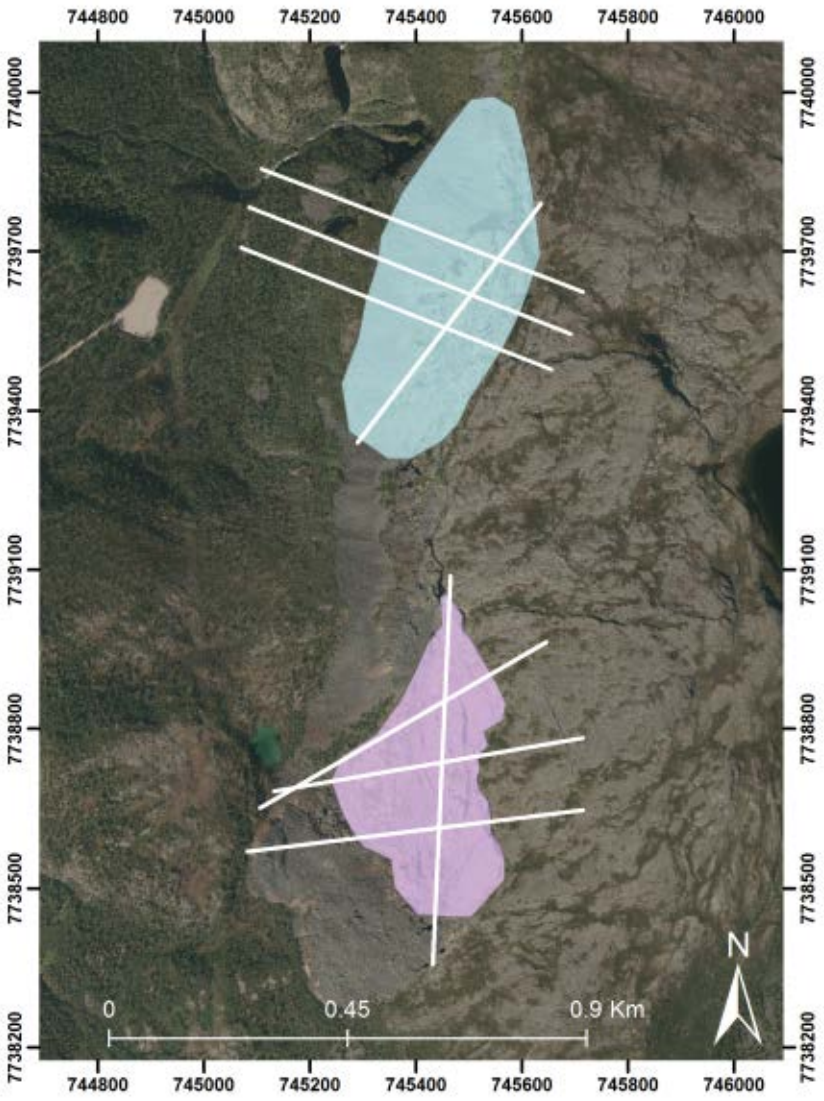

Figure 46: Overview map over failure scenarios and SLBL profiles lines used to inspect the unstable volume.

3.4.1 Mellomfjellet 1

To figure out if a potential failure of Mellomfjellet 1 could cause fatalities, a run-out analysis was conducted in Flow-R, as described in chapter 2.7.2. Based on the resulting volumes (Table 10), the maximum run-out distance was set to 695 m. The results from the run-out analysis are presented in Figure 47, where the susceptibility is divided into three classes: <0.01 (yellow), 0.01-0.1 (orange) and 0.1-1 (red). From the results, it is clear that a potential run-out will not reach any houses or roads.

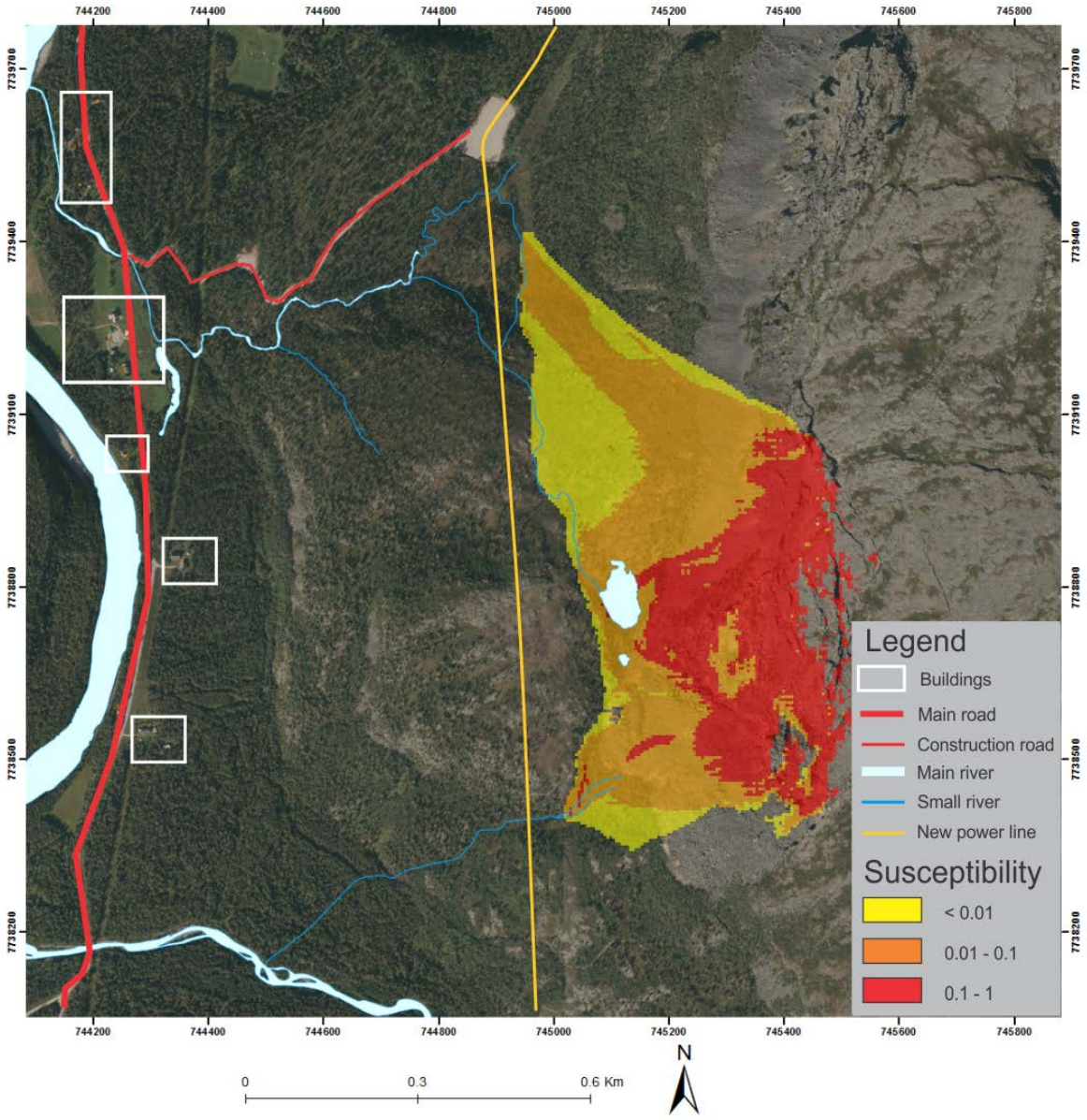

Figure 47: Overview map of the runout analysis for Mellomfjellet 1.

3.4.2 Mellomfjellet 2

A potential run-out distance of 985 m was calculated for Mellomfjellet 2, based on the estimated volume (Table 10). The results from the analysis (Figure 48) are divided into three classes based on the susceptibility, with the same intervals as Mellomfjellet 1. From the analysis, one can see that a potential run out will stop before reaching houses or any main roads. However, a potential run out may reach a construction road and a construction site (light area at the NE end of the construction road), from the establishment of a new power line (Figure 48). Construction work is assumed to be completed in 2020/2021 (Statnett, 2018). It is also worth noting that a potential

run-out has a chance of crossing a river, which is upstream of the multiple settlements in the area (Figure 48).

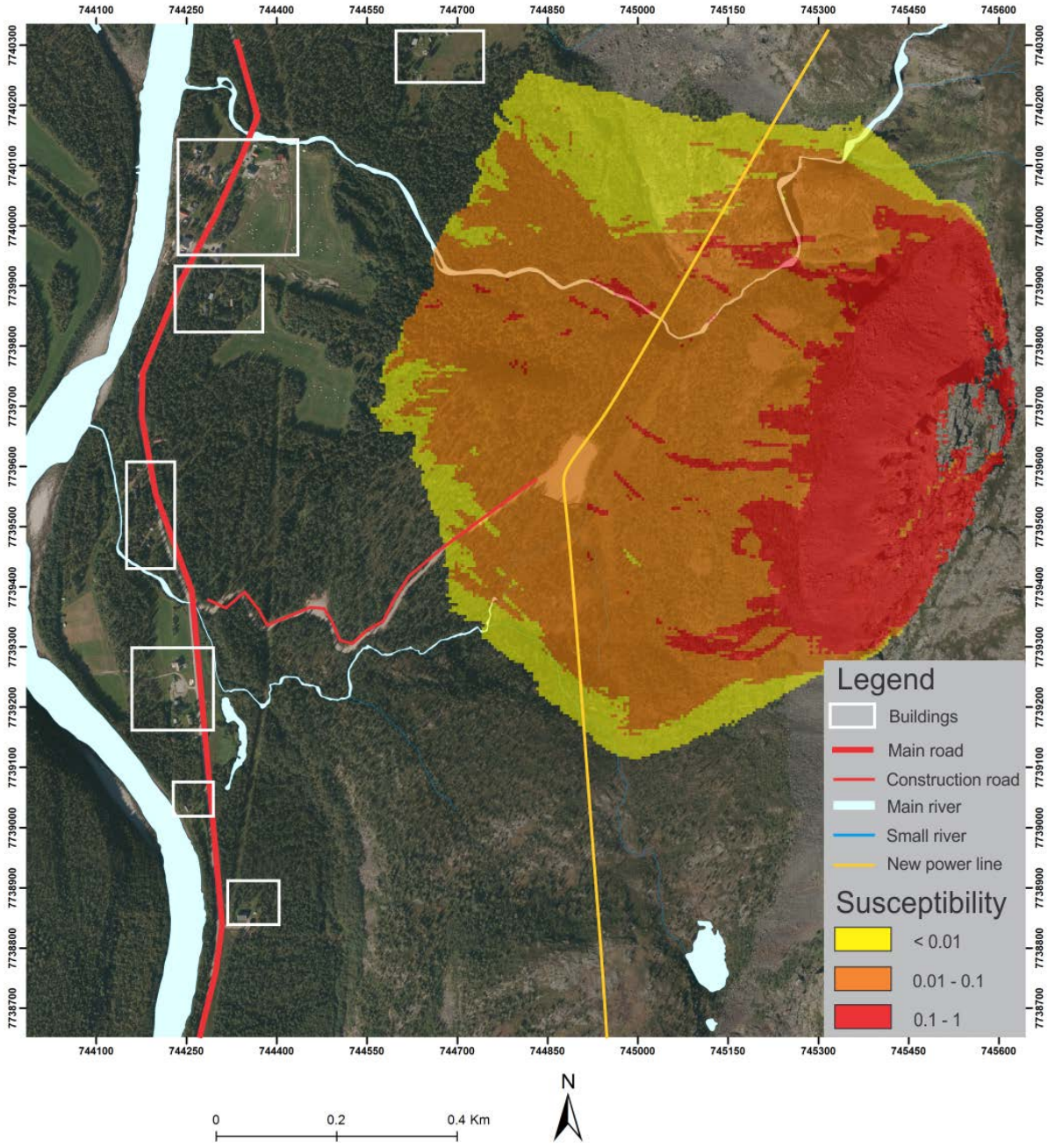

Figure 48: Overview map of the results from the runout analysis for Mellomfjellet 2.

3.5 Hazard assessment

The following criteria were assumed to calculate the hazard score for the URSs.

Mellomfjellet 1 is an URS with party developed backscarps, connected to each other by tension cracks and depressions. The lateral flanks are fully developed. The foliation is daylighting in the slope, allowing for sliding. It is folded, but the fold axis daylight in the slope, also acting as a potential sliding structure. Due to talus and scree deposits is not possible to determine the lower limits of the URS. InSAR LOS displacement rates show an average annual displacement below 0.5 cm. Fresh surfaces from recent rock fall activity were mapped over the entire area.

Mellomfjellet 2 is an URS with a fully developed backscarp over the entire slope, with fully developed lateral limits on both sides. The foliation daylights in the slope and may act as a potential sliding structure. The foliation is gently folded, and the fold axis daylights the slope as well, and may act as a sliding structure. Toppling failure is possible along J1, a very persistent structure. The lower limits of the URS are not possible to detect, due to talus deposits. InSAR LOS displacements shows displacement rates lower than 0.5 cm/year. Fresh surfaces from recent rock fall activity were mapped at multiple locations.

The results from the hazard assessment are presented in Table 11. Mellomfjellet 1 was assigned with a mean hazard score of 5.3, while Mellomfjellet 2 ended up with a mean hazard score of 5.6., where both scores results in a *Medium* Hazard class. Detailed reports from the hazard assessment are available in Appendix H.

Table 11: The hazard score and class for the different scenarios, from the hazard assessment.

Scenario	Hazard score			Hazard class
	Minimum	Mean	Maximum	
Mellomfjellet 1	5	5.3	6	Medium
Mellomfjellet 2	5.5	5.6	6	Medium

4 Discussion

This discussion chapter brings together key results from this study to present a conceptual overview model of the Mellomfjellet URSs. By addressing the key questions presented in chapter 1.2, the overall research objectives are achieved.

4.1 Validation of the structural analysis

The orientation of the outcrop slopes from which structural measurements were collected shows clear strike trends in three directions. Mapping along preferred slope orientations leads to data bias whereby structures sub-parallel to the outcrop orientation may be difficult to detect, or their true orientation may be obscured (Terzaghi, 1965). It is possible to use a weighted factor to reduce the bias (Park and West, 2002), but this has not been done. Therefore, bias due to mapping along preferred outcrop slope orientations may have led to errors in the structural data and therefore the structural analysis.

Spatial variation within the rockmass can also affect the structural data. The fabric of the rockmass varies due varying degree of foliation. For example, areas with poorly developed foliation may be difficult to measure in the field due to sparse occurrences of daylighting planes, and their low persistence. Variance within the data may also be a caused due to the folding of the foliation. This is especially true at Mellomfjellet where the folding is gentle, with a wavelength of 5-15 m. The measured orientation and dip of the foliation plane will depend on the part of the fold that is measured (e.g. which limb). This could explain why there is a greater sample of structural measurements from the north-dipping limb of the foliation at Mellomfjellet 2, as opposed to at Mellomfjellet 1 where the density of structural measurements taken from each limb is evenly distributed (see stereoplots, Figure 18 and Figure 19) However there are seven more structural stations at Mellomfjellet 1 than at Mellomfjellet 2, which gives a better representation of the variating foliation. At Mellomfjellet 1, there is also a larger variation in outcrop slope orientation than Mellomfjellet 2 (rosette plots in Figure 17), resulting in smaller orientation bias, and one explanation for the differences in foliation limb measurements could therefore be that the lack of outcrops at Mellomfjellet 2 has led to a lack of exposure of all the foliation structures present at Mellomfjellet 1.

The axes of the folds were measured in the field, and can be validated in Dips by calculating the axis from fold limb orientations displayed on the stereoplot. The measured and calculated fold axes at Mellomfjellet 1 only differed by 11˚ in trend. At Mellomfjellet 2 however the measured and calculated fold axes showed a larger variation, differing 34˚ in trend. The large

difference at Mellomfjellet 2 is likely explained by the fact that only one fold axis was observed and measured in field, resulting in a lack of data. The calculated fold axis is based on all the foliation measurements, and is therefore assumed to be more reliable. It is worth noting that the calculated fold axis could also be influenced by the factors influencing the foliation data. The calculated fold axis from the Mellomfjellet 2 domain differs 13˚ in trend from that calculated at the Mellomfjellet 1 domain. When combining domains to calculate fold axis trend the results show it differs 2˚ from the calculated axis at Mellomfjellet 1, and 11˚ for the axis at Mellomfjellet 2. The low difference in trend validates the data of downslope trending fold axis.

Some differences between mean joint set orientations can be observed between the two domains (Figure 18 and Figure 19). These difference may be real differences in the structural orientations but could also be explained by the different number of structural stations within the two domains (Figure 17). A larger number of measurements were taken over a larger area at Mellomfjellet 1 than 2. A larger sample size and sample coverage area, combined with data bias caused by outcrop orientation may have had an unquantifiable effect on the structural data and analysis.

J3 has the exact same strike in both domains, but shows a 20˚ difference in dip angle (67˚ at Mellomfjellet 1 and 47˚ at Mellomfjellet 2). Both sets show lower densities than J1 and J2, and were assigned as a set due to being well documented in field. J3 was only observed close to the E-W striking morphological depressions, for both domains. Their low contour density may therefore be affected by the lack of outcrops oriented in a favourable direction, as previously mentioned. However, a strike of 075 is almost perpendicular to the slopes strike (170 for Mellomfjellet 1 and 200 for Mellomfjellet 2), which is a preferable angle to detect the joint set (Park and West, 2002). Another explanation may therefore be that the joint set only exists nearby the E-W striking morphological depression. In Figure 28B, where the morphological depression is daylighting in the backscarp at Mellomfjellet 1, J3 is well documented. At Mellomfjellet 2, the area where the morphological depression and backscarp are intersecting was not reachable, and therefore not inspected. Nevertheless, it is a possibility that J3 is only found nearby the E-W morphological depression as a response to tectonic activity (e.g. faulting), and that J3 are fault parallel joints and fractures located in the damage zone of the faults.

4.1.1 Comparing data from photogrammetry with field data

Drone photogrammetry was used in order to gather structural data from inaccessible areas in field. In this section, similarities and differences from field measurements and photogrammetry will be discussed to get a better understanding of the uncertainties in the results and to validate the results presented.

Both the foliation and J1 shows almost identical trends in strike and dip, with a strike difference of -017 and -16, and dip difference of +11 and +09 respectively (Figure 22 and Table 2). If all the discontinuity sets showed the same difference, it would be likely that the entire 3D model was slightly disoriented compared to the real outcrop, leading to an error in the structural analysis. However, J2 (001/-08) did not differ in the same direction as SF and J1, indicating other reasons for the differences. The GCPs introduce the biggest uncertainty to the data, as they were measured using low precision (2 m) of the GPS. There is a possibility that inaccurate positioning led to warping of the points during georeferencing, therefore affecting the structural results in Coltop3D. Nevertheless, the differences were within the variance of the sets mapped in field (Figure 22), indicating an accurate result. The shape of the discontinuity sets (Table 9) also needs to be taken into account when validating the structural analysis. The foliation had an undulating shape, resulting in a varying dip angle depending on where it is measured (Oppikofer et al., 2011). Due to the small surface size (Figure 20 and Figure 21), measurements are prone to a varying in dip angle due to an undulating shape. When gathering data from small surfaces, there are also uncertainties regarding the point density of the model (point cloud). A point density of 0.277 points/cm^2 (Appendix E), equates to approximately 1 point per 2x2cm. Therefore smaller surfaces may not being fully captured in the point cloud, and result in structures being averaged out. The foliation and J1 surfaces are typically connected in a step-like manner. This formation is not easily detected in the point cloud, and may be interpreted as a single plane when analysing the point cloud in Coltop3D (Oppikofer et al., 2011). As a result, the mean plane of the structural set dips steeper than the real planes (Figure 49). It is also important to keep in mind that the area measured with photogrammetry was only a 40x10 m large area of Mellomfjellet 2, and the results from Coltop3D therefore cover a smaller sample area than the field measurement campaign. The difference in spatial extent will likely result in differences in the results.

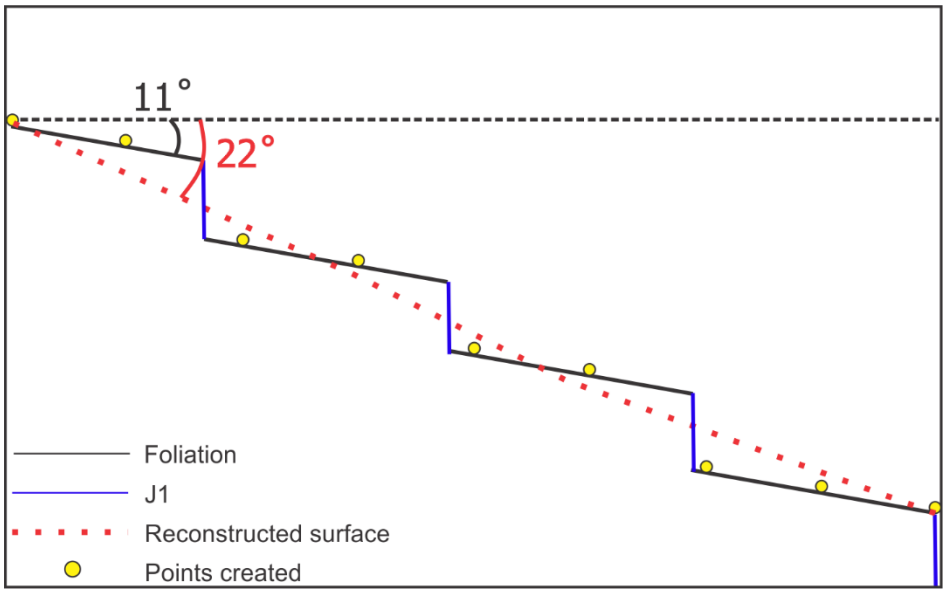

Figure 49: A simplified sketch showing how the point density may lead to a steeper dip when reconstructing small, stepped foliation surfaces in a point cloud.

4.2 Morphological features in relation to discontinuities

To understand what kind of influence the inherited bedrock structures have on the failure mechanisms, it is necessary to relate the large scale morphological features associated with an URS, to the mapped discontinuities and lineaments.

4.2.1 Scarps

At Mellomfjellet 1, the backscarp is mainly striking NNW-SSE (subparallel to J2, Figure 28A), with a smaller part striking NE-SW (parallel to J1, Figure 42A) in the southern end. At Mellomfjellet 2, the NNE-SSW-striking backscarp aligns with J1 (Figure 29), with some small steps to the NNW-SSE, subparallel with J2. The fact that the subscarps in both domains repeat these same strikes (as the backscarps and joint sets, Figure 35), supports the idea that the unstable area is disaggregating along pre-existing joints in the bedrock, rather than forming new surfaces at the time of rupture.

Trace lineaments are often assumed to be surface expressions of faults (Brideau et al., 2009). Everard (1994) and Savigny and Clague (1992) found that landslides, in many cases, were found nearby trace lineaments. The lineament analysis at Mellomfjellet 1 (Figure 17) shows two dominant trend directions: NE-SW and NW-SE, coinciding well with the backscarp orientations. At Mellomfjellet 2, the lineaments were oriented in a NNE-SSW direction, parallel with the backscarp and subscarps. These orientations coincides well with the post-Caledonian

faults (1.4.3.2), mapped by Indrevær et al. (2013), plotted in Figure 50B. These observations support the idea that inherited bedrock structures have a large influence on the unstable area, as they are oriented subparallel to parallel with the joints found in field (Figure 50A), which are believed to control the development of the unstable area.

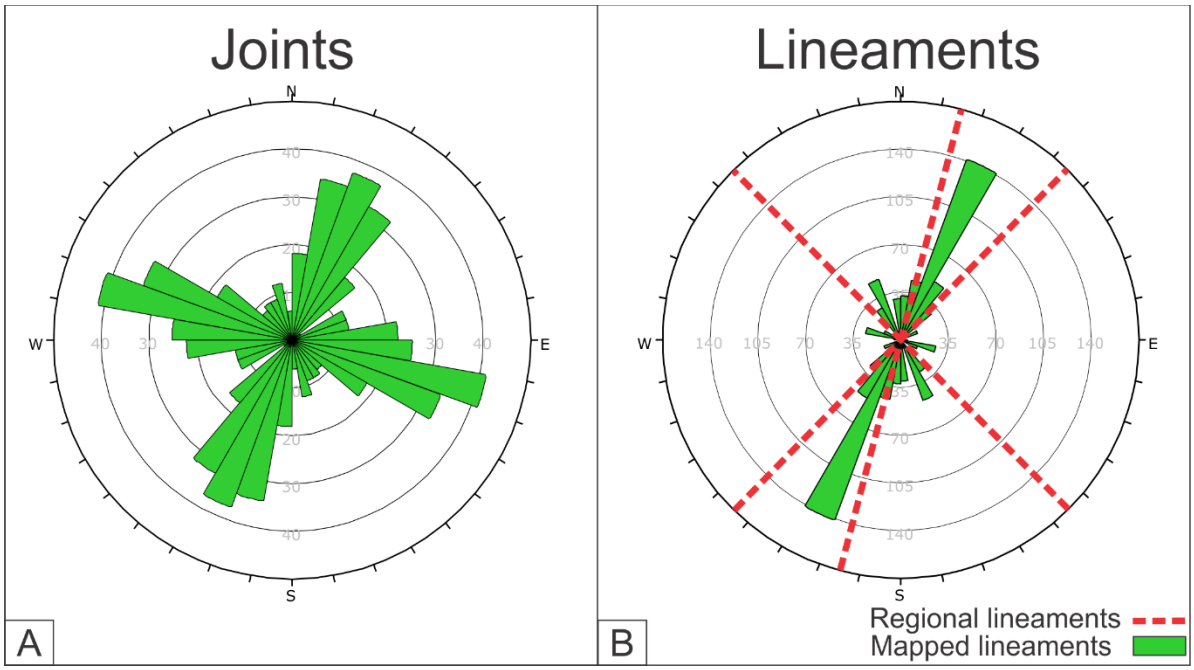

Figure 50: Rosette plots comparing the direction of the joints measured in field with the lineaments mapped from aerial photos and the regional lineaments in Troms. They show similar trend directions, however the mapped lineaments show NNE-SSW as the most dominant strike direction, while the joints are more evenly distributed between NNE-SSW and WNW-ESE as strike direction. A) Rosette plot of joints measured in field. B) Rosette plot of measured lineaments and regional lineament trends.

4.2.2 Tension crack in relation to development of backscarp

A large backscarp-parallel crack striking NW-SE above the unstable area of Mellomfjellet 1 (Figure 34, Figure 35 and Figure 37) is considered to be a tension crack as it is mapped on stable ground (as interpreted by InSAR, and due to the lack of observable deformation features). The fact that the tension crack is subparallel to J2, supports that it is opening along pre-existing joints in the bedrock, similar to the backscarps.

The crack appears to also be connected with a NE-SW striking morphological depression. Morphological depressions can represent tensile openings in the bedrock, and the smaller-scale fractures in the depression augment the idea (Figure 38). Together these two structures form a wedge-shape parallel with both backscarp orientations at Mellomfjellet 1, and are likely connected to the development of the URS. The morphological depression is parallel with J1, indicating that it is forming along pre-existing structures in the bedrock.

There are two possible theories for the presence of the tension cracks upslope of the unstable area. The first is that the tension cracks are a newly-developing upper section of the URS, and represent a retrogressive lengthening in the URS. As the current unstable mass moves downslope removing material that is buttressing the stable mass, the stable mass is free to open along pre-existing joint surfaces, forming a tension crack. Following failure of the unstable mass, or over a significant time period, the tension cracks will likely become the new backscarps (Cruden and Varnes, 1996).

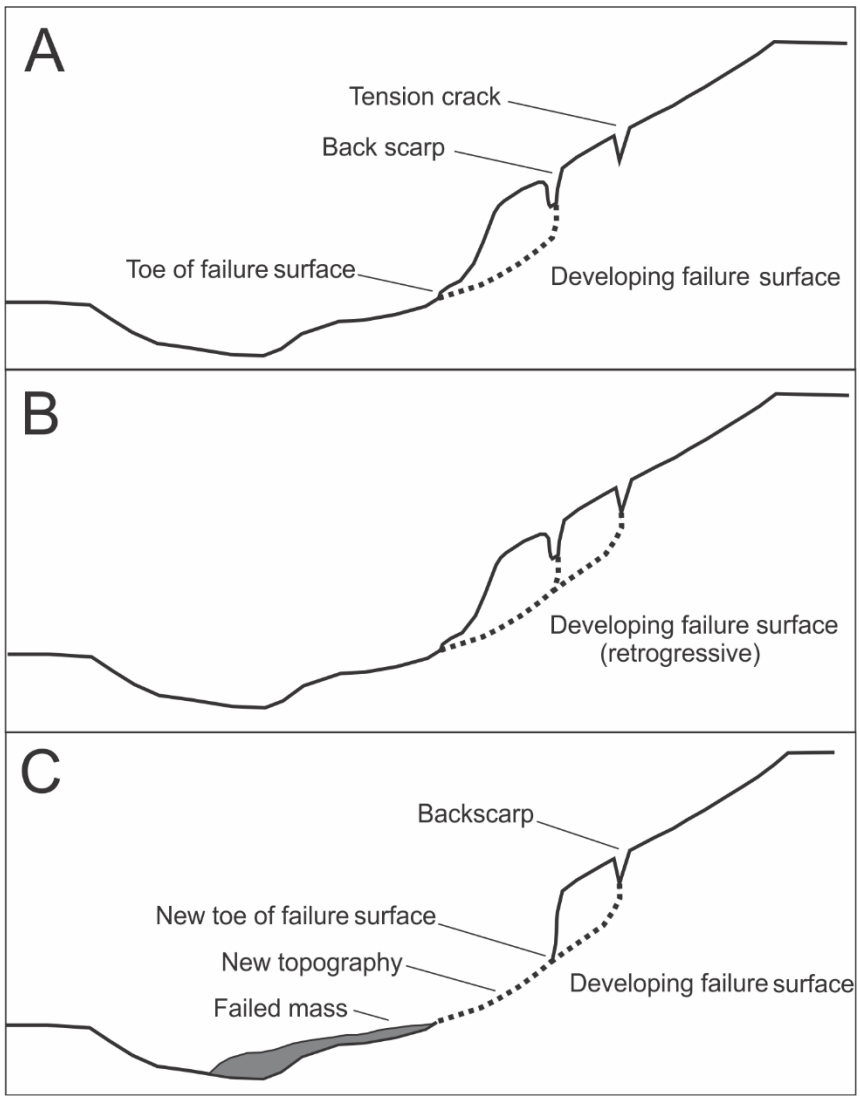

Figure 51: Sketch illustrating how the tension crack may represent a retrogressive failure (Cruden and Varnes, 1996). A) A situation similar to the present conditions at Mellomfjellet 1, with a tension crack upslope of the backscarp. B) The failure surface developing from the backscarp and up to the tension crack upslope, which could be the case for Mellomfjellet 1. C) Future development of the URS, with the tension crack developed as the new backscarp.

The second explanation could be that the tension cracks are due to gravitational drag caused by pre-failure masses. By using numerical modelling, Böhme et al. (2013) found that graben structures (or a tension crack, in this case) upslope of the backscarp could be developed prior to a prehistoric slope failure. Their findings showed that after removing the pre-historic masses, the tensile stress decreased in the graben areas, and became an inactive part of the URS (Figure 52). The tension cracks may therefore not be part of the present instability, but be remnant morphological structures of an earlier URS.

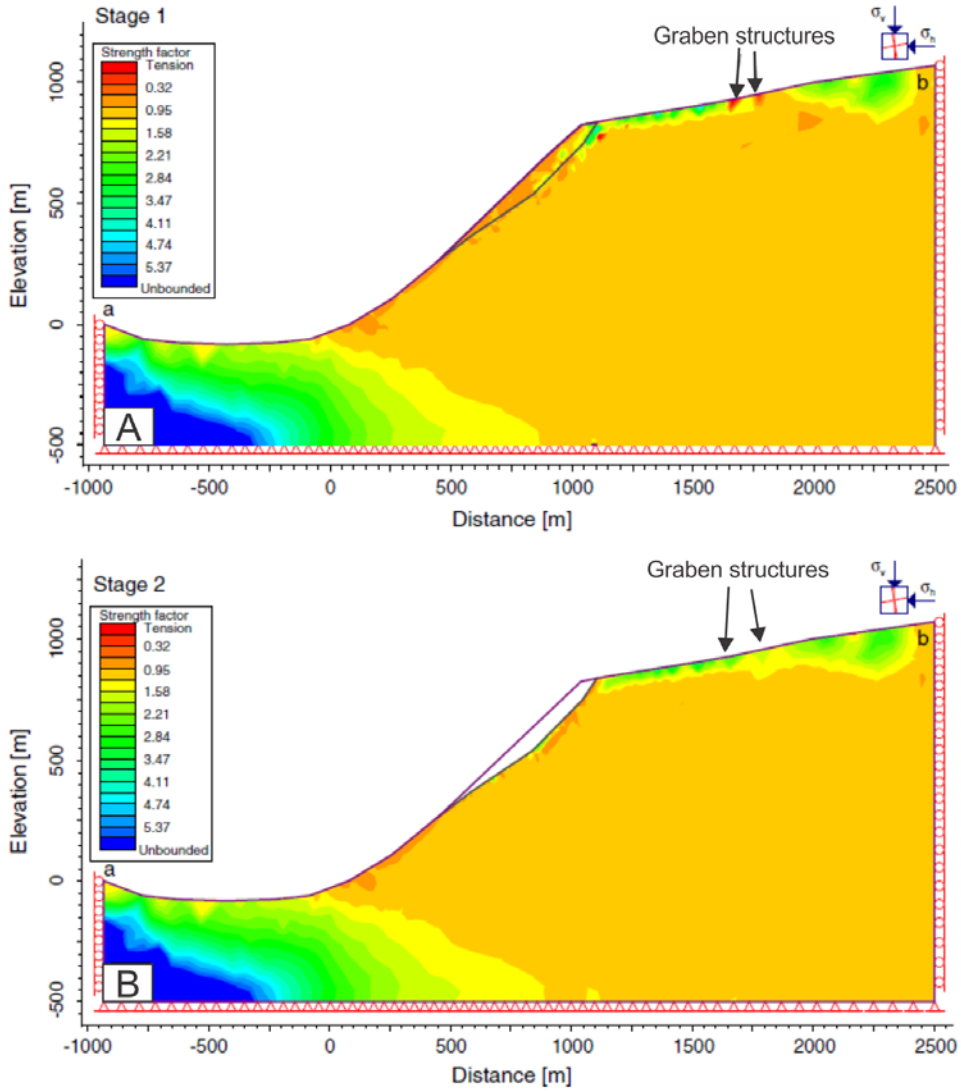

Figure 52: Figure presenting continuum modelling results, modified after Böhme et al. (2013). A) The strength factor before the prehistoric failure, with more mass acting on the slope, showing low strength where the graben structures are located. B) The strength factor based on current topography, after the prehistoric mass is removed. A high strength factor is present where the graben structures are located, indicating that it is inactive.

4.2.3 Disintegrating blocks and talus

The unstable area is divided into multiple slide blocks by the scarps. The block surfaces are highly fractured (Figure 39), indicating that deformation is taking place. Some blocks are clearly at a more advanced stage of deformation, especially in the southern area of Mellomfjellet 1 (Figure 34), where disintegration of blocks is likely be the source of the thick talus deposit downslope (Figure 40). This observation could indicate that the entire URS Mellomfjellet 1 is disintegrating, and that a catastrophic failure is not be expected. Thick talus and heavily disintegrating blocks were also found downslope of the two E-W striking morphological depressions. As previously discussed, large scale lineaments and depressions often indicate faults, as could be the case for the two E-W striking morphological depressions. E-W striking lineaments are found multiple places in Troms (Andresen, 2018), and are likely inherited E-W striking faults. The thick talus deposit and disintegrating blocks in this area could therefore be a result of localized deformation caused by large Post-Caledonian faults.

4.2.4 Felsic intrusion

A thin (>40 cm) foliation-parallel felsic intrusion was mapped within the surrounding amphibolite and hornblende schist bedrock, near to the toe of the URS. The intrusion shows signs of shearing deformation, supported by thin section analysis where the felsic mineral assemblages show signs of late-stage deformation, and from the SEM analysis of a weaker lens within the intrusion (Figure 32), where the presence of clay minerals suggests shearing has occurred at some point. The coating observed on the joint surfaces below the zone, suggests leeching of minerals due to groundwater flowing through the zone. It could therefore be that the change in lithology creates a boundary for groundwater flow, where the clay (with its low hydraulic conductivity) creates higher water pressure along the lithological boundary, hence lowering the shear strength by lowering the effective normal stress (Wyllie and Mah, 2004). Therefore it is possible that the zone is influencing the stability of the URS. However, the boundary is not interpreted to be the main failure surface for the URS, as it is located within the unstable area, hence there has to be a deeper failure surface.

It is worth noting that samples from the intrusion were only analysed from one specific area, and that the extent of the intrusion is not known, other than that similar zones were observed in the URS from distance. For the theory of a failure surface along the intrusion contact to be valid, one has to assume that the intrusion continues along the entire length of the URS.

4.3 InSAR

InSAR-derived displacement data can be related to morphological elements of the URSs to better understand how the URSs is deforming. Both InSAR-datasets show movement coinciding well with the mapped unstable area at Mellomfjellet (Figure 34, Figure 44 and Figure 45). All the measured downward displacement is occurring downslope of the area delimited by the mapped backscarps.

Analysis of the R-SAT InSAR profiles (Figure 44B and C) shows how the different morphological elements are controlling the movement. At Mellomfjellet 1, both Profile AA' and CC' show the largest displacement over the areas at the front (downslope), where the more disintegrated material is mapped, indicating that the larger blocks close to the backscarp are more confined than the lower blocks. Profile AA' at Mellomfjellet 1 shows that the largest change (increase) in displacement occurs across a subscarp separating two larger dislocated blocks, supporting the theory that the upper blocks are more confined. The Sentinel-1 data showed the same trends (Figure 45 A and B), with lower velocities recorded on the upper, confined blocks, and higher velocities at the lower, less confined blocks, supporting movement along subscarps.

Profile BB' (R-SAT), drawn across the assumed stable area, shows no sign of displacement, supporting the theory that no movement occurs upslope of the mapped backscarp. Neither of the InSAR datasets display data for the thick talus deposit south at Mellomfjellet 1, even though observations at the site indicate a movement within the mass (Figure 40). As this area contains a large amount of talus, there could be too much variation in movement within the mass due to tilting and movement of individual rocks for the satellite to recognize the same surfaces during each flyover.

Profile DD' (R-SAT), at Mellomfjellet 2 (Figure 44C), shows a very low displacement across the uppermost block within the unstable area, and that higher displacement is occurring on a lower block, the change in displacement corresponding well with a subscarp separating the two blocks. The same pattern is observed in the Sentinel-1 data (Figure 45C), where the upper block shows no displacement, while the lower block and smaller surrounding blocks shows downward displacement, indicating that the main displacement at Mellomfjellet 2 occurs along this subscarp.

Both LOS velocities from Sentinel-1 and R-SAT show a similar displacement pattern, with larger displacement rates at Mellomfjellet 1, but much higher velocities are recorded by

Sentinel-1 compared to R-SAT (Figure 44 and Figure 45). These differences might be due to a difference in LOS for the two data sets, where Sentinel-1 have an incidence angle of 42 and R-SAT have an incidence angle of 31. A lower incidence angle equals a steeper dip, when comparing it to the dip in a geological matter (Figure 10). Since both URSs are expected to slide along a low angled failure surface, the steep angle of R-SAT's LOS is probably the explanation for the lower velocities measured.

Only descending InSAR-datasets have been used, based on their favourable LOS for detecting downslope movement (2.2 and Figure 12A). When only descending datasets are used, movement in LOS only is detected, and most likely underestimating real displacement. By using both descending and ascending satellite paths, it is possible to decompose a 2D vector, giving information of both horizontal and vertical displacement in an E-W cross-section (Böhme et al., 2016b).

Displacement rates lower than 1 mm/year are close to lower detection limit for long time series (Bredal, 2016). Several areas, especially from the R-SAT data-set, showed movements below 1 mm/year, and these may therefore not reflect genuine geological processes. The processing method may also influence the results. Sentinel-1 and R-SAT-2 are processed using two different methods, and is probably the most important factor to have influenced the magnitude of the measured displacement.

4.4 Classification of the unstable rock slopes

4.4.1 Kinematics

The kinematic analysis provides insights as to which structures are problematic for failure, however it is important to validate the results by relating them to field observations, rather than to simply accept and present what the Dips model shows.

4.4.1.1 Mellomfjellet 1

The kinematic analysis (Figure 23) suggests that planar failure along the foliation is possible, with J2 functioning as a release surface. Even though the mean plane of the foliation dips shallower than the friction angle, the high variation caused by the undulating surfaces results in 44% of the foliation planes plotting steeper than the friction angle (20°; Table 4). As foliation-parallel planar failure was observed on a local scale in the field (Figure 31 and Figure 41), planar sliding is considered feasible.

The opening of the backscarp can give an indication on the movement of the unstable area. At Mellomfjellet 1, one of the backscarps had a 5 m horizontal and 1 m vertical opening (Figure 36), indicating a low angled sliding plane (Figure 53). However, this trend did not match all of the backscarps, where some also showed an equal ratio of horizontal and vertical displacement, indicating a steeper sliding plane. These observations can be explained by multiple failure surfaces or a listric failure surface (Braathen et al., 2004). The folded and undulating foliation leads to a more complex failure surface. The smooth roughness of the foliation (Table 9) does however lower the friction along the surface and increased the chance of sliding to occur (Wyllie and Mah, 2004).

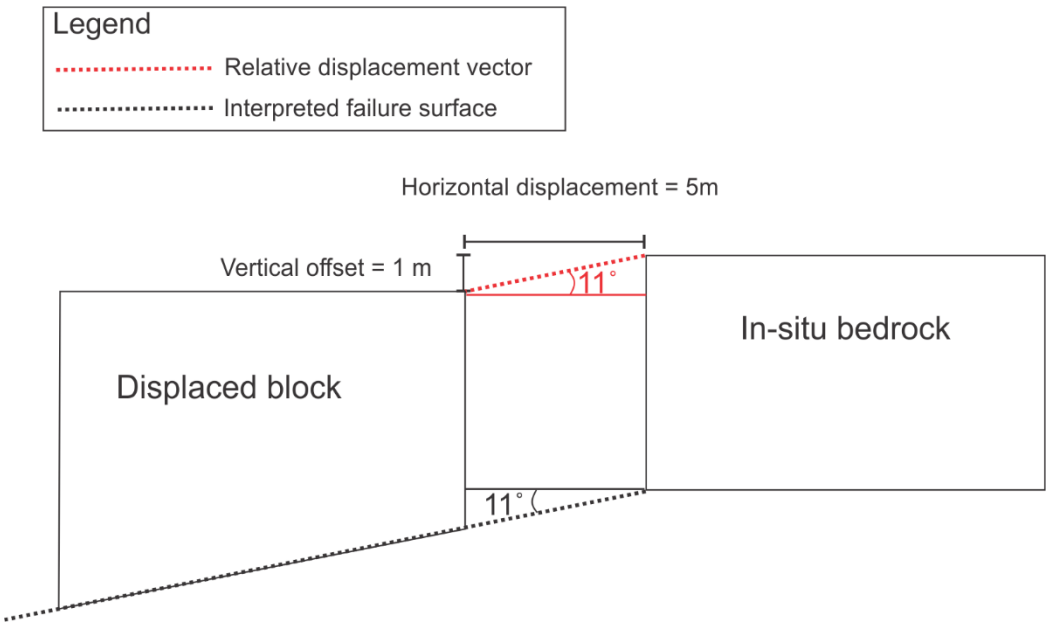

Figure 53: Sketch showing how the horizontal and vertical offset, which indicates a low angled failure surface, by calculating the relative displacement angle and assuming that is the angle of the failure surface. The average dip angle of the foliation was 13˚, corresponding well with the calculated failure surface.

A failure surface stepping between foliation and J1 surfaces is highly likely. This was observed on a local scale at most of the outcrops along the backscarp (Figure 27B and Figure 28), and is feasible from the kinematic analysis (3.1.4).

Flexural toppling failure is classified as *partly* possible along J1, a small number of surfaces in the set daylight inside the lateral limits (Figure 23). Small scale topples were observed to have happened in the NE-SW-striking scarps (Figure 42A).

4.4.1.2 Mellomfjellet 2

The kinematic analysis suggests that flexural toppling along J1 is possible, with the entire variability cone plotting within the critical area (Figure 24C), and partly possible along J3. Block toppling along a combination of J1 and the foliation was observed on a local scale in field (Figure 42B), which suggests that at a larger scale flexural toppling along J1 could be possible. No toppling along J3 was observed in the field, however the observations of J3 were limited.

Most of the variability cone for the foliation plotted outside the critical area for planar failure, however on a local scale biplanar failure in combination with J1 and J2 acting as release surfaces for foliation-sliding was observed (Figure 43B). A failure surface stepping between J2 and the foliation was commonly observed along outcrops near or parallel with the backscarp. The opening of the backscarp (10 m vertical and 20-25 m horizontal) suggests movement along a gently dipping planar failure surface.

4.4.2 Classification

Large URSs often have an increased structural complexity, compared to smaller failures, and therefore multiple failure modes may occur at the one site (Figure 54; Stead et al., 2006). In order to understand how the URS is failing, simple kinematic analysis alone is not sufficient. Therefore classification systems have been created, in order to better understand how the different structures connect and control the instability of the slope.

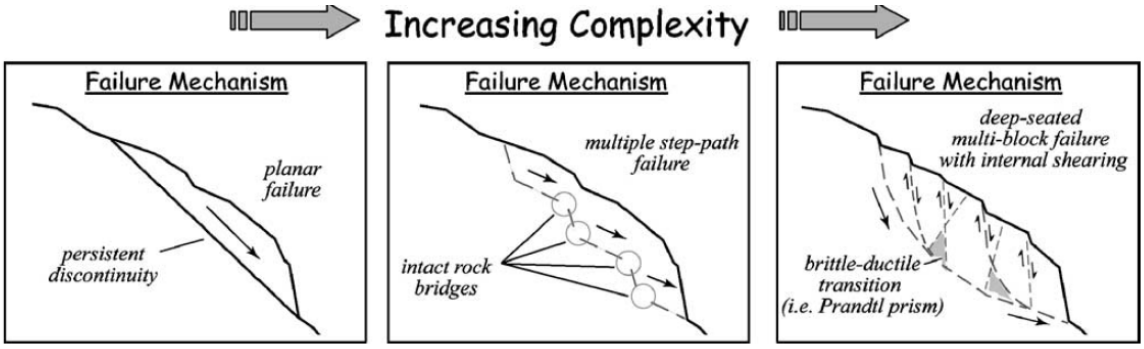

Figure 54: Flowchart showing how different failure mechanisms may be part of the same URS when the size and its complexity increases. Figure after Stead et al. (2006).

For this project, a combination of the systems developed by Braathen et al. (2004), Hermanns and Longva (2012) (including adaptations from Glastonbury and Fell (2010) and Braathen et al. (2004)), and Agliardi et al. (2001) have been used. Based on the results from the structural

and kinematic feasibility analysis, and field observations, Mellomfjellet 1 and 2 are compared to diagnostic features presented in the different systems.

DSGSD –defined by Agliardi et al. (2001), have multiple diagnostic features (Agliardi et al., 2012) that are found at Mellomfjellet 1 (Figure 55):

- Tensile features resembling tectonic lineaments (morphological depressions, scarps and tension cracks) are found in the upper part of the slope;
- Heavily fractured rock mass is found in the lower parts of the slope and active rockfall in front of the slope;
- The unstable area seems to be controlled by major structures such as faults and joints;
- It is formed along a glacial valley in rockmass consisting of foliated metamorphic rocks; and Low rates of displacement are observed.

However, some features typical for a DSGSD were not found at Mellomfjellet, such as:

- Counterscarps
- Double crested ridges
- Predicted failure volume greater than 0.5 km^3

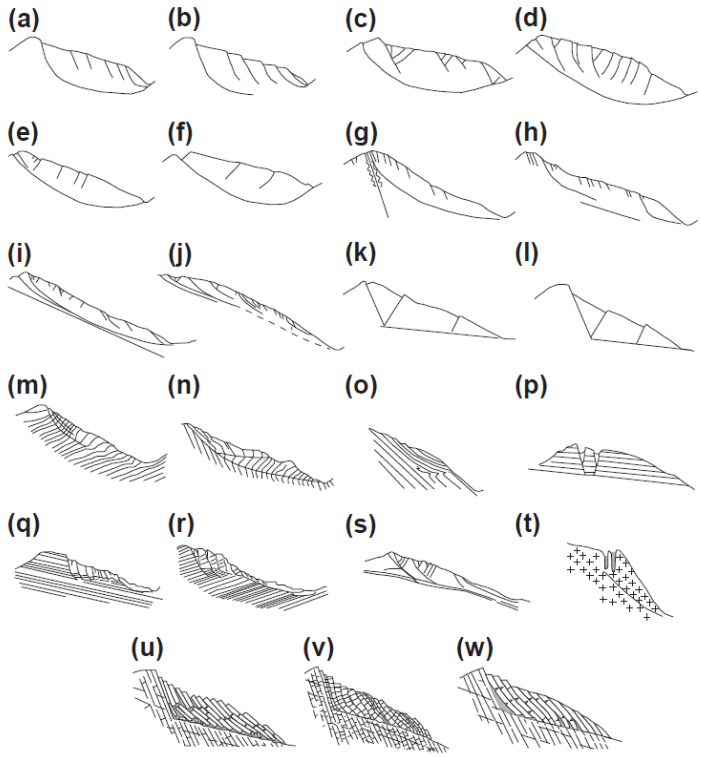

Figure 55: Different failure mechanisms for DSGSD, organized after structural control and failure geometry (Agliardi et al., 2012).

Diagnostic features typical for DSGSD have some cross over with other classification systems (Agliardi et al., 2001). Complex fields, defined by Braathen et al. (2004), also share most of the aforementioned features, with back bounding depressions, scarps, dislocated and fractured blocks above a low angled, deep-seated failure surface, as common features (Figure 56C).

Mellomfjellet 1 shares features similar to a biplanar compound slide, with low angled failure surface connected to a steeply dipping release surface (Figure 56A). Biplanar compound slides often occur in anisotropic bedrock, shows highly fractured slide mass characteristics, forms in glacial slopes and are sometimes influenced by water (Glastonbury and Fell, 2010). Internal shearing occurring normal to the anisotropy (foliation in this case), is also a common feature (Glastonbury and Fell, 2010). This is observed at Mellomfjellet 1 as well, with multiple steep subscarps showing high displacement (4.3) that are located within the rock mass.

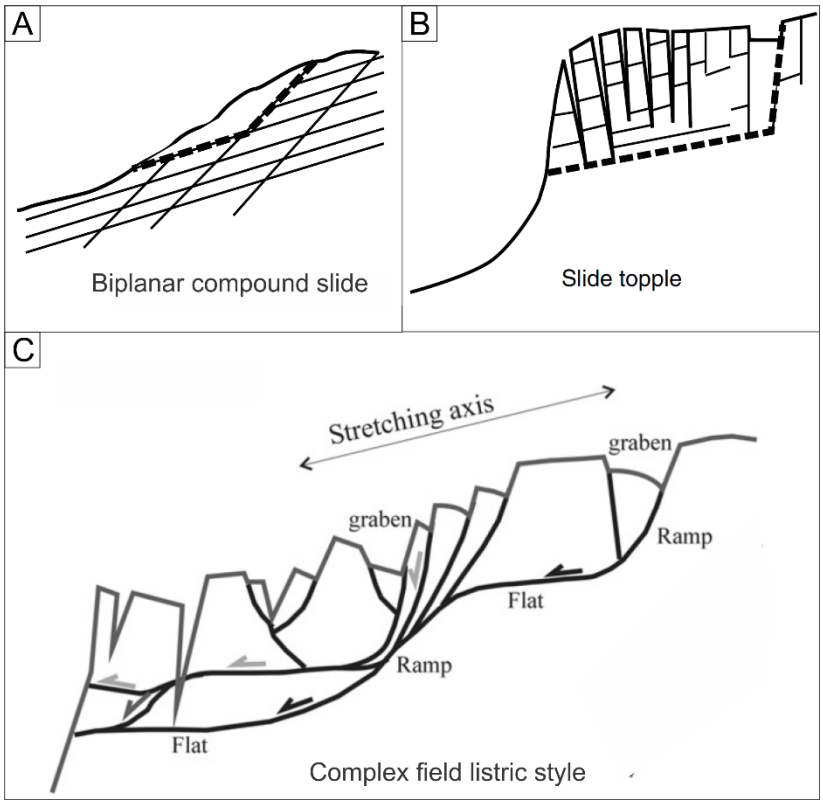

Figure 56: Examples of different classifications of URSs that show similar features as Mellomfjellet. A) Biplanar compound slide, after Hermanns and Longva (2012). B) Slide topple, after Hermanns and Longva (2012). C) Complex field listric style, modified after Braathen et al. (2004).

Mellomfjellet 2 shares very few typical DSGSD diagnostic features (Agliardi et al., 2001), and instead aligns more with a typical slide topple failure (Figure 56B; Hermanns and Longva, 2012). The kinematics suggest that flexural toppling is feasible (4.4.1). However, analysis of the backscarp opening (displaying the relative movement of the upper main block) indicates that sliding along a low angled failure surface is also occurring, and steeper surfaces within the foliation variability cone allow for planar sliding to occur (Table 5). A combination of J1 and the foliation (as observed on a local scale in field, Figure 29) likely forms the back- and basal-bounding surfaces of a slide topple mechanism.

Brideau and Stead (2009) used both 2D and 3D numerical modelling to investigated the role of the rear release surface, block size and lateral confinement on rock slope failure mechanisms where both toppling and sliding are possible. They found that the intact block size (based on spacing of discontinuities in in situ bedrock) as well as the dip angle of the rear release surface determined what kind of failure mode that was dominant. The dip angle of the rear release surface (J1) at Mellomfjellet 2 has a dip ranging between 67˚ to vertical (Figure 19 and Table 8), and a block size of 1x2x5 m (based on spacing of foliation, J1 and J2, Table 9). Based on

these values, the results of Brideau and Stead (2009) suggests that both a slide-topple, as well as pure sliding are possible failure modes at Mellomfjellet 2. It is important to note that there are uncertainties regarding the spacing assigned to the discontinuities, due to rough field estimates, which may affect the possibility for slide-topple to occur.

Mellomfjellet 2 also shares features similar to a biplanar compound slide, with a steep release surface and a low angled failure surface, highly fractured rock mass in anisotropic bed rock, located in a slope formed by glacial processes. Internal shearing occurring normal to the anisotropy is also observed along the subscarp, supported by high deformation rates from the InSAR-datasets.

4.5 Controlling factors

There are several factors that might influence and control the deformation occurring at Mellomfjellet 1 and 2. Ground water flow is an important factor influencing the stability of rock slopes (Wyllie and Mah, 2004), and may also lead to freezing of groundwater acting as controlling factors as well (when located in a cold climate).

At Mellomfjellet, no streams were observed flowing directly into the URSs, however multiple streams flowing from the lake at the peak and into boggy ground, towards the unstable area, indicates that water is flowing into the URSs. Due to the anisotropic and fractured nature of the rock mass it will have a high secondary permeability. If water flows into the slope, it is likely to be flowing through the fractured part of the rock. The presence of a band of vegetation at the assumed toe of the URSs indicates that there is a sudden presence of water here, and that groundwater seepage may be occurring. However, the vegetation may also be located there as the blocks provide shelter for rough weather.

The streams flowing out of the talus, downslope of the vegetated areas, together with the mineral coating below the zone of weakness discussed in chapter 3.2.2.6, supports the assumption of water flowing into the fractured material at the backscarp, and along a basal failure surface, and exiting near the toe of the URS.

The presence of groundwater within the fractures and on the basal failure surface will influence stability of the rockmass by increasing the pore pressure, lowering the effective stress, and thus lowering the stability of the slope (Crosta and Agliardi, 2003, Wyllie and Mah, 2004). Water may therefore act as one of the controlling factors for the deformation at Mellomfjellet.

When groundwater is present, freezing and thawing also needs to be addressed as a potential controlling factor. Freezing can block drainage patterns of ground water, resulting in a build-up of groundwater and thus lowering the stability of the rock mass, by increasing the pore pressure (Wyllie and Mah, 2004). Ice wedging may also occur, due to an increase in volume when groundwater freezes, which will expand existing fractures and contribute to the breaking of rock bridges. Snow and ice were found deep inside the large tension crack, and may support the idea that freezing of groundwater occurs at Mellomfjellet. However, this observation was made in September, and the snow and ice may be remains from the snowpack the previous winter. Nevertheless, freezing are believed to be a controlling factor for the deformation at Jettan (Blikra et al., 2015), a large URS located in the same general area as Mellomfjellet. Freezing and may therefore be a controlling factor for the deformation, due to the groundwater flow and climatic conditions.

4.6 Geological model

Based on the discussion of the morphological features in relation to the classification of the URSs, a geological model has been made for both of the sites. They are made as 2D profiles crossing the main morphological features (Figure 57).

At Mellomfjellet 1 (Figure 58A), a toe of failure is assumed to daylight somewhere in the talus area, as it was not observed in field. The felsic intrusion (3.2.2.6) is interpreted to be a failure surface for a smaller instability within the URS, and several subscarps are interpreted to connect to it at depth. This interpretation is supported by the observed trend from the InSAR data. The scarps are interpreted to connect to a basal failure surface due to a step-wise combination of J2 and the shallow dipping foliation. The tension crack is interpreted to be connected to the main failure surface, and to develop as the next backscarp when the blocks downslope has moved further down and made way for the upper part to slide (4.2.2).

At Mellomfjellet 2 (Figure 58B), the failure surface is interpreted to daylight in either the talus or in the forested area downslope of the talus. The vertical backscarp is interpreted to continue quite steep until a step-like combination connects it to the deep, shallow dipping failure surface (similar to the mechanism at Mellomfjellet 1).

For both domains there are uncertainties regarding the structural measurements, as previously discussed in chapter 4.1. Due to the lack of measurements at depth (e.g. borehole logging), there are high uncertainties regarding the structures at depth, where an assumed failure surface is

located. The felsic intrusion is for instance not included in the model at Mellomfjellet 2, due to high uncertainties in its lateral extent.

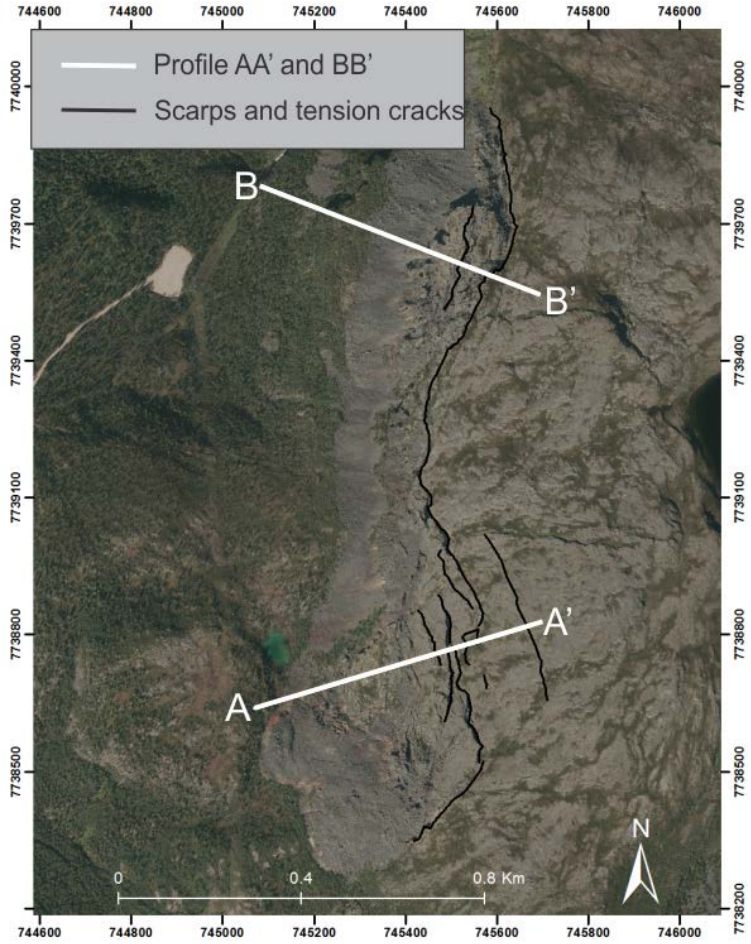

Figure 57: Map showing the location of the profile AA' and BB' used for the geological model at Mellomfjellet 1 and Mellomfjellet 2, respectively.

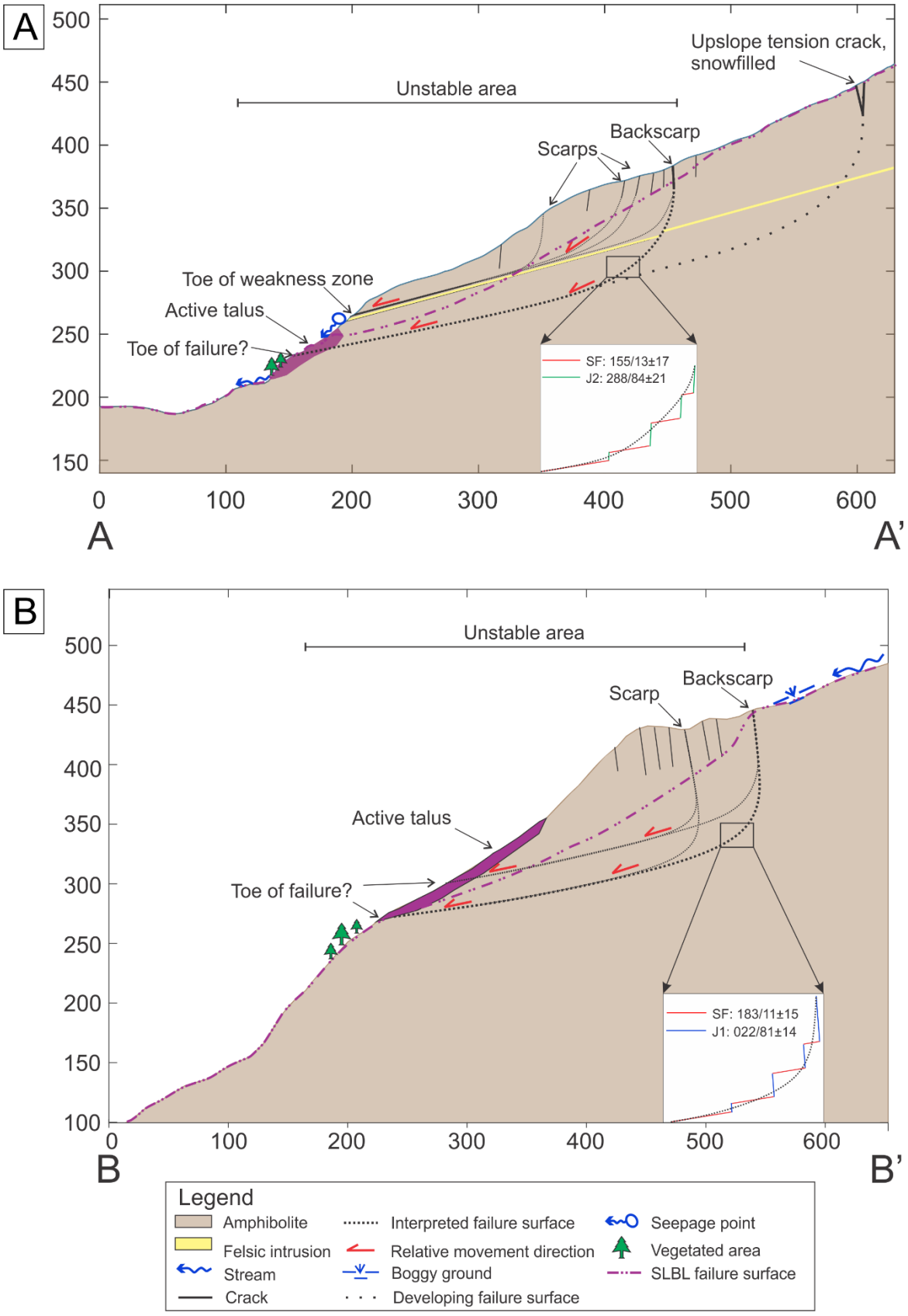

Figure 58: Geological model of Mellomfjellet 1 and 2. Note that this is a schematic profile based on interpretations of failure at depth, where only the major structures are included. A) Geological model of Mellomfjellet 1, along profile AA'. B) Geological model of Mellomfjellet 2, along profile BB'.

4.7 Hazard analysis

The hazard analysis performed resulted in both scenarios ending up with a medium hazard (Table 11). There are however numerous uncertainties associated with the different scores assigned in the analysis. There are uncertainties regarding potential sliding structures at depth, as all data was gathered from outcrops at the surface (as previously discussed in 4.6) and no subsurface data could be considered. Uncertainties are also present regarding the displacement rates, as InSAR only provides displacement rates in the LOS, and may therefore underestimate the displacement (as discussed in chapter 4.3, and illustrated in Figure 12A), and therefore reduce the hazard score. Talus deposits covering the lower part of the URS results in uncertainties, as it may hide a potential rupture surfaces, thus lowering the hazard score.

4.8 Volume estimations and run-out analysis

Uncertainties exists within the volume estimations, as no subsurface data could be considered for the scenarios. As discussed in chapter 4.4, both scenarios are believed to slide along deep planar failure surfaces in combination with subvertical to vertical release surfaces along the backscarp. Hence, the SLBL shape used for volume calculations might be a geometrical underestimation. An underestimated volume will (generally) lead to an underestimation of the run out distance. For URSs where there is a clear structural control, like Mellomfjellet, Oppikofer et al. (2016b) found that volume estimations are more accurate when constructing the failure surfaces in 3D. This method was tested for Mellomfjellet, but due to the resolution and quality of the Arctic DEM (3x3 m) structural surfaces were hard to identify, and the method was therefore dismissed.

The run out modelling conducted in Flow-R determined the run out length based on the Scheidegger curve (2.7). Blikra et al. (2001) found several weaknesses with the Scheidegger curve. Norwegian events typically plot above the curve (also illustrated in Figure 14), and therefore have a higher angle of reach, hence a lower run out distance than predicted by the Scheidegger equation. The maximum run-out distance may therefore be estimated as too high.

The run out analysis at Mellomfjellet 1 shows that no settlement or infrastructure is in danger of being hit by a rock avalanche. A bedrock knob downslope of Mellomfjellet 1 blocks the failure from continuing west towards settlements and rivers (Figure 47). Therefore no human lives are at risk if a potential failure occurs at Mellomfjellet 1, as long as there are not any people out for recreational purposes.

For Mellomfjellet 2, the run out analysis shows that a potential failure is likely to cover the new power line, as well as the construction site and parts of the construction road (Figure 48). As construction work is expected to finish in 2020/2021, human lives may be in danger if a failure occurs before the construction work finishes, but this is considered highly unlikely. The construction road is open for the public, and was used both by the author during the field campaign, and by people living in the area. Therefore, humans could be in the area when a failure occurs. A river flowing down the northern side of Mellomfjellet 2 has a high chance of being covered. However, due to the steep topography and narrow shape of the river canyon, it is likely that the river will divert further north, and damming of the river is not likely to occur.

5 Conclusion

The main findings of the structural assessment and characterization of the unstable rock slopes at Mellomfjellet are summarised and listed below:

- Based on analyses of stereoplots from 31 different stations, in combination with analyses of lineaments and morphological features, the area was divided into two structural domains: Mellomfjellet 1 and Mellomfjellet 2. Structures determined in the domains are:
    - Mellomfjellet 1: SF (155/13 ± 17), J1 (029/72 ± 16), J2 (288/84 ± 21), J3 (075/67 ± 12)
    - Mellomfjellet 2: SF (183/11 ± 15), J1 (022/81 ± 14), J2 (108/88 ± 15), J3 (075/47 ± 17)
- Three of the four sets were identified in Coltop3D when analysing the point cloud: SF (166/22 ± 13), J1 (006/72 ± 17), J2 (289/85 ± 16). Results from structural analysis based on data gathered in Coltop3D showed a difference when comparing it to field measurements, but are the same when taking the variance into account. The biggest uncertainty is introduced by the low precision of the GCPs.
- Kinematic analysis was executed for both of the structural domains, where the following failure modes were found feasible:
    - Mellomfjellet 1: Planar sliding possible within variations of the foliation, and flexural toppling partly possible along J1
    - Mellomfjellet 2: Flexural toppling possible along J1, and planar sliding possible within variations of the foliation
- Field observations supports that planar sliding is occurring at both domains, along a deep lying failure surface. A failure surface stepping between the foliation and J1 and J2 is highly likely.
- A felsic intrusion was identified at Mellomfjellet 1, and interpreted as a potential sliding surface, based on field observations, thin section- and SEM-analysis.
- The backscarps are subparallel to parallel with J1 and J2, striking in two main directions: NNW-SSE and NNE-SSW. These orientations coincide well with the strike of regional faults in Troms and supports that the unstable areas are disintegrating along pre-existing joints in the bedrock.

- Displacement from InSAR-datasets coincided well with the mapped features delimiting the unstable area.
- Both URSs showed diagnostic features that allowed for an assessment of the failure mechanism type:
    - Mellomfjellet 1 show multiple diagnostic features typical for a DSGSD, but also lacks several features one would expect for a DSGSD. It also shares features similar to a biplanar compound slide, as well as a complex field.
    - Mellomfjellet 2 also shares features typical for a biplanar compound slide, as well as a slide topple. When taking the results from the kinematic analysis into account, a slide topple is a possible classification for the URS.
- Water flow along the failure main surface may be the controlling factor for the deformation, based on the mapped streams, boggy ground and vegetation close to the top and the toe of the unstable area.
- Freezing and may be a controlling factor for the deformation due to the groundwater flow and climatic conditions.
- Hazard analysis concluded that both scenarios are classified within the medium hazard class. The highest uncertainties within the analysis are the displacement rates and the toe of rupture, which may have resulted in an underestimated hazard value for the scenarios.
- Volume estimations for the two domains are: Mellomfjellet 1: 1.12×10^6 m^3. Mellomfjellet 2: 3.05×10^6 m^3. There are however uncertainties with the estimated depths of the two scenarios, and a deeper failure surface would result in a much larger volume.
- A potential run-out at Mellomfjellet 1 is estimated to have a maximum run-out length of 695 m, where no infrastructure or rivers are in danger of being struck. A run-out at MF2 is estimated to have a 985 m run-out length, with a construction site, a new power line and a river located in the run-out zone. The construction work is estimated to finish within 2021, and the river is not prone for damming due to favourable topography. No human lives are therefore at risk, as long as no one is in the area for recreational purposes.

5.1 Further work

Based on the low consequence of a potential rock slope failure, Hermanns et al. (2012b) recommends that further follow up of the sites are not economically sustainable. However, from a scientific point of view, there are many things that could be done in order to get a better understanding of the two sites at Mellomfjellet.

A high resolution DEM (1x1 m) would be beneficial, to estimate the volume by constructing failure surfaces in 3D, as discussed in chapter 4.8. 3D vectors of the displacement could be obtained by establishing ground based InSAR at the base of the slope, and combining the measurements with ascending and descending satellite InSAR data (Eriksen, 2017). 3D vectors could also be obtained by establishing Global Navigational Satellite Systems (GNSS) antennas and measuring differential GNSS (Böhme et al., 2016b). Boreholes could give vital information regarding structures at depth. Borehole logging, combined with the use of either optical televiewer or acoustic televiewer could identify orientations of defects at depth, and identify potential failure surfaces. Different sensors could also be installed in the boreholes (e.g. piezometer, thermometer and DMS columns). DMS columns containing inclinometers could reveal displacement at depth, making it possible to identify failure surfaces, and obtaining 3D displacement vectors at depth. Combining these data with groundwater and temperature data (from piezometers and temperature loggers, respectively), seasonal patterns controlling the deformation could be obtained, similar to Jettan (Blikra et al., 2015).

Works cited

AGLIARDI, F., CROSTA, G. & FRATTINI, P. 2012. 18 Slow rock-slope deformation. *Landslides: Types, mechanisms and modeling***,** 207.

AGLIARDI, F., CROSTA, G., ZANCHI, A. & AGLIARDI, F. 2001. Structural constraints on deep-seated slope deformation kinematics. *Engineering Geology,* 59**,** 83-102.

ANDRESEN, M. L. 2018. *Regional structural analysis of rock slope failure types, mechanisms and controlling bedrock structures in Kåfjorden, Troms.* UiT Norges arktiske universitet.

BALLANTYNE, C. K. 2002. Paraglacial geomorphology. *Quaternary Science Reviews,* 21**,** 1935-2017.

BEMIS, S. P., MICKLETHWAITE, S., TURNER, D., JAMES, M. R., AKCIZ, S., THIELE, S. T. & BANGASH, H. A. 2014. Ground-based and UAV-based photogrammetry: A multi-scale, high-resolution mapping tool for structural geology and paleoseismology. *Journal of Structural Geology,* 69**,** 163-178.

BERGH, S. G., EIG, K., KLØVJAN, O. S., HENNINGSEN, T., OLESEN, O. & HANSEN, J.-A. 2007. The Lofoten-Vesterålen continental margin: a multiphase Mesozoic-Palaeogene rifted shelf as shown by offshore-onshore brittle fault-fracture analysis. *Norwegian Journal of Geology/Norsk Geologisk Forening,* 87.

BERGSTRØM, B. 1983. Deglaciation of the Reisa Valley, northern Norway, and studies of glacial deposits and dispersal processes. *Acta geológica hispánica,* 18**,** 161-167.

BLIKRA, L., BRAATHEN, A. & SKURTVEIT, E. 2001. Hazard evaluation of rock avalanches; the Baraldsnes–Oterøya area. *Geological Survey of Norway (NGU), Report,* 2001.108.

BLIKRA, L., LONGVA, O., BRAATHEN, A., ANDA, E., DEHLS, J. & STALSBERG, K. 2006. Rock slope failures in Norwegian fjord areas: examples, spatial distribution and temporal pattern. *Landslides from massive rock slope failure.* Springer.

BLIKRA, L. H. & CHRISTIANSEN, H. H. 2014. A field-based model of permafrost-controlled rockslide deformation in northern Norway. *Geomorphology,* 208**,** 34-49.

BLIKRA, L. H., CHRISTIANSEN, H. H., KRISTENSEN, L. & LOVISOLO, M. 2015. Characterization, geometry, temporal evolution and controlling mechanisms of the Jettan Rock-Slide, Northern Norway. *Engineering Geology for Society and Territory-Volume 2.* Springer.

BRAATHEN, A., BLIKRA, L. H., BERG, S. S. & KARLSEN, F. 2004. Rock-slope failures in Norway; type, geometry, deformation mechanisms and stability. *Norwegian Journal of Geology/Norsk Geologisk Forening,* 84.

BREDAL, M. 2016. *A structural, geomorphological and InSAR study of the unstable rock slope in Oksfjellet, Kåfjord, Troms.* UiT Norges arktiske universitet.

BRIDEAU, M. & STEAD, D. The role of rear release surfaces, block size and lateral confinement on rock slope failure mechanisms. 62nd Canadian geotechnical conference and 10th joint groundwater CGS/IAH-CNC conference. Halifax, Nova Scotia, 2009. 489-496.

BRIDEAU, M., YAN, M. & STEAD, D. 2009. The role of tectonic damage and brittle rock fracture in the development of large rock slope failures. *Geomorphology,* 103**,** 30-49.

BUNKHOLT, H., OTTERÅ, S., YUGSI MOLINA, F., HERMANNS, R., DEHLS, J., OSMUNDSEN, P., REDFIELD, T., EIKEN, T. & BÖHME, M. 2013. Undersøkelser av ustabile fjellpartier i Troms–status og planer etter feltarbeid 2011 og 2012. *NGU Rapport 2013.021*.

BÖHME, M. 2014. Spatial and temporal variability of rock slope instability in western Norway: Implications for susceptibility and hazard assessment.

BÖHME, M., BUNKHOLT, H., DEHLS, J., OPPIKOFER, T., HERMANNS, R., DALSEGG, E., KRISTENSEN, L., LAUKNES, T. & ERIKSEN, H. 2016a. Geologisk modell og fare-og risikoklassifisering av det ustabile fjellpartiet Gamanjunni 3 i Manndalen, Troms. *NGU Rapport,* 64.

BÖHME, M., BUNKHOLT, H., OPPIKOFER, T., DEHLS, J., HERMANNS, R., ERIKSEN, H., LAUKNES, T. & EIKEN, T. Using 2D InSAR, dGNSS and structural field data to understand the deformation mechanism of the unstable rock slope Gamanjunni 3, northern Norway. Landslides and Engineered Slopes: Experience, Theory and Practice: Proceedings of the 12th International Symposium on Landslides (Napoli, Italy, 12–19 June 2016): Rome, Associazione Geotecnica Italiana, 2016b. 443-449.

BÖHME, M., HERMANNS, R., OPPIKOFER, T., FISCHER, L., BUNKHOLT, H., EIKEN, T., PEDRAZZINI, A., DERRON, M.-H., JABOYEDOFF, M. & BLIKRA, L. 2013. Analyzing complex rock slope deformation at Stampa, western Norway, by integrating geomorphology, kinematics and numerical modeling. *Engineering geology,* 154**,** 116-130.

CORFU, F., ANDERSEN, T. & GASSER, D. 2014. The Scandinavian Caledonides: main features, conceptual advances and critical questions. *Geological Society, London, Special Publications,* 390**,** SP390. 25.

CROSTA, G. & AGLIARDI, F. 2003. Failure forecast for large rock slides by surface displacement measurements. *Canadian Geotechnical Journal,* 40**,** 176-191.

CRUDEN, D. & VARNES, D. 1996. Landslides: investigation and mitigation. Chapter 3-Landslide types and processes. *Transportation research board special report.*

DORÉ, A., LUNDIN, E., FICHLER, C. & OLESEN, O. 1997. Patterns of basement structure and reactivation along the NE Atlantic margin. *Journal of the Geological Society,* 154**,** 85-92.

ERIKSEN, H. Ø. 2013. *Slope displacement patterns observed using satellite InSAR data in the Storfjord-Kåfjord-Lyngen region, Troms.* Universitetet i Tromsø.

ERIKSEN, H. Ø. 2017. Combining Satellite and Terrestrial Interferometric Radar Data to Investigate Surface Displacement in the Storfjord and Kåfjord Area, Northern Norway.

ESA. 2019. *Resolution and Swath* [Online]. Available: https://sentinel.esa.int/web/sentinel/missions/sentinel-1/instrument-payload/resolution-swath [Accessed 05.05. 2019].

EVERARD, K. A. 1994. *Regional characterization of large landslides in southwest Yukon, with emphasis on the role of neotectonics.* University of British Columbia.

FALEIDE, J. I., TSIKALAS, F., BREIVIK, A. J., MJELDE, R., RITZMANN, O., ENGEN, O., WILSON, J. & ELDHOLM, O. 2008. Structure and evolution of the continental margin off Norway and the Barents Sea. *Episodes,* 31**,** 82-91.

GLASTONBURY, J. & FELL, R. 2010. Geotechnical characteristics of large rapid rock slides. *Canadian Geotechnical Journal,* 47**,** 116-132.

GLIMSDAL, S. & HARBITZ, C. 2007. Flodbølger etter mulig fjellskred, Nordnes, Lyngen kommune. Beregning av mulige fjellskred og flodbølger. *NGI Rapport 20071677,* 1.

HANSEN, J.-A. & BERGH, S. 2012. Origin and reactivation of fracture systems adjacent to the Mid-Norwegian continental margin on Hamarøya, North Norway: use of digital geological mapping and morphotectonic lineament analysis. *Norwegian Journal of Geology/Norsk Geologisk Forening,* 92.

HENDERSON, I., OSMUNDSEN, P. & REDFIELD, T. 2010. ROS Fjellskred i Troms: Status og planer, 2009. *Norges geologiske undersøkelse, Rapport.*

HERMANNS, R., HANSEN, L., SLETTEN, K., BÖHME, M., BUNKHOLT, H., DEHLS, J., EILERTSEN, R., FISCHER, L., LHEUREUX, J. & HØGAAS, F. 2012a. Systematic

geological mapping for landslide understanding in the Norwegian context. *Landslide engineered slopes: protecting society through improved understanding. Taylor Francis Group, London***,** 265-271.

HERMANNS, R., OPPIKOFER, T., ANDA, E., BLIKRA, L., BÖHME, M., BUNKHOLT, H., CROSTA, G., DAHLE, H., DEVOLI, G. & FISCHER, L. 2012b. Recommended hazard and risk classification system for large unstable rock slopes in Norway. *NGU rapport,* 2012.029.

HERMANNS, R., OPPIKOFER, T., ANDA, E., BLIKRA, L., BÖHME, M., BUNKHOLT, H., CROSTA, G., DAHLE, H., DEVOLI, G. & FISCHER, L. 2013. Hazard and risk classification for large unstable rock slopes in Norway. *Italian Journal of Engineering Geology Environment,* 2013**,** 245-254.

HERMANNS, R. L. & LONGVA, O. 2012. Rapid rock-slope failures. *Landslides: types, mechanisms and modeling***,** 59-70.

HERMANNS, R. L., OPPIKOFER, T., MOLINA, F. X. Y., DEHLS, J. F. & BÖHME, M. 2014. Approach for systematic rockslide mapping of unstable rock slopes in Norway. *Landslide science for a safer geoenvironment.* Springer.

HERNES, I. 2014. *Fjellskred ved Indre Nordnes, Nordnesfjellet, Lyngen, Troms-Berggrunnens indre struktur og bevegelsesmekanismer basert på strukturell analyse og overvakingsdata.* UiT Norges arktiske universitet.

HOLMGREN, P. 1994. Multiple flow direction algorithms for runoff modelling in grid based elevation models: an empirical evaluation. *Hydrological processes,* 8**,** 327-334.

HORTON, P., JABOYEDOFF, M., RUDAZ, B. E., AL & ZIMMERMANN, M. 2013. Flow-R, a model for susceptibility mapping of debris flows and other gravitational hazards at a regional scale. *Natural Hazards and Earth System Sciences,* 13**,** 869-885.

HUSBY, E. D. 2011. *Fjellskred i Nomedalstinden: En strukturstyrt masseutglidning på et underliggende storskala glideplan.* Universitetet i Tromsø.

INDREVÆR, K., BERGH, S. G., KOEHL, J.-B., HANSEN, J.-A., SCHERMER, E. R. & INGEBRIGTSEN, A. 2013. Post-Caledonian brittle fault zones on the hyperextended SW Barents Sea margin: New insights into onshore and offshore margin architecture. *Norwegian Journal of Geology,* 93.

JABOYEDOFF, M., BAILLIFARD, F., COUTURE, R., LOCAT, J., LOCAT, P. J. L. E., STABILIZATION. BALKEMA, T. & FRANCIS GROUP, L. 2004. Toward preliminary hazard assessment using DEM topographic analysis and simple mechanical modeling by means of sloping local base level. *Landslides: evaluation and stabilization. Balkema, Taylor & Francis Group, London***,** 199-206.

JABOYEDOFF, M., METZGER, R., OPPIKOFER, T., COUTURE, R., DERRON, M., LOCAT, J. & TURMEL, D. New insight techniques to analyze rock-slope relief using DEM and 3D-imaging cloud points: COLTOP-3D software. Rock mechanics: Meeting Society's Challenges and demands, 2007. 61-68.

JABOYEDOFF, M., METZGER, R., OPPIKOFER, T., VIERO, A. & GALGARO, A. 2009. Coltop3D: a new software for structural analysis with high resolution 3D point clouds and DEM. *AAPG Search and Discovery Article,* 90171**,** 4-8.

KAMPES, B. M. 2006. Radar interferometry: Persistent Scatterer Technique. *Remote Sensing and Digital Image Processing, 12, Springer Netherlands.***,** 5-30.

LAUKNES, T., SHANKER, A. P., DEHLS, J., ZEBKER, H., HENDERSON, I. & LARSEN, Y. 2010. Detailed rockslide mapping in northern Norway with small baseline and persistent scatterer interferometric SAR time series methods. *Remote Sensing of Environment,* 114**,** 2097-2109.

LAUKNES, T. R. 2011. Rockslide mapping in Norway by means of interferometric SAR time series analysis.

MALLISON, H. 2018. *Photogrammetry tutorial 11: How to handle a project in Agisoft Photoscan* [Online]. Available: https://dinosaurpalaeo.wordpress.com/2015/10/11/photogrammetry-tutorial-11-how-to-handle-a-project-in-agisoft-photoscan/ [Accessed 28.10. 2018].

MASSONNET, D. & FEIGL, K. L. 1998. Radar interferometry and its application to changes in the Earth's surface. *Reviews of geophysics,* 36**,** 441-500.

MICHELETTI, N., CHANDLER, J. H. & LANE, S. N. 2015. Structure from motion (SFM) photogrammetry. *Geomorphological Techniques (Online Edition).* London: British Society for Geomorphology.

NGU. 2019. *Ustabile fjellparti - Nasjonal database for ustabile fjellparti* [Online]. Available: http://geo.ngu.no/kart/ustabilefjellparti_mobil/ [Accessed 11.05. 2019].

OPPIKOFER, T., BÖHME, M., NICOLET, P., PENNA, I. & HERMANNS, R. 2016a. Metodikk for konsekvensanalyse av fjellskred. *NGU Report .047*.

OPPIKOFER, T., HERMANNS, R. L., SANDØY, G., BÖHME, M., JABOYEDOFF, M., HORTON, P., ROBERTS, N. J. & FUCHS, H. 2016b. Quantification of casualties from potential rock-slope failures in Norway. *Landslides and Engineered Slopes: Experience, Theory and Practice***,** 1537-1544.

OPPIKOFER, T., JABOYEDOFF, M., PEDRAZZINI, A., DERRON, M. H. & BLIKRA, L. H. 2011. Detailed DEM analysis of a rockslide scar to characterize the basal sliding surface of active rockslides. *Journal of Geophysical Research: Earth Surface,* 116.

OPPIKOFER, T., NORDAHL, B., BUNKHOLT, H., NICOLAISEN, M., JARNA, A., IVERSEN, S., HERMANNS, R. L., BÖHME, M. & MOLINA, F. X. Y. 2015. Database and online map service on unstable rock slopes in Norway—From data perpetuation to public information. *Geomorphology,* 249**,** 69-81.

PARK, H. & WEST, T. 2002. Sampling bias of discontinuity orientation caused by linear sampling technique. *Engineering Geology,* 66**,** 99-110.

RAMBERG, I., BRYHNI, I. & NØTTVEDT, A. 2007. *Landet blir til: Norges geologi*, Norsk geologisk forening.

RASMUSSEN, E. 2011. *Fjellskred i Laksvatnfjellet, Balsfjord, Troms: indre struktur, morfologi og skredmekanismer.* Universitetet i Tromsø.

ROCSCIENCE. 2018a. *Dips* [Online]. Available: https://www.rocscience.com/software/dips [Accessed 07.11 2018].

ROCSCIENCE. 2018b. *Dips7.0: Tutorial 4 Toppling, Planar Sliding, Wedge Sliding* [Online]. Available: https://www.rocscience.com/help/dips/pdf_files/tutorials/Tutorial_04_Toppling_Planar_and_Wedge_Sliding.pdf [Accessed 06.12 2018].

ROSEN, P. A., HENSLEY, S., JOUGHIN, I. R., LI, F. K., MADSEN, S. N., RODRIGUEZ, E. & GOLDSTEIN, R. M. 2000. Synthetic aperture radar interferometry. *Proceedings of the IEEE,* 88**,** 333-382.

SAVIGNY, W. & CLAGUE, J. 1992. Technical Tour No. 2: Fraser valley and Fraser Canyon Areas. *Proceeding of GeoHazards,* 92.

SCHEIDEGGER, A. E. 1973. On the prediction of the reach and velocity of catastrophic landslides. *Rock Mechanics and Rock Engineering,* 5**,** 231-236.

SKREDE, I. 2013. *Jettan, Nordnesfjellet, Kåfjord, Troms–indre geometri og struktur, kinematikk og styrande faktorar av eit ustabilt fjellparti, basert på strukturellanalyse, geomorfologi og overvakingsdata.* UiT Norges arktiske universitet.

STATNETT. 2018. *God fremdrift nordover* [Online]. Available: https://www.statnett.no/her-bygger-vi/region-nord/balsfjord--skaidi/Nyheter/god-fremdrift-nordover2/ [Accessed 26.04 2019].

STEAD, D., EBERHARDT, E. & COGGAN, J. 2006. Developments in the characterization of complex rock slope deformation and failure using numerical modelling techniques. *Engineering geology,* 83**,** 217-235.
TERZAGHI, R. D. 1965. Sources of error in joint surveys. *Geotechnique,* 15**,** 287-304.
TRAVELLETTI, J., DEMAND, J., JABOYEDOFF, M. & MARILLIER, F. 2010. Mass movement characterization using a reflexion and refraction seismic survey with the sloping local base level concept. *Geomorphology,* 116**,** 1-10.
WYLLIE, D. C. & MAH, C. W. 2004. Rock slope engineering: civil and mining. *Spon Press, New York*.
ZWAAN, K. 1988. *Geologisk kart over Norge. Berggrunnskart NORDREISA-M 1: 250 000*.
ZWAAN, K. 1995. Geology of the West Troms Basement Complex, northern Norway, with emphasis on the Senja Shear Belt: a preliminary account. *Geological Survey of Norway Bulletin,* 427**,** 33-36.
ZWAAN, K., RYGGHAUG, P. & ZOBEL, W. 1984. Reisadalen 1734 III, bergrunnsgeologisk kart, foreløbig utgave. *Norges Geologiske Undersøkelse*.

Appendix

Appendix A: Structural map Mellomfjellet 1

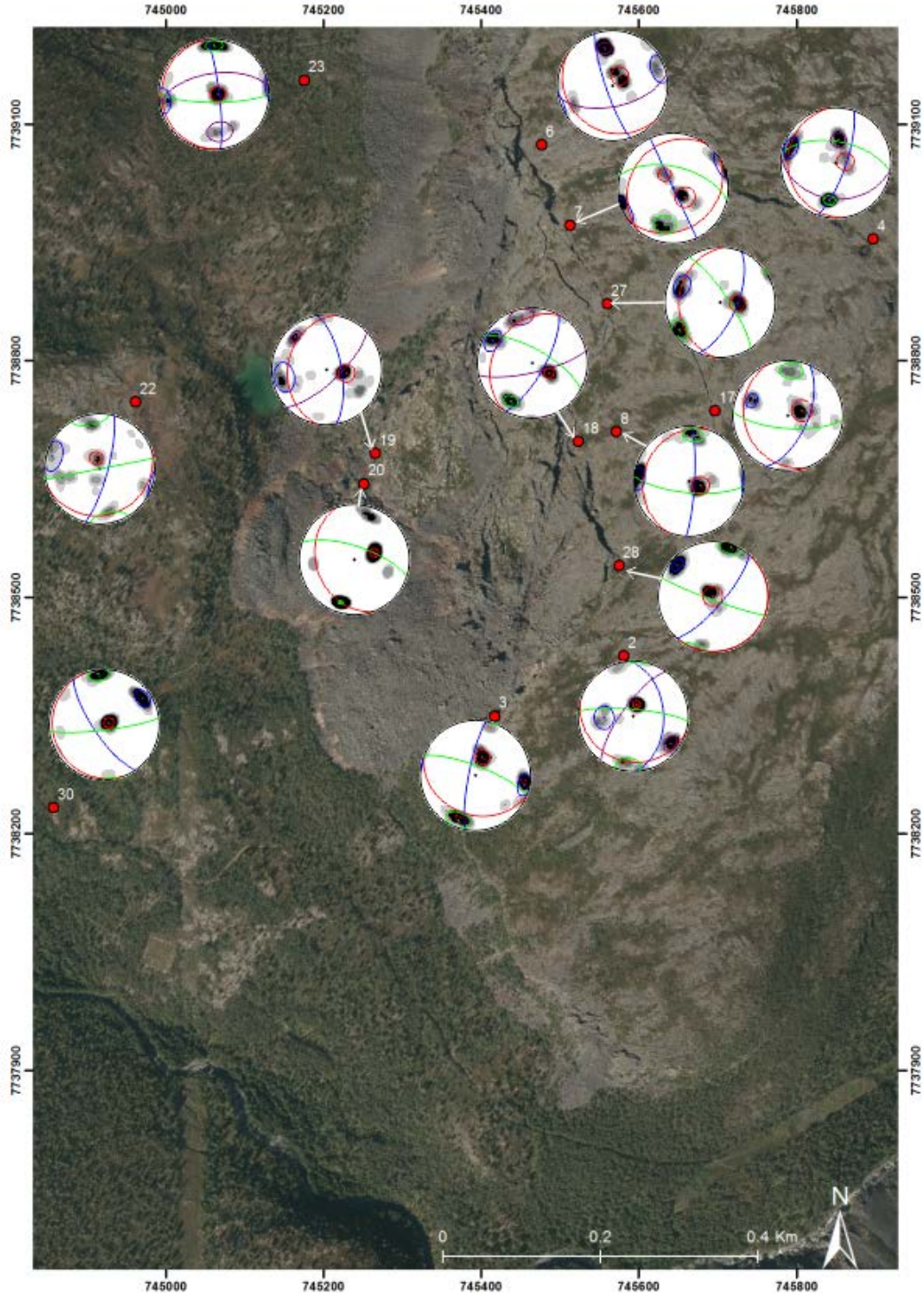

Overview map of the structural data gathered at Mellomfjellet 1, presented in stereonet for each structural station.

Appendix B: Structural map Mellomfjellet 2

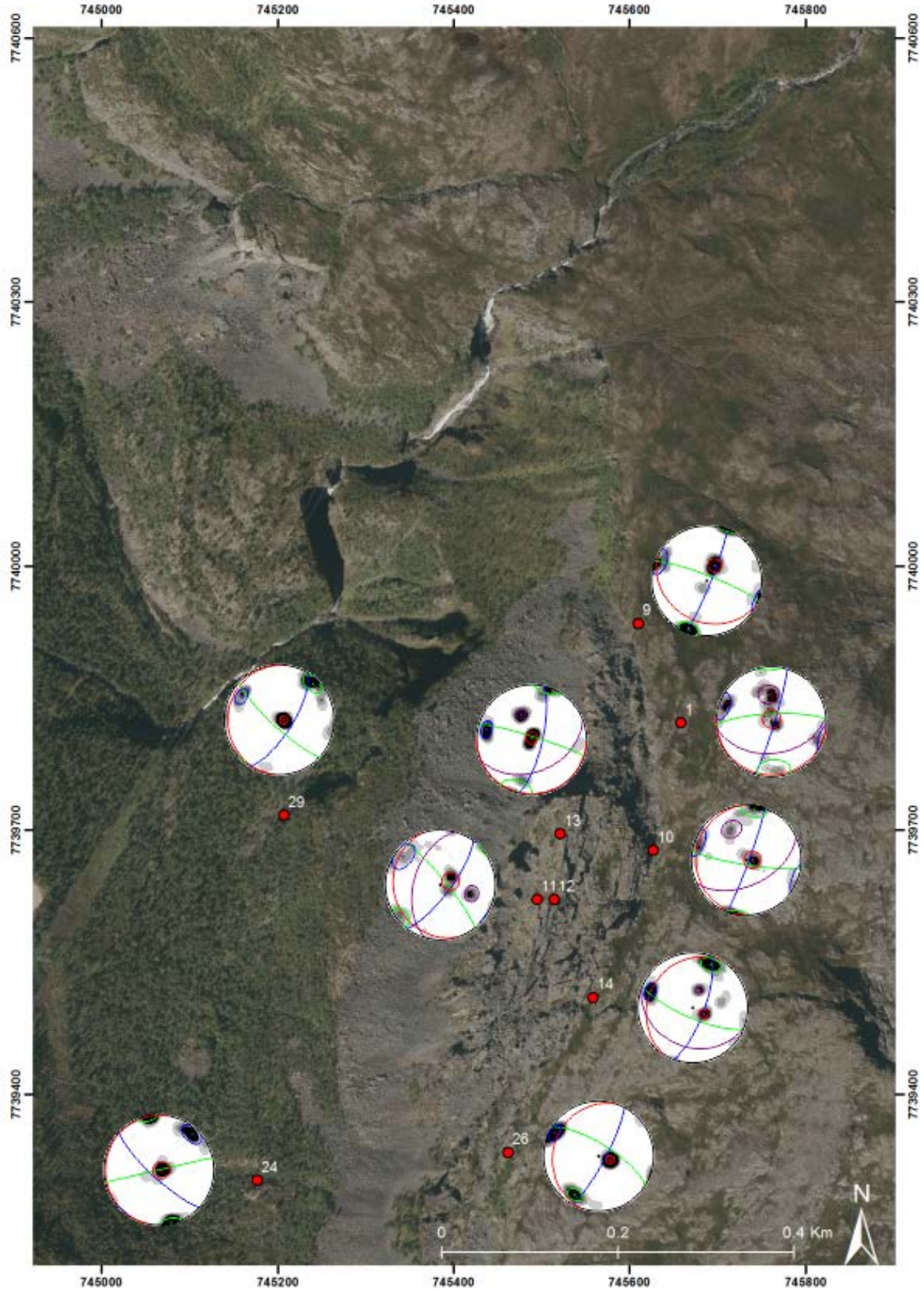

Overview map of the structural data gathered at Mellomfjellet 2, presented in stereonet for each structural station.

Appendix C: InSAR RADARSAT-2

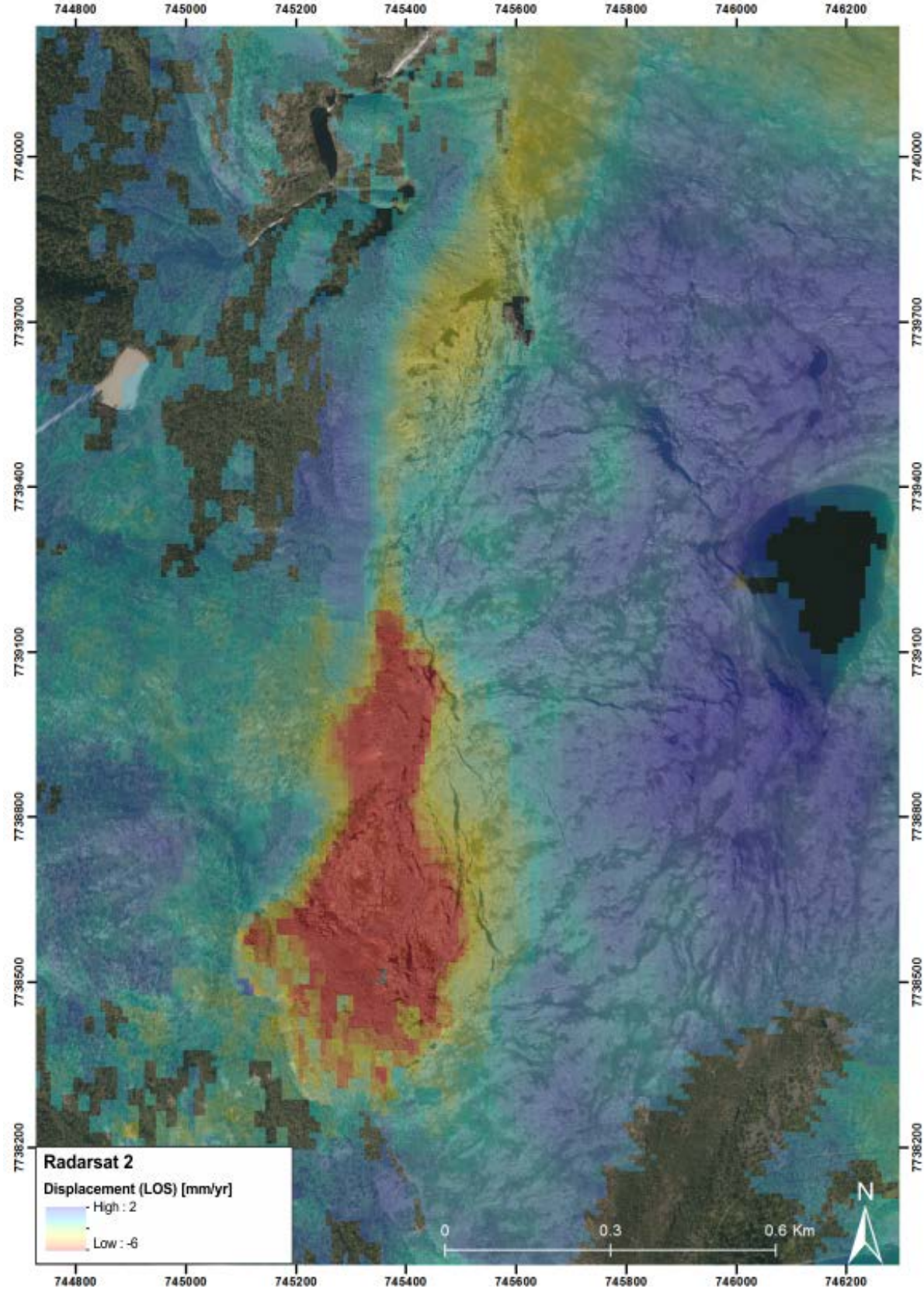

Overview map of the R-SAT InSAR data.

Appendix D: InSAR SENTINEL-1

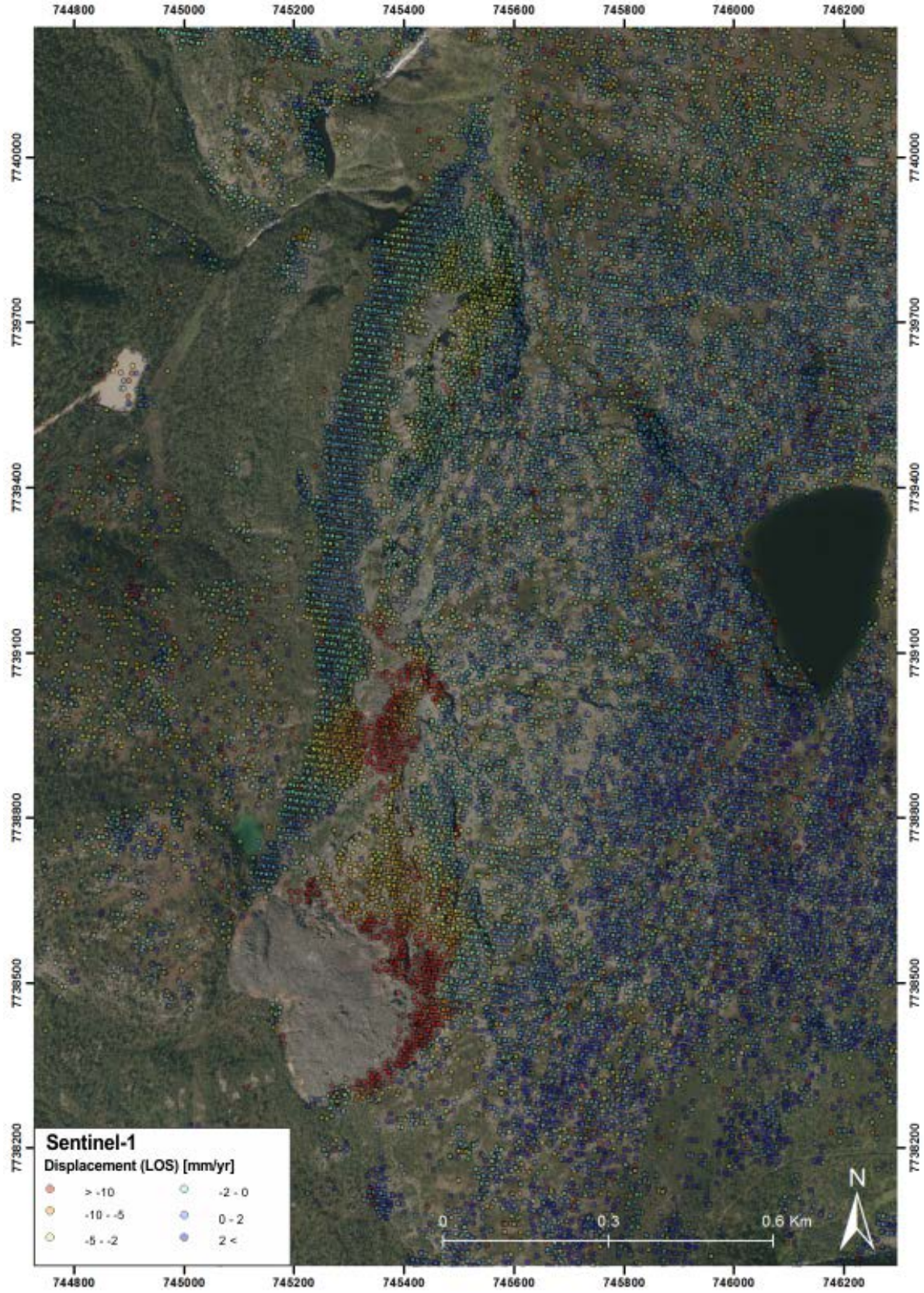

Overview map of the Sentinel InSAR data set.

Appendix E: Agisoft Photoscan report

Survey Data

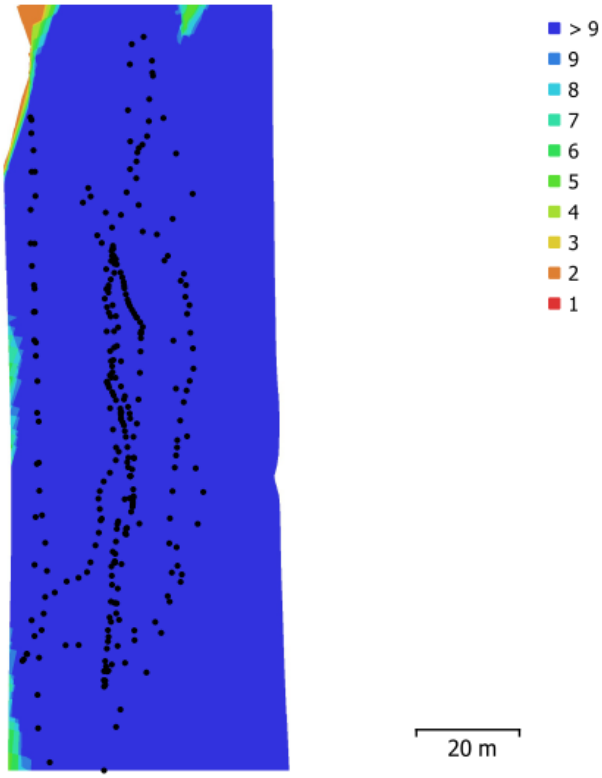

Fig. 1. Camera locations and image overlap.

Number of images:	288	Camera stations:	288
Flying altitude:	23.1 m	Tie points:	258,910
Ground resolution:	9.51 mm/pix	Projections:	1,152,922
Coverage area:	7.7e+03 m²	Reprojection error:	0.725 pix

Camera Model	Resolution	Focal Length	Pixel Size	Precalibrated
FC350 (3.61mm)	4000 x 3000	3.61 mm	1.56 x 1.56 µm	No

Table 1. Cameras.

Ground Control Points

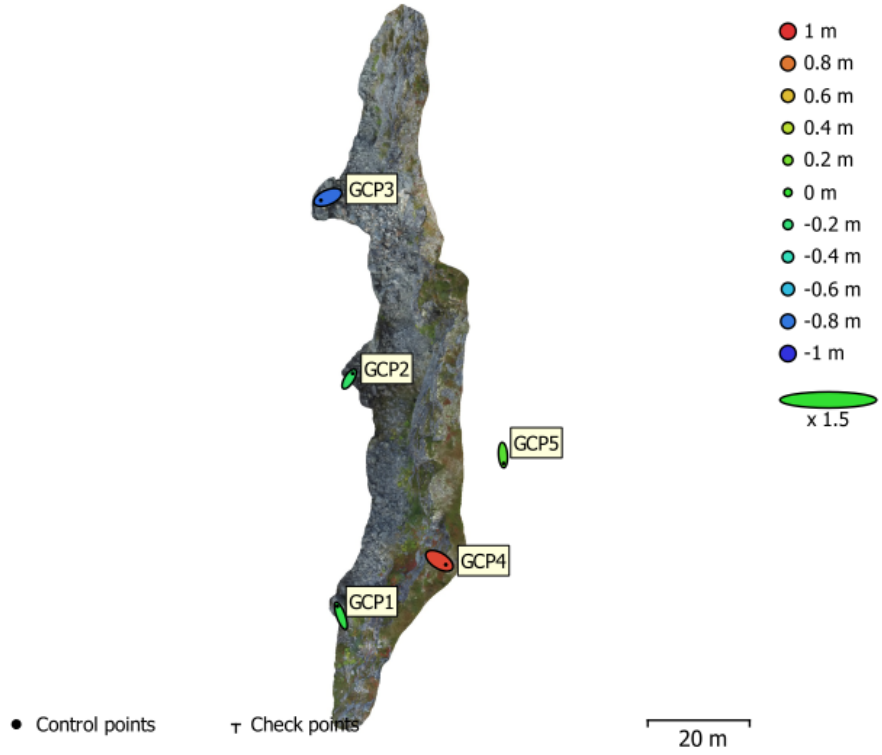

Fig. 3. GCP locations and error estimates.
Z error is represented by ellipse color. X,Y errors are represented by ellipse shape.
Estimated GCP locations are marked with a dot or crossing.

Count	X error (m)	Y error (m)	Z error (m)	XY error (m)	Total (m)
5	1.24731	1.71741	0.570399	2.12256	2.19787

Table 3. Control points RMSE.
X - Easting, Y - Northing, Z - Altitude.

Label	X error (m)	Y error (m)	Z error (m)	Total (m)	Image (pix)
GCP1	-0.911322	2.5033	-0.0698508	2.66494	0.464 (57)
GCP2	0.916574	1.46523	-0.153793	1.73513	0.591 (68)
GCP3	-1.81986	-0.782766	-0.830183	2.14798	0.720 (42)
GCP4	1.66561	-1.0242	0.947486	2.17278	0.849 (61)
GCP5	0.148988	-2.16156	0.106339	2.16929	0.013 (2)
Total	**1.24731**	**1.71741**	**0.570399**	**2.19787**	**0.665**

Table 4. Control points.
X - Easting, Y - Northing, Z - Altitude.

Digital Elevation Model

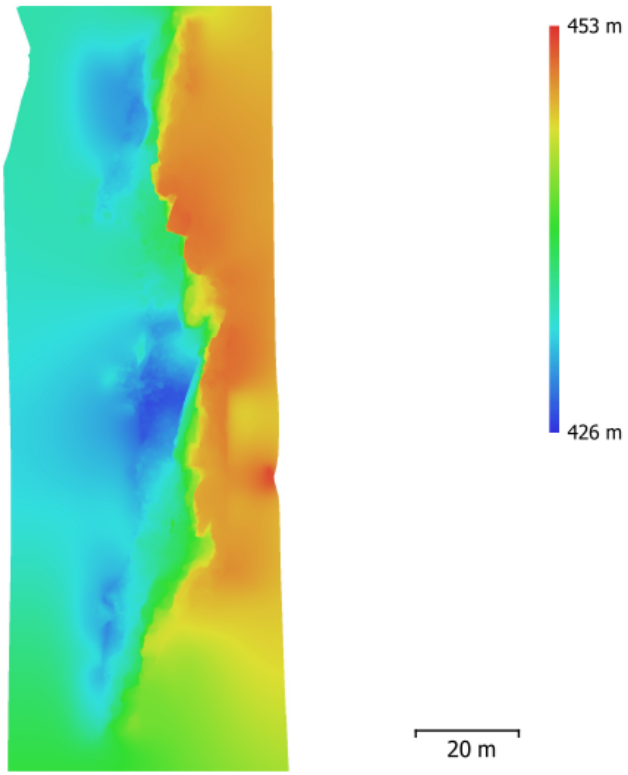

Fig. 4. Reconstructed digital elevation model.

Resolution: 1.9 cm/pix
Point density: 0.277 points/cm²

Processing Parameters

General	
Cameras	288
Aligned cameras	288
Markers	5
Coordinate system	WGS 84 / UTM zone 33N (EPSG::32633)
Rotation angles	Yaw, Pitch, Roll
Point Cloud	
Points	258,910 of 1,447,293
RMS reprojection error	0.219877 (0.724634 pix)
Max reprojection error	3.11953 (14.0158 pix)
Mean key point size	3.28736 pix
Point colors	3 bands, uint8
Key points	No
Average tie point multiplicity	3.7415
Alignment parameters	
Accuracy	High
Generic preselection	Yes
Reference preselection	Yes
Key point limit	60,000
Tie point limit	0
Adaptive camera model fitting	Yes
Matching time	50 minutes 15 seconds
Alignment time	25 minutes 52 seconds
Optimization parameters	
Parameters	f, b1, b2, cx, cy, k1-k4, p1, p2
Adaptive camera model fitting	Yes
Optimization time	32 seconds
Dense Point Cloud	
Points	21,527,475
Point colors	3 bands, uint8
Reconstruction parameters	
Quality	High
Depth filtering	Aggressive
Depth maps generation time	1 days 17 hours
Dense cloud generation time	11 hours 52 minutes
Model	
Faces	4,302,414
Vertices	2,154,066
Vertex colors	3 bands, uint8
Texture	4,096 x 4,096, 4 bands, uint8
Reconstruction parameters	
Surface type	Arbitrary
Source data	Dense
Interpolation	Enabled
Quality	High
Depth filtering	Aggressive
Face count	4,305,495
Processing time	3 hours 51 minutes
Texturing parameters	
Mapping mode	Generic
Blending mode	Mosaic
Texture size	4,096 x 4,096
Enable hole filling	Yes
Enable ghosting filter	Yes
UV mapping time	1 minutes 5 seconds

Processing Parameters

Blending time	17 minutes 18 seconds
DEM	
Size	3,421 x 8,732
Coordinate system	WGS 84 / UTM zone 33N (EPSG::32633)
Reconstruction parameters	
Source data	Dense cloud
Interpolation	Enabled
Processing time	49 seconds
Software	
Version	1.4.4 build 6848
Platform	Windows 64

Appendix F: Bedrock Map

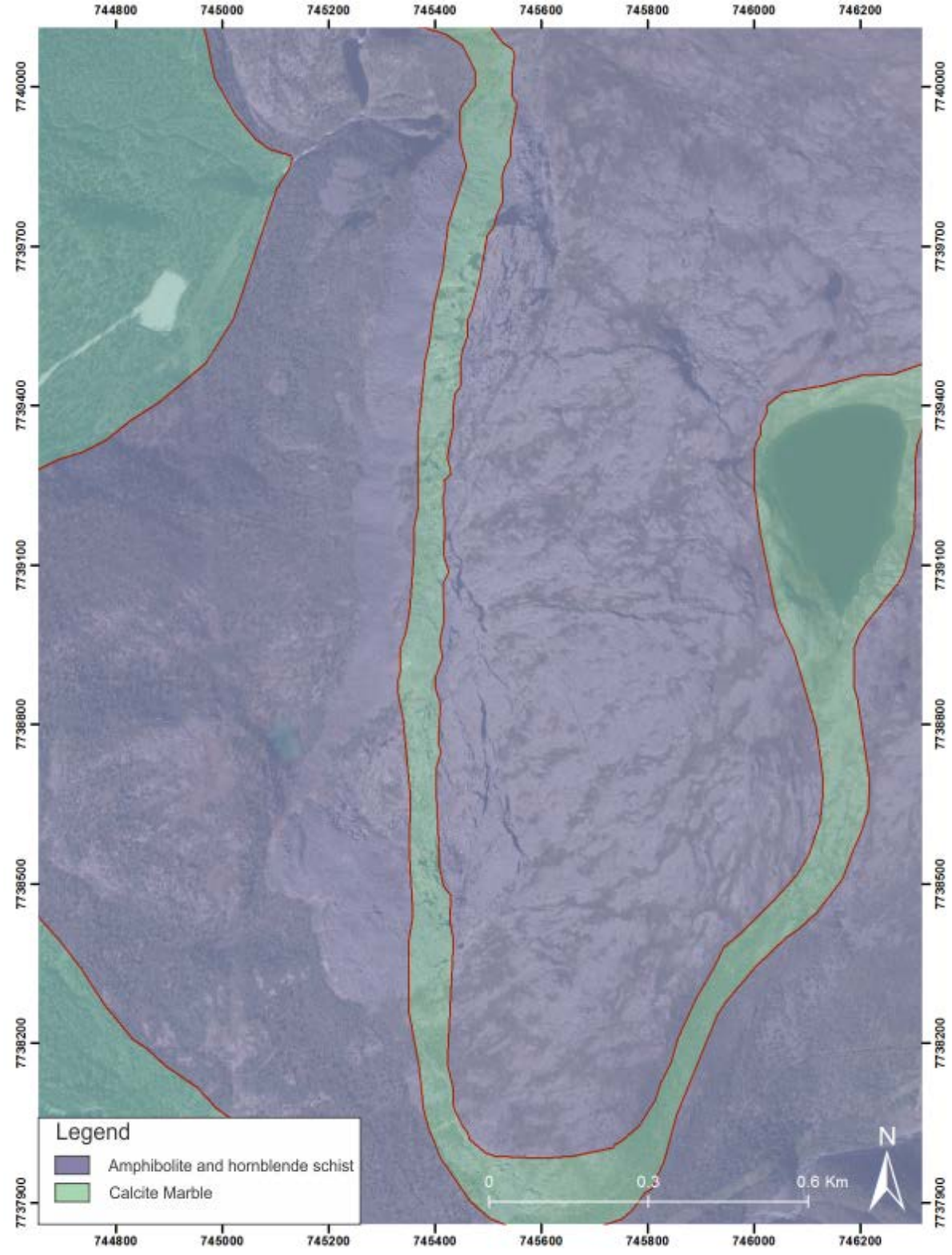

Bedrock geology based on NGU's 1:50 000 bedrock map (Zwaan et al., 1984).

Appendix G: Lineament analysis

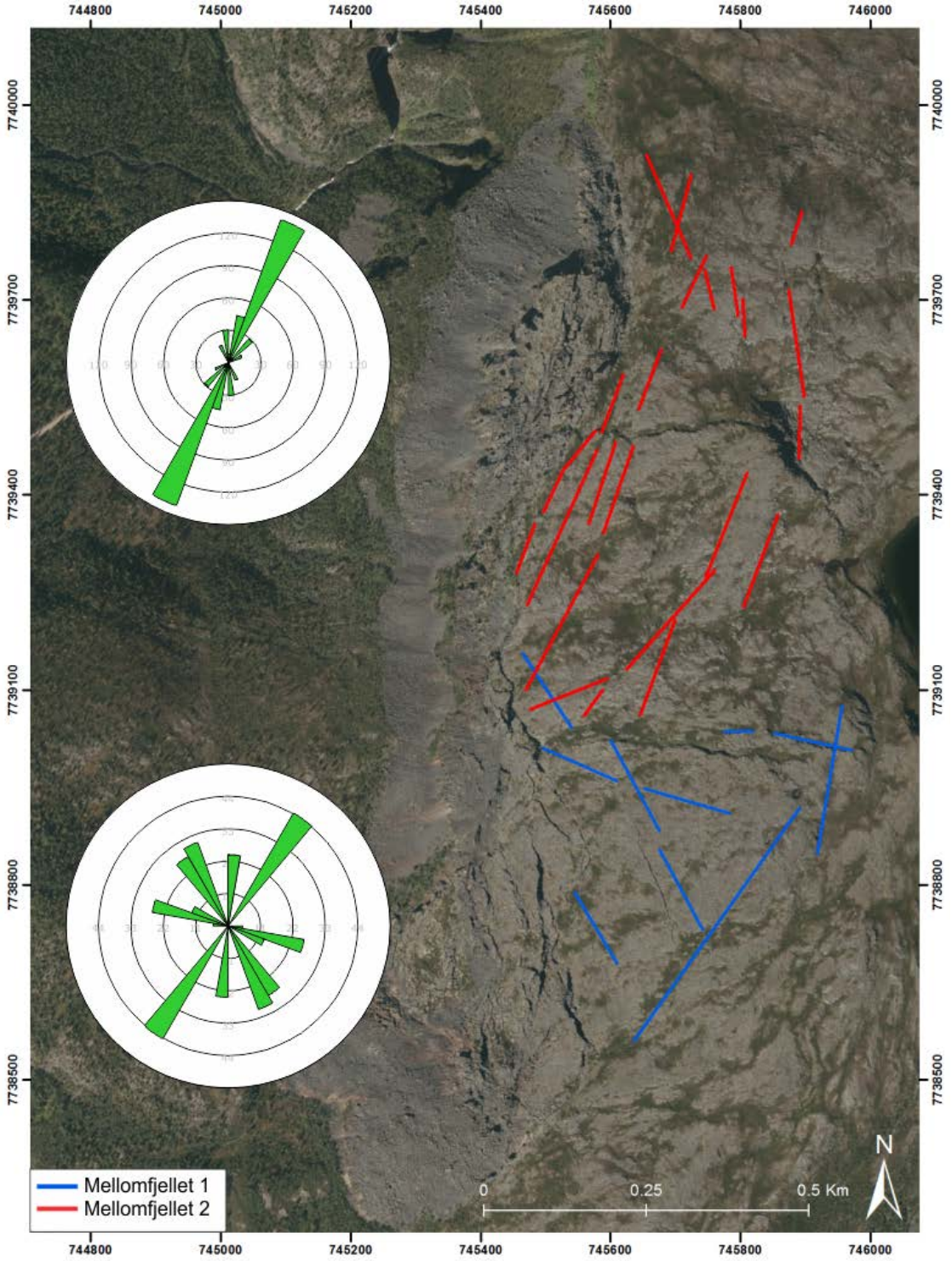

Overview map of the lineaments mapped from orthophoto and hillshade, for the two structural domains. Rosette plots for the two domains are showing the orientation of the mapped lineaments, where the blue lineaments are for Mellomfjellet 1 and red lineaments are for Mellomfjellet 2.

Appendix H: Hazard assessment

Hazard assesment of unstable rockslopes in Norway

Name of locality Mellomfjellet 1 **Scenario:** 1 **Made by:** GS **Date:** 18.03.2019

Hazard classes	Probability	Cumulative prob.
Very low	0.0 %	0.0 %
Low	0.0 %	0.0 %
Medium	100.0 %	100.0 %
High	0.0 %	100.0 %
Very high	0.0 %	100.0 %

Hazard score	
Minimum	5.0
Maximum	6.0
Mode	5.0
Mean	5.3
5% percentile	5.0
95% percentile	6.0

Fitted normal distribution	
Mean μ	0.0
St. dev σ	0.0
μ - 2σ	0.0
μ + 2σ	0.0
Corr. coeff.	0.0000
K-S-test	0.0 %

1. Back-scarp	**Score**	**Norm. prob.**
Not developped	0	0.0 %
Partly open over width of slide body (few cm to m)	0.5	75.0 %
Fully open over width of slide body (few cm to m)	1	25.0 %
Comment: The backscarps have a few meters of offset between them, but are connected with depressions in the terrain or smaller cracks.		

2. Potential sliding structures	**Score**	**Norm. prob.**
No penetrative structures dip out of the slope	0	0.0 %
Penetrative structures dip on average < 20 degree or steeper than the slope	0.5	66.7 %
Penetrative structures dip on average > 20 degree and daylight with the slope	1	33.3 %
Comment: Potentiall sliding structures are mainly the foliation, which dips downslope. Since it is gently folded, the fold axes are also a possible structure to access.		

3. Lateral release surfaces	**Score**	**Norm. prob.**
Not developped	0	0.0 %
Partly developped on 1 side	0.25	0.0 %
Fully developped or free slope on 1 side or partly developped on 2 sides	0.5	0.0 %
Fully developped or free slope on 1 side and partly developped on 1 side	0.75	0.0 %
Fully developped or free slope on 2 sides	1	100.0 %
Comment: The location has open scarps on both sides, in a wedge shape. Hence, completely developed flanks.		

4. Kinematic feasibility test	**Score**	**Norm. prob.**
Kinematic feasibility test does not allow for planar sliding, wedge sliding or toppling	0	0.0 %
Failure is partly feasible kinematically (movement direction is more than ±30° to slope orientation)	0.5	0.0 %
Failure is feasible kinematically (movement direction is less than ±30° to slope orientation)	0.75	0.0 %
Failure is partly feasible kinematically on persistent discontinuities (movement direction is more than ±30° to slope orientation)	0.75	0.0 %
Failure is feasible kinematically on persistent discontinuities (movement direction is less than ±30° to slope orientation)	1	100.0 %
Comment: Planar sliding along the foliation is possible. The average foliation is not steep enough, but due to large variation within the set it is possible along multiple		

5. Morphologic expression of the rupture surface	**Score**	**Norm. prob.**
No indication on slope morphology	0	100.0 %
Slope morphology suggests formation of a rupture surface (bulging, concavity-convexity, springs)	0.5	0.0 %
Continuous rupture surface is suggested by slope morphology and can be mapped out	1	0.0 %
Comment: No certain signs of the rupture plane, only assumptions.		

6. Displacement rates	**Score**	**Norm. prob.**
No significant movement	0	0.0 %
>0 - 0.5 cm/year	1	100.0 %
0.5 - 1 cm/year	2	0.0 %
1 - 4 cm/year	3	0.0 %
4 - 10 cm/year	4	0.0 %
> 10 cm/year	5	0.0 %
Comment: The slowest recorded velocity for the scenario is below 0.5cm/yr		

7. Acceleration (if velocity is >0.5 cm/yr and <10 cm/yr)	**Score**	**Norm. prob.**
No acceleration or change in displacement rates	0	80.0 %
Increase in displacement rates	1	20.0 %
Comment: Standard value if no data available		

8. Increase of rock fall activity	**Score**	**Norm. prob.**
No increase of rock fall activity	0	0.0 %
Increase of rock fall activity	1	100.0 %
Comment: Multiple fresh surfaces from recent rock fall activity was mapped.		

9. Past events	**Score**	**Norm. prob.**
No post-glacial events of similar size	0	100.0 %
One or several events older than 5000 years of similar size	0.5	0.0 %
One or several events younger than 5000 years of similar size	1	0.0 %
Comment: No post-glacial events of similar size.		

Report showing the results from the hazard assessment of Mellomfjellet 1.

Hazard assesment of unstable rockslopes in Norway

Name of locality Mellomfjellet 2 **Scenario:** 1 **Made by:** GS **Date:** 18.03.2019

Hazard classes	Probability	Cumulative prob.
Very low	0.0 %	0.0 %
Low	0.0 %	0.0 %
Medium	100.0 %	100.0 %
High	0.0 %	100.0 %
Very high	0.0 %	100.0 %

Hazard score	
Minimum	5.5
Maximum	6.0
Mode	5.5
Mean	5.6
5% percentile	5.5
95% percentile	6.0

Fitted normal distribution	
Mean μ	0.0
St. dev σ	0.0
μ - 2σ	0.0
μ + 2σ	0.0
Corr. coeff.	0.0000
K-S-test	0.0 %

1. Back-scarp	**Score**	**Norm. prob.**
Not developped	0	0.0 %
Partly open over width of slide body (few cm to m)	0.5	0.0 %
Fully open over width of slide body (few cm to m)	1	100.0 %
Comment: Fully developed backscarp over the entire location.		

2. Potential sliding structures	**Score**	**Norm. prob.**
No penetrative structures dip out of the slope	0	0.0 %
Penetrative structures dip on average < 20 degree or steeper than the slope	0.5	80.0 %
Penetrative structures dip on average > 20 degree and daylight with the slope	1	20.0 %
Comment: Potentiall sliding structures are mainly the foliation, which dips downslope. Since it is gently folded, the fold axes are a possible structure to access.		

3. Lateral release surfaces	**Score**	**Norm. prob.**
Not developped	0	0.0 %
Partly developped on 1 side	0.25	0.0 %
Fully developped or free slope on 1 side or partly developped on 2 sides	0.5	0.0 %
Fully developped or free slope on 1 side and partly developped on 1 side	0.75	0.0 %
Fully developped or free slope on 2 sides	1	100.0 %
Comment: Scarps fully developed on both sides.		

4. Kinematic feasibility test	**Score**	**Norm. prob.**
Kinematic feasibility test does not allow for planar sliding, wedge sliding or toppling	0	0.0 %
Failure is partly feasible kinematically (movement direction is more than ±30° to slope orientation)	0.5	0.0 %
Failure is feasible kinematically (movement direction is less than ±30° to slope orientation)	0.75	0.0 %
Failure is partly feasible kinematically on persistent discontinuities (movement direction is more than ±30° to slope orientation)	0.75	0.0 %
Failure is feasible kinematically on persistent discontinuities (movement direction is less than ±30° to slope orientation)	1	100.0 %
Comment: Toppling possible along J1, which is very persistant.		

5. Morphologic expression of the rupture surface	**Score**	**Norm. prob.**
No indication on slope morphology	0	100.0 %
Slope morphology suggests formation of a rupture surface (bulging, concavity-convexity, springs)	0.5	0.0 %
Continuous rupture surface is suggested by slope morphology and can be mapped out	1	0.0 %
Comment: No certain sign of rupture surfaces, only assumptions.		

6. Displacement rates	**Score**	**Norm. prob.**
No significant movement	0	0.0 %
>0 - 0.5 cm/year	1	100.0 %
0.5 - 1 cm/year	2	0.0 %
1 - 4 cm/year	3	0.0 %
4 - 10 cm/year	4	0.0 %
> 10 cm/year	5	0.0 %
Comment: The slowest velocity is below 0.5cm/yr.		

7. Acceleration (if velocity is >0.5 cm/yr and <10 cm/yr)	**Score**	**Norm. prob.**
No acceleration or change in displacement rates	0	80.0 %
Increase in displacement rates	1	20.0 %
Comment: Standard value if unknown.		

8. Increase of rock fall activity	**Score**	**Norm. prob.**
No increase of rock fall activity	0	0.0 %
Increase of rock fall activity	1	100.0 %
Comment: Multiple recent rockfalls mapped.		

9. Past events	**Score**	**Norm. prob.**
No post-glacial events of similar size	0	100.0 %
One or several events older than 5000 years of similar size	0.5	0.0 %
One or several events younger than 5000 years of similar size	1	0.0 %
Comment: No post-glacial events of similar size.		

Report showing the results from the hazard assessment of Mellomfjellet 2.

Appendix I: Field guide sheet

NZ GEOTECHNICAL SOCIETY INC

ROCK > field guide sheet

FIELD DESCRIPTION OF ROCK

SEQUENCE OF TERMS – weathering – colour – fabric – rock name – strength – discontinuities – additional

SCALE OF ROCK MASS WEATHERING

Term	Grade	Abbreviation	Description
Unweathered (fresh rock)	I	UW	Rock mass shows no loss of strength, discolouration or other effects due to weathering. There may be slight discolouration on major rock mass defect surfaces or on clasts.
Slightly Weathered	II	SW	The rock mass is not significantly weaker than when fresh. Rock may be discoloured along defects, some of which may have been opened slightly.
Moderately Weathered	III	MW	The rock mass is significantly weaker than the fresh rock and part of the rock mass may have been changed to a soil. Rock material may be discoloured and defect and clast surfaces will have a greater discolouration, which also penetrates slightly into the rock material. Increase in density of defects due to physical disintegration.
Highly Weathered	IV	HW	Most of the original rock mass strength is lost. Material is discoloured and more than half the mass is changed to a soil by chemical decomposition or disintegration (increase in density of defects/fractures). Decomposition adjacent to defects and at the surface of clasts penetrates deeply into the rock material. Lithorelicts or corestones of unweathered or slightly weathered rock may be present.
Completely Weathered	V	CW	Original rock strength is lost and the rock mass changed to a soil either by decomposition (with some rock fabric preserved) or by physical disintegration.
Residual Soil	VI	RS	Rock is completely changed to a soil with the original fabric destroyed (pedological soil).

ROCK STRENGTH TERMS

Term	Field Identification of Specimen	Unconfined uniaxial compressive strength q_u (MPa)	Point load strength $I_{S(50)}$ (MPa)
Extremely strong	Can only be chipped with geological hammer	> 250	>10
Very strong	Requires many blows of geological hammer to break it	100 – 250	5 – 10
Strong	Requires more than one blow of geological hammer to fracture it	50 – 100	2 – 5
Moderately strong	Cannot be scraped or peeled with a pocket knife. Can be fractured with single firm blow of geological hammer	20 – 50	1 – 2
Weak	Can be peeled by a pocket knife with difficulty. Shallow indentations made by firm blow with point of geological hammer	5 – 20	<1
Very weak	Crumbles under firm blows with point of geological hammer. Can be peeled by a pocket knife	1 – 5	
Extremely weak (soil description required)	Indented by thumb nail or other lesser strength terms used for soils	<1	

Note: No correlation is implied between q_u and $I_{(50)}$

SPACING OF DEFECTS/ DISCONTINUITIES

Term	Spacing
Very widely spaced	>2 m
Widely spaced	600 mm – 2 m
Moderately widely spaced	200 mm – 600 mm
Closely spaced	60 mm – 200 mm
Very closely spaced	20 mm – 60 mm
Extremely closely spaced	<20 mm

APERTURE OF DISCONTINUITY SURFACES

Term	Aperture (mm)	Description
Tight	Nil	Closed
Very Narrow	> 0 – 2	
Narrow	2 – 6	
Moderately Narrow	6 – 20	Gapped
Moderately Wide	20 – 60	Open
Wide	60 – 200	
Very Wide	> 200	

BEDDING THICKNESS TERMS

Term	Bed Thickness
Thinly laminated	< 2 mm
Laminated	2 mm - 6 mm
Very thin	6 mm - 20 mm
Thin	20 mm - 60 mm
Moderately thin	60 mm - 200 mm
Moderately thick	0.2 m - 0.6 m
Thick	0.6 m - 2 m
Very thick	> 2 m

BEDDING INCLINATION TERMS

Term	Inclination (from horizontal)
Sub-horizontal	0° – 5°
Gently inclined	6° – 15°
Moderately inclined	16° – 30°
Steeply inclined	31° – 60°
Very steeply inclined	61° – 80°
Sub-vertical	81° – 90°

ROUGHNESS AND APERTURE

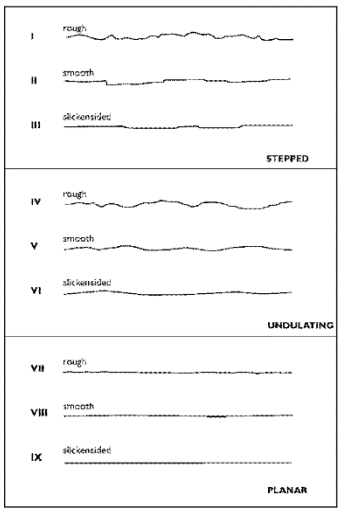

compiled by KATE WILLIAMS design KARRYN MUSCHAMP

NZ GEOTECHNICAL SOCIETY INC

This field sheet has been taken from and should be used and read with reference to the document FIELD DESCRIPTION OF SOIL AND ROCK. Guideline For the Field Classification and Description of Soil and Rock for Engineering Purposes. NZ Geotechnical Society Inc, December 2005. **www.nzgeotechsoc.org.nz**

Field guide used when estimating discontinuity spacing, -roughness and waviness.